Synthesis and Characterization of Aerosol Silicon Nanoparticle Nonvolatile Floating Gate Memory Devices

Thesis by

Michele L. Ostraat

In Partial Fulfillment of the Requirements

for the Degree of

Doctor of Philosophy

California Institute of Technology

Pasadena, California

2001

(Submitted February 6, 2001)

To my husband, Eric
with all my love

Acknowledgments

As with any collaborative work, this thesis represents not only my efforts and ideas, but those from my colleagues as well. I am greatly indebted to my advisors, Richard C. Flagan and Harry A. Atwater. Not only have they given me the latitude and trust to work on topics of interest to me, but they have allowed me to form valuable, close collaborations with members outside of the Caltech community. I am grateful for their support, advice, and insights throughout my graduate career. I am particularly appreciative of their ability to mentor me in a productive manner, knowing when I needed a push in a certain direction and recognizing when they should just stand by and let me forge ahead on my own.

I also wish to acknowledge my collaborators, Jan W. De Blauwe and Martin L. Green. Not only did they provide invaluable advice that allowed me to build an ultra clean system that enabled state-of-the-art production of aerosol devices in Lucent's facilities, but they believed in me enough to trust that I would not inadvertently destroy the Lucent cleanroom equipment. I also appreciate the time they spent with me when I was in New Jersey doing the electrical characterization of these devices. I needed significant help during those times and Jan and Marty were wonderful mentors.

I am indebted to Carol Garland and Channing Ahn for teaching me everything I know about the TEM and sample preparation. I could not have done this work without them. I wish to thank L. Doug Bell from the Jet Propulsion Laboratory. His experimental help was greatly appreciated, as were his candid and honest impressions. Thanks are also

in order to Mark Brongersma for his helpful discussions in devices and to Elizabeth Boer for her help in AFM, XPS, and AES.

I owe my thanks to the students in Chemical Engineering and Environmental Engineering who throughout my time at Caltech had to suffer through the noise from the cleanroom blowers as they shared lab space with me, namely Marcus Kalberer, Tim VanReken, Brian Mader, Jian Wang, and Dean Holunga. I have taken up more than my share of lab space. I also wish to acknowledge Thanos Nenes and Mina Sierou for helping me whenever the feared "modeling" came up in my thesis. Alas, some of us are experimentalists at heart and we absolutely depend upon those who are not.

I wish to thank Kathy Bubash and Christine Silva, who often go unacknowledged as those responsible for keeping the Chemical Engineering Department running smoothly and to Carol Mann who keeps Rick's schedule running smoothly. Perhaps more importantly, all three are excellent sources for chocolate and sweet tarts.

I owe a great deal of thanks to my parents, Willard and Alice, for instilling within me the importance and value of a good education and hard work. I wish to thank my in-laws, Randy and Sharon, for their unwavering faith in my abilities.

I also want to thank my husband, Eric, for whom this thesis is dedicated. Not only does he give me the confidence to trust myself and my abilities and the encouragement to face difficult challenges, but he balances the analytical tendencies within me to make me a complete person. I know that we are both fortunate to have found each other.

Abstract

Silicon nanoparticle-based floating gate metal-oxide-semiconductor (MOS) field effect devices have potential for terabit cm^{-2} density nonvolatile memory applications. Aerosol synthesis of silicon nanoparticles is an important route toward the formation of discontinuous silicon nanoparticle floating gate structures that affords excellent control over particle size and size distribution, particle density, and oxide passivation. We have fabricated nanoparticle memory devices in a conventional MOS ultra-large scale integration (ULSI) process with channel lengths from 0.2 - 10 μm with a silicon nanoparticle floating gate fabricated by aerosol deposition.

SiO_2 passivated silicon nanoparticles have been synthesized in an ultra clean two-stage aerosol reactor that is interfaced to a 200 mm wafer deposition chamber in a class 100 cleanroom. We synthesize silicon nanoparticles by thermal decomposition of silane gas at 950°C to produce single crystal, nonagglomerated nanoparticles. The second reactor stage passivated the silicon nanoparticles with a thin thermal oxide grown at 1050°C. Particles are thermophoretically deposited onto 200 mm silicon wafers with densities from 10^{13} particles cm^{-2} at the wafer center to 10^{11} particles cm^{-2} at the wafer edge in tens of minutes. We have fabricated floating gate memory devices in which the dielectric layer contains a discontinuous nanoparticle layer containing either (i) 2 -4 nm crystalline core diameter with 1 nm thermal oxide; or (ii) 6 - 15 nm crystalline core diameter with 2 nm thermal oxide. Cross-sectional transmission electron microscopy

(TEM) verifies the presence of a silicon nanoparticle floating gate layer and planar TEM confirms nanoparticle morphology, size, and density.

Aerosol floating gate devices exhibit normal transistor behavior and have promising nonvolatile device performance. Aerosol nanoparticle devices with 0.2 mm channel lengths exhibit threshold voltages < 5 V with large threshold voltage shifts (~ 2 V), submicrosecond program times and millisecond erase times. No degradation in program/erase threshold voltage swing was observed during 10^5 program and erase cycles, although some threshold voltage shift due to charge trapping was observed. Electrostatic modeling indicates when a discontinuous nanoparticle layer can be modeled as a continuous sheet charge embedded within oxide and when it should be modeled as individual nanoparticles in an array.

Contents

List of Figures

List of Tables

Chapter 1: Introduction

1.1 Motivation

In recent years, considerable research has focused on nanostructured materials for a vast array of technological applications. These structures are in the nanometer size range and their characteristic length scale is on the order of the deBroglie wavelength of an electron. These nanostructures are composed of hundreds to tens of thousands of atoms. Because of their extremely small sizes, nanostructures possess interesting chemical and physical properties that are often very different from the properties of the bulk material or molecular species from which they are composed. Since the band structure of semiconducting materials is neither an atomic nor a molecular property but a property of the periodic arrangement of a large number of atoms in a crystal lattice, it has been found that material properties gradually change from those of the bulk semiconductor to the molecular properties in the nanometer range, leading to drastic changes in optical and electrical properties [1]. For example, the current through a nanoparticle or the capacitance between two leads on a nanoparticle can vary by several orders of magnitude when the charge on a nanoparticle is changed by a single electron [2]. Efforts to synthesize semiconductor nanoparticles stem from a desire to produce structures in which the band gap and associated properties can be chosen by the designer, was well as fabricating smaller dimension nanoscale devices.

Although numerous semiconductor materials exist, this discussion focuses

primarily upon silicon since it exhibits certain advantages over other semiconductor materials. Silicon is readily available in large sizes with a high degree of crystal perfection. It has a high quality oxide and superior processing, thermal, and mechanical properties. Additionally, a considerable amount of time, money, and capital has been invested in ultra-large scale integration (ULSI) silicon manufacturing [3]. However, as the limits to silicon technology are becoming real issues, solutions are being investigated to meet future progress in silicon devices. Future devices will inevitably incorporate nanostructured materials and layers. Indeed, critical structures in semiconductor devices today are already in the 1 - 2 nm range, and control over these dimensions is critically important. Currently, some experimental semiconductor devices utilize two-dimensional nanostructures, i.e., quantum wells [4],[5],[6] for quantum confinement effects, such as the quantum well semiconductor laser [7],[8]. The possibility of applying quantum confinement effects into other devices that incorporate nanostructured materials has motivated a vast amount of research directed toward the synthesis and characterization of such structures.

1.2 Objectives

This thesis discusses the synthesis and characterization of 0.20 μm aerosol silicon nanoparticle nonvolatile floating gate memory devices fabricated in state-of-the-art ULSI processing facilities.

Chapter 2 is an introduction to nanostructured materials, particularly nanoparticles

and the application of silicon nanoparticles in floating gate memory devices. First, the basic operation of a field effect transistor will be discussed. The operation of and similarities and differences between conventional and nanoparticle floating gate memories will be discussed. Advantages to aerosol nanoparticle floating gate memories will serve as the overall objective of this thesis.

Chapter 3 is a discussion on the synthesis of aerosol silicon nanoparticles. It focuses primarily on the formation of uniformly sized, spherical, single crystal, nonagglomerated silicon nanoparticles via silane decomposition and particle size classification. Reactor design issues will be discussed.

Chapter 4 introduces the topic of silicon nanoparticle colloids and particle reactions. It also discusses particle collection, including electrostatic deposition, thermophoretic deposition, and colloid collection. Reactions between nanoparticles and oxygenated solvents, including ethylene glycol, water, and ethanol, are discussed in addition to the role that dissolved oxygen plays in those reactions. Evidence for alkoxysilane formation in ethanol colloids will be mentioned as a point of interest.

Chapter 5 discusses the oxide passivation of silicon nanoparticles, including thermal oxidation in the aerosol phase and TEOS oxidation in both the liquid phase and the aerosol phase. Although the different oxide-passivation methods produce interesting structures, the formation of well-controlled oxide shells is of greater importance in the overall objectives of this thesis.

Chapter 6 introduces the ultra clean two-stage aerosol reactor and deposition chamber for the production of oxide-passivated aerosol silicon nanoparticle floating gates

on 200 mm silicon wafers. A portion of this chapter discusses the efforts required to conform to industry standards and addresses the important issue of contamination control in order to facilitate an exchange of materials between Caltech and Lucent Technologies/Bell Laboratories for an intense collaboration.

Chapter 7 discusses details of the silicon nanoparticle device fabrication and structural characterization of nanoparticle floating gate layers and nanoparticle devices. Of particular interest are dimensions and uniformity of the tunnel oxide layer, the nanoparticle layer, and the high temperature oxide (HTO) layer. The effect of the nanoparticle layer on the HTO layer conformation, uniformity, and adhesion are also probed. The structural characterization is examined with optical microscopy, atomic force microscopy, and transmission electron microscopy.

Chapter 8 discusses the electrical characterization of aerosol silicon nanoparticle floating gate memory devices and electrostatic modeling of the floating gate region. Some discussion on the effects of nanoparticle size and density on the electrical characterizations are included. Electrical characterization of these aerosol devices includes current-voltage characteristics, program and erase transients, endurance, gate and drain disturb, and retention measurements.

Chapter 9 summarizes the conclusions of this thesis and presents comments on some future improvements and directions for this project, including adding size classification to the ultra clean reactor and producing a deposition chamber that produces uniform nanoparticle deposits over the entire 200 mm silicon wafer.

Appendix A describes the ultra clean reactor protocol, including the ultra clean

reactor start up and shut down procedures.

Appendix B lists the cleanroom protocol and wafer handling for controlling wafer contamination.

Appendix C catalogs the ultra clean reactor and deposition parts and building the ultra clean reactor. This information is included to ensure that future changes and modifications to the ultra clean reactor and deposition chamber are consistent with existing equipment and to ensure continued cleanliness of the equipment.

Appendix D describes the various TEM sample preparation techniques used in completing this thesis, including basic procedures for colloidal deposition, electrostatic deposition, cross-section, wedge, and double-wedge techniques.

Appendix E provides the source code for the electrostatic modeling of the continuous sheet charge and nanoparticle floating gate layers.

Bibliography

[1] A. Henglein, "Small-Particle Research: Physicochemical Properties of Extremely Small Colloidal Metal and Semiconductor Particles," *Chem. Rev.*, **89**, pp. 1861-1873 (1989).

[2] M.A. Kastner, "Artificial Atoms," *Physics Today*, pp. 24-31 (January 1993).

[3] R.T. Collins, P.M. Fauchet, and M.A. Tischler, "Porous Silicon: From Luminescence to LEDs," *Physics Today*, pp. 24-31 (January 1997).

[4] S. Tiwari, F. Rana, H. Hanafi, A. Hartstein, E.F. Crabbe, and K. Chan, "A Silicon Nanocrystals Based Memory," *Appl. Phys. Lett.*, **68**, pp. 1377-1379 (1996).

[5] S. Tiwari, F. Rana, K. Chan, L. Shi, and H. Hanafi, "Single Charge and Confinement Effects in Nano-Crystal Memories," *Appl. Phys. Lett.*, **69**, pp. 1232-1234 (1996).

[6] H.I. Hanafi, S. Tiwari, and I. Khan, "Fast and Long Retention-Time Nano-Crystal Memory," *IEEE Trans. Electron Dev.*, **43**, pp. 1553-1558 (1996).

[7] H. Okamoto, "Semiconductor Quantum Well Lasers for Optoelectronic Applications," *Jpn. J. App. Phys.*, **26**, p. 315 (1987).

[8] L.E. Brus, "Quantum Crystallites and Nonlinear Optics," *Appl. Phys. A.*, **53**, pp. 465-474 (1991).

Chapter 2: Applications for Silicon Nanoparticles: Emphasis on Nonvolatile Nanoparticle Floating Gate Memory Devices

2.1 Introduction

In recent years, considerable research has focused upon nanostructured materials for a vast array of technological applications. These nanostructures are in the nanometer size range and their characteristic length scale is on the order of the deBroglie wavelength of an electron. Two-dimensional nanostructures, i.e., ones with only one length scale within the nanometer size range, are called quantum wells, one-dimensional nanostructures are called quantum wires, and zero-dimension nanostructures, i.e., ones with all length scales within the nanometer range, are called nanoparticles, nanoparticles, or quantum dots. These nanoparticles are typically composed of only hundreds to thousands of individual atoms. Because of their extremely small size, nanoparticles often possess interesting chemical, physical, optical, and electrical properties that are very different from the properties of the bulk material or molecular species from which they are composed. These properties are often nanoparticle size dependent. Furthermore, because of their very substantial surface area to volume ratios, the surface chemistry of nanoparticles greatly affects their properties and behavior.

2.2 Silicon Nanoparticle Applications

A wide variety of applications exist for nanoparticles, including fine-grained materials and nanostructured alloys, optoelectronics, and advanced memory and switching devices, such as cellular automata structures and single electron memory devices. Although numerous semiconductor materials are available and many examples in the literature cite success with fabricating a wide variety of semiconductor nanoparticles, this thesis focuses upon silicon. Silicon exhibits certain advantages over other semiconductor materials. Silicon is readily available and affordable in large sizes with a high degree of crystal perfection. It forms a high quality oxide (SiO_2) that has tremendous insulating properties, and both silicon and silicon dioxide have superior processing, thermal, and mechanical properties. A considerable amount of time, money, and capital has also been invested in utilizing silicon technology [1]. Furthermore, silicon is a material with mature technology such that extensive existing information can be used in manufacturing and integrating new silicon structures into devices. These existing resources, capital, and knowledge dedicated to silicon are invaluable and can play a vital role in integrating nanotechnology into existing devices and structure design. This thesis demonstrates that silicon nanoparticle devices can also be readily manufactured and are compatible with existing silicon-based device tools and technology. Silicon is also a material commonly found in devices, so minimal contamination from silicon integration occurs, unlike contamination issues associated with introducing another material, such as transition metal nanoparticles, into devices.

2.2.1 Optical Applications for Silicon Nanoparticles

Initial attempts to produce optical systems with semiconductor nanoparticles focused upon direct gap materials, such as GaAs, CdS, CdSe. Group IV semiconductor nanoparticles may have applications as light emitters because of their ability to produce room temperature visible photoluminescence. Compared to more commonly used light emitters, i.e., GaAs, InGaP, the Group IV semiconductors have low quantum efficiencies, typically ~ 10^{-4} to 10^{-5} [2],[3].

2.2.1.1 Silicon as an Indirect Bandgap Material

One disadvantage to working with silicon for optoelectronic applications is that bulk silicon is an indirect bandgap material and does not emit light or luminesce very efficiently. Luminescence is a radiative decay process. Light emission from a semiconductor first requires the excitation of an electron from the valence band to the conduction band via energy transfer. The subsequent recombination of this electron in the conduction band with a hole in the valence band leads to light emission only if the recombination energy of the electron-hole recombination process is given off as a photon, a process requiring both a conservation of energy and of momentum. Radiative decay processes must compete with nonradiative decay processes. In indirect bandgap materials like silicon, conservation of momentum requires a three-particle process; an electron and a hole must interact with specific phonons in order to decay radiatively. In general, this three-particle process is very slow and competes poorly with more rapid and favorable

nonradiative decay processes. Hence, bulk silicon is an inefficient luminescence material [4].

2.2.1.2 Porous Silicon and Nanocrystalline Silicon as Direct Bandgap Materials

Following Canham's observation [5],[6] that anodic etching of silicon wafers produces porous silicon that luminesces at relatively high external quantum efficiency of about 10% at room temperature and that the actual luminescent material is irregular nanostructured wires of crystalline silicon [7],[8], researchers pondered the future role of silicon nanoparticles in optoelectronic devices [9]. Indeed, Soref even claims that the Holy Grail of optoelectronics is the silicon "superchip" that contains "advanced silicon electronics with active silicon optics on a silicon substrate [10]." Delley and coworkers claim that a silicon nanoparticle with a diameter smaller than about 2 nm behaves as a direct bandgap material with an energy gap in the visible region [11]. Indeed, the luminescence efficiency of silicon is seen to increase in silicon nanoparticles since the three-particle process is no longer required to produce radiative decay.

2.2.2 Memory Applications for Silicon Nanoparticles

Despite the interest in applications of silicon nanoparticles for optoelectronic devices, this thesis concentrates upon the application for silicon nanoparticles in novel memory devices. A few examples in the literature report on the ability to store information using silicon nanoparticles [12], [13], [14]. Others report on single electron devices, including single electron transistors [15],[16] and logic devices [17], including

cellular automata structures [18],[19],[20],[21]. In order to understand the proposed use of silicon nanoparticles in these memory devices, it is first necessary to describe some simpler structures.

2.3 The MOSFET

2.3.1 MOSFET Structure

In the nanoparticle floating gate field effect memory device, the most basic structure is that of a transistor. The metal oxide semiconductor field effect transistor (MOSFET) as shown in Fig. 2.1 operates on the concept that a voltage applied to a conductive control gate is able to control the conductance of an underlying p- or n-type semiconductor. This semiconductor conductance is then used to control the current flowing in the channel between two highly doped regions in the silicon substrate, named the source and the drain. The MOSFET is simply a MOS-capacitor with 2 p-n junctions adjacent to the semiconductor region controlled by the MOS-gate. Detailed schematics, performance, and device physics of MOSFETs can be found in a number of references [22],[23],[24]. In this thesis, the subscript d refers to the drain node, s to the source node, sub to the substrate node, and g to the gate node. Voltages and currents are specified with V and I, respectively.

2.3.2 MOSFET Subthreshold Characteristics

A typical subthreshold characteristic for a MOSFET is shown in Fig. 2.2. At zero

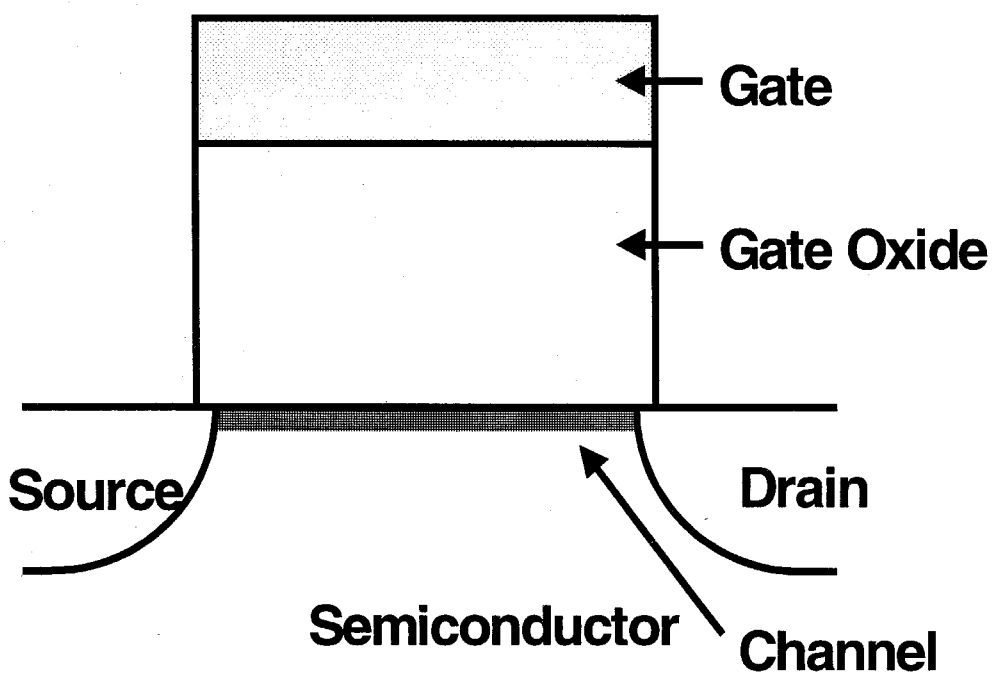

Figure 2.1: Metal-oxide-semiconductor field effect transistor (MOSFET) illustrating the features of a basic transistor.

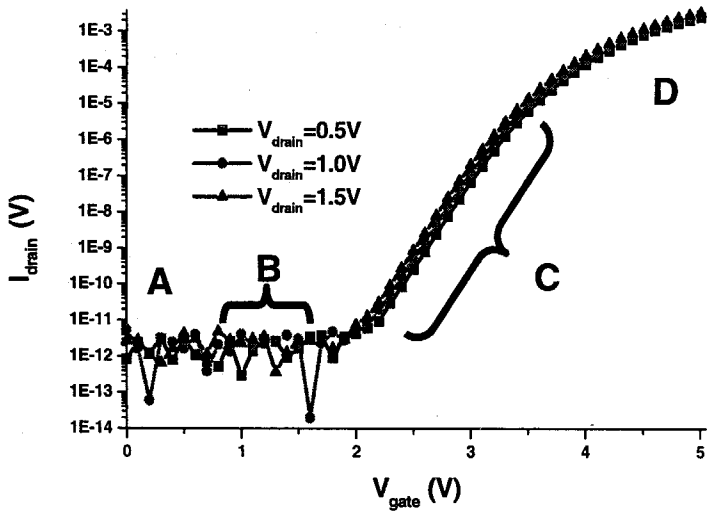

Figure 2.2: Subthreshold characteristic for typical MOSFET.

potential to the gate (Fig. 2.2, point A), the transistor is in thermal equilibrium and the transistor is in the off position; I_d is identically zero. No mobile carriers are available and, thus, no current flows between the source and the drain; the circuit between the source and drain is open. At V_g less than the depletion-inversion transition-point voltage, the channel contains very few electrons and no current is able to flow between the source and the drain; the circuit is open as shown in region B on Fig. 2.2. However, when V_g is greater than the depletion-inversion transition-point voltage, an inversion layer containing mobile electrons forms in the channel. Thus, the channel is now able to conduct current between the source and the drain and the transistor will turn on; the circuit between the source and drain is closed as shown in region C on Fig. 2.2. As the gate potential increases, the current flowing between the source and the drain rises. However, beyond a limiting value of V_g, the current saturates to its maximum value ($I_{d,sat}$ occurring at $V_{g,sat}$) near point D on Fig. 2.2 and subsequent increases in the gate potential will no longer increase the current flow between the source and the drain. At moderate gate potentials, the current between the source and drain is almost a linear function of the gate potential. The threshold voltage or V_t of the transistor can be defined in a number of ways as illustrated in Fig. 2.3. Ultimately, V_t corresponds to a V_g that causes the transistor to carry current at the onset of inversion.

2.3.3 MOSFET Output Characteristics

To understand the effect of V_d on the MOSFET performance, now consider the case where V_g is greater than the depletion-inversion transition point voltage as shown in

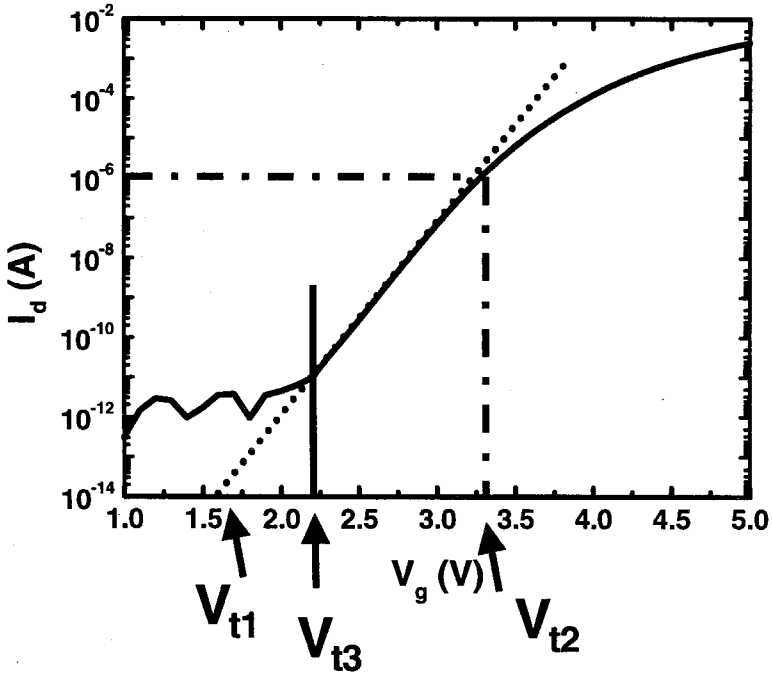

Figure 2.3: Various methods exist to determine V_t based upon the subthreshold characteristics of a MOSFET.

the typical MOSFET output characteristics in Fig. 2.4. Starting from $V_d = 0$, the drain bias is incrementally increased. At $V_d = 0$, the device is in thermal equilibrium and the source and drain circuit is open; $I_d = 0$. With small increases in V_d, the channel acts as a basic resistor. I_d is proportional to V_d, as shown in the linear region marked A in Fig. 2.4. As V_d continues to increase, the inversion region surrounding the drain grows. The number of carriers in the inversion layer decreases reducing the channel conductance. As shown in Fig. 2.4, this corresponds to a decreasing I_d vs. V_d slope marked B in Fig. 2.4. As V_d is further increased, the channel conductance continues to decrease and the I_d vs. V_d slope decreases. Eventually, the V_d becomes so large that the inversion layer around the drain disappears, causing the conducting channel near the drain to "pinch-off" and the slope of I_d vs. V_d begins to approach zero. The saturation drain bias at which this "pinch-off" occurs, $V_{d,sat}$, corresponds to point C in Fig. 2.4.

2.4 Conventional Floating Gate Memory Devices

Conceptually, conventional floating gate memory device comprises a transistor with a continuous conducting floating gate layer embedded within the control oxide as shown in Fig. 2.5. In a conventional floating gate MOSFET, a continuous conducting layer (i.e., 150 nm poly silicon) is embedded within the oxide region to produce a stacked gate structure. The floating gate is isolated from the underlying substrate channel by an insulating layer called the tunnel oxide and from the gate (or control gate) by an insulating layer called the gate (or control gate) oxide. By applying biases to the gate,

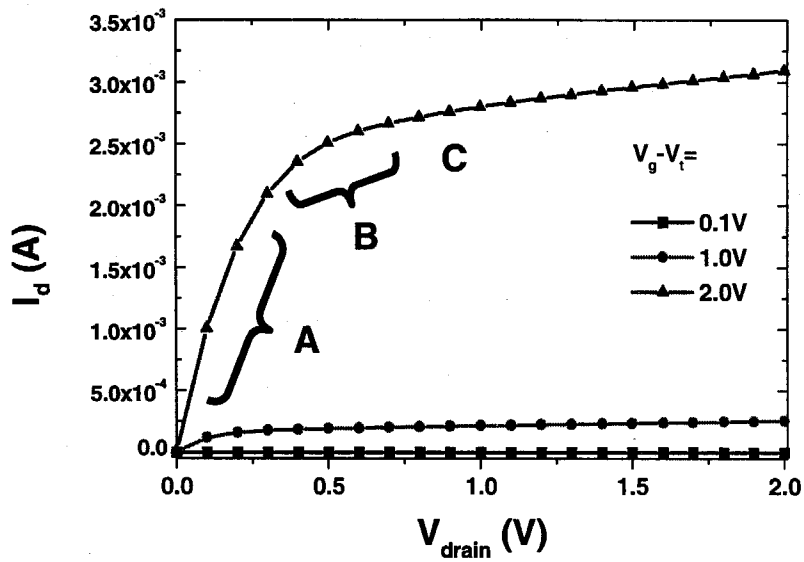

Figure 2.4: Output characteristic for typical MOSFET.

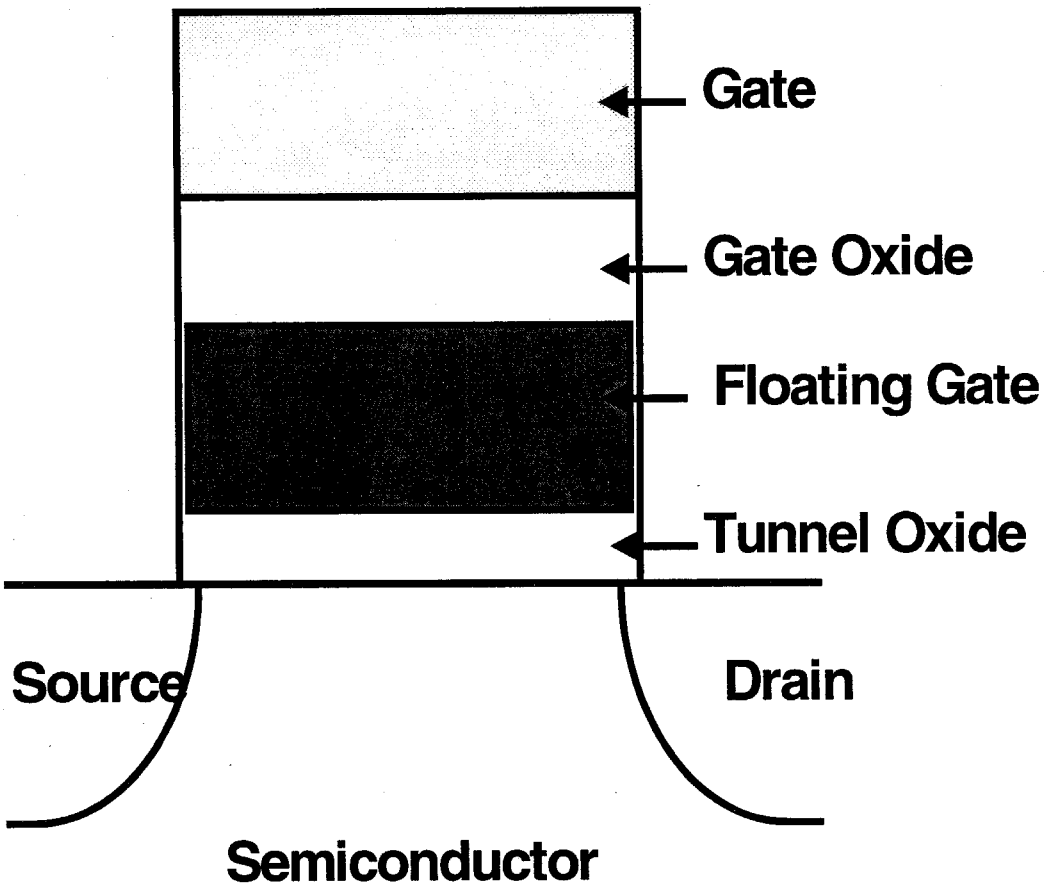

Figure 2.5: Conventional stacked-gate memory device.

drain, or substrate nodes of the floating gate MOSFET, it is possible to tunnel charge from the channel through the tunnel oxide into the floating gate as shown in Fig. 2.6. The amount of charge stored on the floating gate depends upon a number of factors, including tunnel oxide thickness, tunneling time, and applied biases. Once the biases are removed and if the floating gate is truly insulated from conductive regions, the charge is stored on the floating gate. This charge then acts as a "screen" between the control gate and the substrate. Incremental gate biases are then required to induce current flow between the source and drain. The shift in the gate voltage (or threshold voltage shift ΔV_t) required to turn on the device makes it possible to differentiate between a floating gate MOSFET that does not contain stored charge (lower V_t, erased) and a floating gate MOSFET that does contain stored charge (higher V_t, programmed) as shown in Fig. 2.7. As long as the ΔV_t between the programmed and erased states can be easily measured and is above the noise level, the floating gate MOSFET can be used to store information, thereby functioning as a memory device.

2.4.1 Issues for Conventional Floating Gate Memory Devices

In conventional floating gate memory devices, the isolation of the continuous floating gate material from the channel and gate is imperative. Defects in the floating gate layer or in the insulating oxide layers subject the memory device to catastrophic failure by leakage of the stored charge. Possible defects include a portion of the floating gate material shorting to the channel, enabling charge to easily and completely leak out of the floating gate. In another failure mode, defects in a poor quality oxide could transport

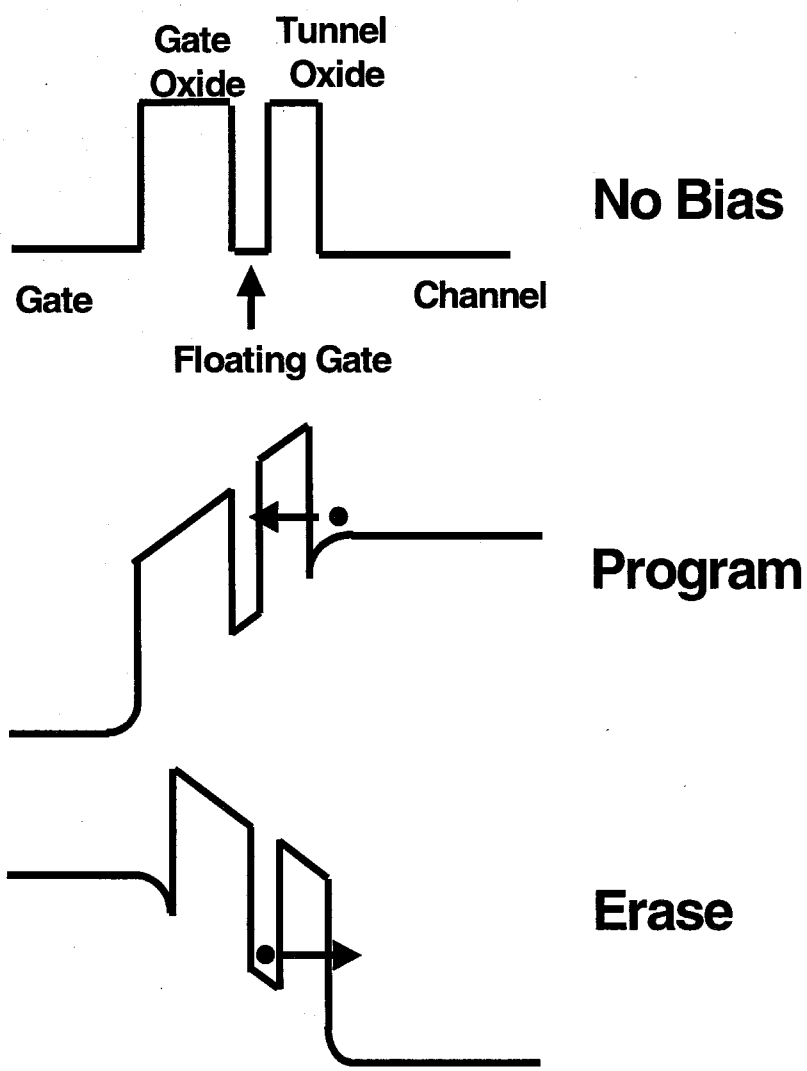

Figure 2.6: Program and erase behavior of nanoparticle floating gate memory devices.

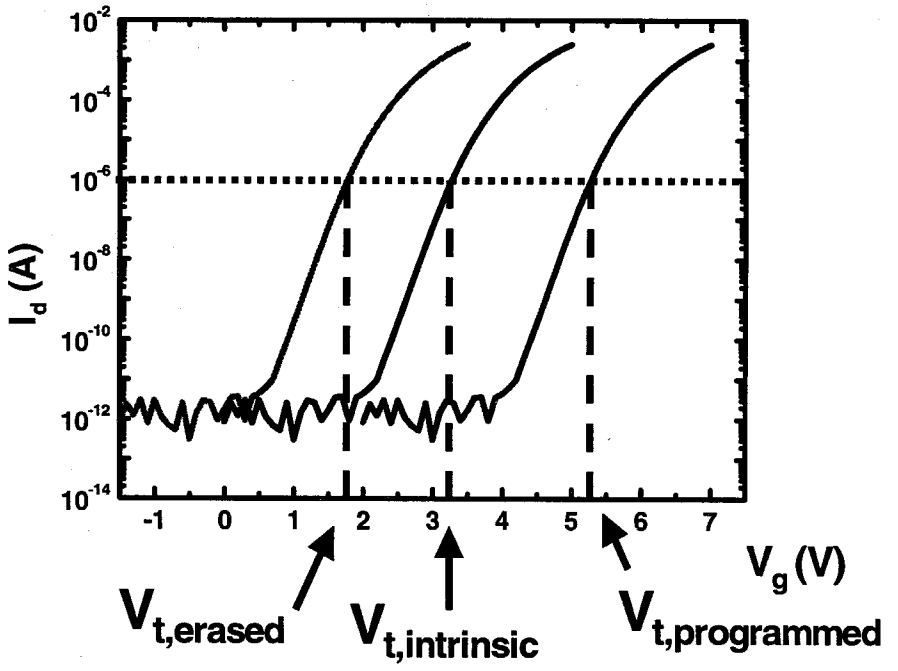

Figure 2.7: Subthreshold characteristics shift from left to right upon programming a device and shift from right to left upon erasing a device. The threshold voltage is measured consistently in all device states.

carriers from the floating gate into either the gate or the channel of the device. Since the floating gate is continuous, these defect sites would allow the loss of all stored charge on the floating gate to the channel. Therefore, high quality, thick oxide layers (typically ~ 10 - 25 nm) are required in effective floating gate devices. Thick oxide layers translate into increased program and erase times (because tunneling rate is retarded) and increased program and erase potentials (because electric fields at the floating gate are decreased). These increased voltage requirements demand high voltage power supplies for the device, increasing manufacturing and operating costs for these memories. Furthermore, because the floating gate is a thick (~ 150 nm) poly silicon layer, significant process challenges exist in the fabrication and etching of the stacked gate features, further increasing the manufacturing cost of the devices. One approach to overcoming these performance limitations and cost issues of the conventional floating gate MOSFET involves the use of electrically isolated silicon nanoparticles to produce a discontinuous floating gate silicon nanoparticle memory device with particular performance, processing, and cost advantages [12],[13],[14].

2.5 Nanoparticle-Based Floating Gate Memory Devices

Silicon nanoparticle-based floating gate MOSFETs are attractive candidates for terabit cm^{-2} density nonvolatile memory applications. As shown schematically in Fig. 2.8, nanoparticle floating gate MOSFETs are similar to a conventional floating gate MOSFET except that the nanoparticles replace the continuous poly silicon floating gate

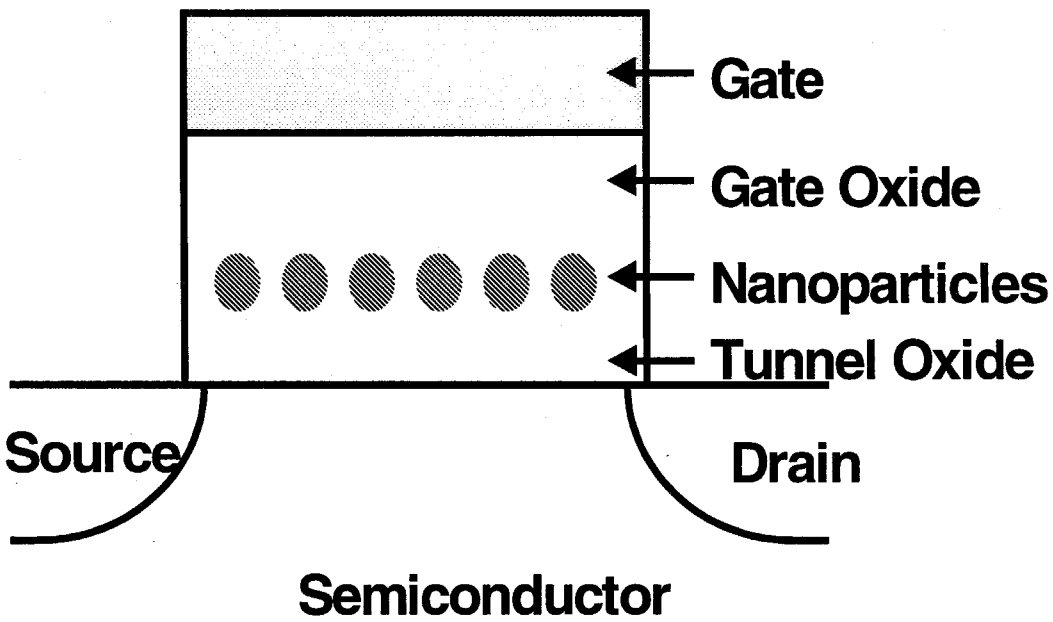

Figure 2.8: Nanoparticle-based floating gate memory device.

in conventional floating gate MOSFETs.

2.5.1 Issues for Nanoparticle-Based Floating Gate Memory Devices

Silicon nanoparticle floating gate memories may outperform conventional floating gate memory devices with faster read and write times, higher reliability, and lower power dissipation. These advantages derive from replacing the continuous poly silicon floating gate with discrete nanoparticles, making the memory device more defect-tolerant. In a conventional floating gate memory, insulation of the floating gate is imperative if charge is to be stored on the floating gate with any degree of reliability. Any defects in the floating gate or insulating oxide layers may lead to complete device failure. However, by replacing the continuous poly silicon floating gate with a discontinuous layer of discrete nanoparticles, the memory will still function even if ~ 10 to 20% of those nanoparticles lose their charge. Thus, insulation requirements in the nanoparticle floating gate memories are more forgiving, enabling thinner tunnel oxide dimensions, on the order of 1 to 4 nm. These thinner tunnel oxides, in turn, facilitate faster program and erase times and lower program and erase voltages. This eliminates the need for high voltage power supplies. Since the nanoparticle floating gate memories are truly nonvolatile, the charge stored on the floating gate during a program step is retained on the floating gate until removed by an erase process; memory refresh is not required. Furthermore, the conceptually simple silicon nanoparticle floating gate memories are easy to fabricate, requiring fewer processing steps than the conventional 150 nm poly silicon floating gate.

2.5.2 Previous Designs for Nanoparticle Nonvolatile Floating Gate Memory Device

Prior to the work discussed in this thesis, nonvolatile floating gate memory devices were fabricated by embedding silicon nanoparticles within the gate oxide of MOSFETs by either (i) implanting excess silicon into the gate oxide; or (ii) direct deposition of nanometer-scale silicon islands in the floating gate region by silicon chemical vapor deposition [12],[13],[14]. Within the gate oxide of a MOSFET, silicon nanoparticles act as charge storage elements. Injecting charge into the nanoparticle by tunneling from the channel alters the V_t of the transistor. In a normal write/read/erase cycle, information is written by charge injection, read by measuring the subthreshold current-voltage characteristic, and erased by tunneling charge back into the substrate as illustrated in Fig. 2.6. In previously fabricated devices, it was found that a single electron stored on each nanoparticle in an array with a nanoparticle density of ~ 10^{11} particles cm^{-2} with a 7 nm gate oxide resulted in a ΔV_t of 0.3 to 0.5 V that is easily detected at room temperature [12],[13],[14].

2.5.3 Towards an Aerosol Nanoparticle Nonvolatile Floating Gate Memory Device

For the previously discussed nanoparticle devices, it was determined that the program/erase speed of these nanoparticle devices was potentially limited by a distribution in charge transit times, charging voltages, and ΔV_t caused by a broad distribution in nanoparticle size, shape, position, oxide thickness, interface states, or shifts in the energy of electron levels due to quantum confinement effects [12],[13],[14]. Thus, fabricating nanoparticles in a way that is compatible with silicon ULSI processing,

combined with controlled particle size distribution and oxide thicknesses, and deposited on a substrate in a controlled manner with good control of electronic properties is vital to the development of high quality, reliable silicon nanoparticle-based nonvolatile floating gate memories. This thesis explores the synthesis and characterization of silicon nanoparticles nonvolatile floating gate memory devices using aerosol routes for silicon nanoparticle synthesis.

2.6 Summary

In this chapter, we have discussed a basic nanostructure called the nanoparticle. Applications for these nanoparticles include not only the nanoparticle floating gate memory devices, but also have important applications in optoelectronic devices and in logic devices. In these applications, the size of the nanoparticle is expected to play a pivotal role because of quantum confinement effects. We have mentioned the basic functional unit of the floating gate memory devices, namely the MOSFET, and we have provided some important details of the IV characteristics of a MOSFET. The structure of the conventional floating gate memory device was discussed and compared to that of a nanoparticle floating gate memory device. Silicon nanoparticle floating gate devices possess some clear advantages over conventional floating gate devices, including faster program/erase times, lower power requirements, and cheaper device fabrication.

However, in order to produce reliable devices with reproducible results, control over the nanoparticle size, interface states, oxide passivation, and two-dimensional

arrangement need to be controlled with high precision on the sub nm scale. The next few chapters deal exclusively with the aerosol synthesis of these nanoparticles. Not until Chapters 6, 7, and 8 will the nanoparticle devices and characterization be discussed in detail.

Bibliography

[1] R.T. Collins, P.M. Fauchet, and M.A. Tischler, "Porous Silicon: From Luminescence to LEDs," *Physics Today*, pp. 24-31 (January 1997).

[2] K.V. Shcheglov, C.M. Yang, K.J. Vahala, and H.A. Atwater, "Electroluminescence and Photoluminescence of Ge-Implanted $Si/SiO_2/Si$ Structures," *Appl. Phys. Lett.*, **66**, pp. 745-747 (1994).

[3] T.A. Burr and K.D. Dolenbrander, "Carrier Transport in Silicon Nanocrystallite-Based Multilayer Electroluminescent Devices," *Mat. Res. Soc. Symp. Proc.*, **405**, pp. 271-276 (1996).

[4] J.R. Haynes and W.C. Westphal, "Radiation Resulting from Recombination of Holes and Electrons in Silicon," *Phy. Rev.* **101**, pp. 1676-1678 (1956).

[5] V. Lehmann and U. Gösele, "Porous Silicon Formation: A Quantum Wire Effect," *Appl. Phys. Lett.*, **58**, pp. 856-858 (1991).

[6] L.T. Canham, "Silicon Quantum Wire Array Fabrication by Electrochemical and Chemical Dissolution of Wafers," *Appl. Phys. Lett.*, **57**, pp. 1046-1048 (1990).

[7] L.T. Canham, "Progress Toward Crystalline-Silicon-Based Light-Emitting Diodes," *MRS Bulletin*, pp. 22-28 (July 1993).

[8] P.M. Fauchet, L. Tsybeskov, C. Peng, S.P. Duttagupta, J. von Behren, Y. Kostoulas, J.M.V. Vandyshev, and K.D. Hirschman, "Light-Emitting Porous Silicon: Materials Science, Properties, and Device Applications," *IEEE J. Quant. Elect.*, **1**, pp. 1126-1139 (1995).

[9] K.S. Min, K.V. Shcheglov, C.M. Yang, H.A. Atwater, M.L. Brongersma, and

A.Polman, "Defect-Related Versus Excitonic Visible Light Emission from Ion Beam Synthesized Si Nanocrystals in SiO_2," *Appl. Phys. Lett.*, **69**, pp. 2033-2035 (1996).

[10] R.A. Soref, "Silicon-Based Optoelectronics," *Proc. IEEE,* **81**, pp. 1687-1706 (1993).

[11] B. Delley and E.F. Steigmeier, "Quantum Confinement in Si Nanocrystals," *Phys. Rev. B.*, **47**, pp. 1397-1400 (1993).

[12] S. Tiwari, F. Rana, H. Hanafi, A. Hartstein, E.F. Crabbe, and K. Chan, "A Silicon Nanocrystals Based Memory," *Appl. Phys. Lett.*, **68**, pp. 1377-1379 (1996).

[13] S. Tiwari, F. Rana, K. Chan, L. Shi, and H. Hanafi, "Single Charge and Confinement Effects in Nano-Crystal Memories," *Appl. Phys. Lett.*, **69**, pp. 1232-1234 (1996).

[14] H.I. Hanafi, S. Tiwari, and I. Khan, "Fast and Long Retention-Time Nano-Crystal Memory," *IEEE Trans. Electron Dev.*, **43**, pp. 1553-1558 (1996).

[15] L. Guo, E. Leobandung, and S.Y. Chou, "A Silicon Single-Electron Transistor Memory Operating at Room Temperature," *Science*, **275**, pp. 649-651 (1997).

[16] D.C. Ralphs, C.T. Black, and M. Trinkham, "Gate-Voltage Studies of Discrete Electronic States in Aluminum Nanoparticles," *Phys. Rev. Lett.*, **78**, pp. 4087-4090 (1997).

[17] H. Fahmy and K. Ismail, "Analysis of a Single-Electron Decimal Adder," *Appl. Phys. Lett.*, **70**, pp. 2613-2615 (1997).

[18] P.D. Tougaw, C.S. Lent, and W. Porod, "Bistable Saturation in Coupled Quantum-Dot Cells," *J. App. Phys.*, **74**, pp. 3558-3566 (1993).

[19] C.S. Lent and P.D. Tougaw, "Lines of Interacting Quantum-Dot Cells - A Binary Wire," *J. App. Phys.*, **74**, pp. 6227-6233 (1993).

[20] A. Gin, P.D. Tougaw, and S. Williams, "An Alternative Geometry for Quantum-Dot Cellular Automata," *J. App. Phys.*, **85**, pp. 8281-8286 (1999).

[21] J.R. Pasky, L. Henry, and P.D. Tougaw, "Regular Arrays of Quantum-Dot Cellular Automata 'Macrocells'," *J. App. Phys.*, **87**, pp. 8604-8609 (2000).

[22] S.M. Sze, *Semiconductor Devices Physics and Technology*, New York, John Wiley & Sons (1985).

[23] B.G. Streetman, *Solid State Electronic Devices,* 2nd ed., Englewood Cliffs, NJ, Prentice-Hall (1980).

[24] R.F Pierret and G.W. Neudeck, *Modular Series on Solid State Devices, Vol. IV: Field Effect Devices*, Reading, MA, Addison-Wesley (1983).

Chapter 3: Aerosol Synthesis of Uniformly-Sized Single Crystal Silicon Nanoparticles

3.1 Introduction

Aerosol synthesis routes have been used to fabricate semiconductor nanoparticles of a variety of semiconductor materials. Colloidal-phase reactions are the most common synthesis routes as discussed in greater detail in Chapter 4. An alternative approach, aerosol synthesis of semiconductor nanoparticles, enables control over the size distribution of particles of common semiconductor materials, making it an excellent method to control nanoparticle electronic properties. Vapor phase or aerosol synthesis of nanoparticles allows one to utilize important instrumentation and techniques used in aerosol systems to improve such things as nanoparticle size control and detection.

Previous work done by Camata and coworkers examined several synthesis routes for the production of aerosol silicon nanoparticles, including spark ablation, laser ablation, and thermal evaporation [1]. In this thesis, we produce aerosol silicon nanoparticles via dilute silane pyrolysis, similar to the aerosol silicon nanoparticle synthesis via dilute disilane [2],[3]. In any of these aerosol synthesis routes, the resulting nanoparticle aerosol can be monitored using aerosol instrumentation in order to achieve good control over such properties as particle size, shape, crystallinity, and surface passivation state.

In this chapter, we discuss the synthesis of aerosol silicon nanoparticles followed by *in situ* particle classification, detection, and deposition [1],[4]. The synthesis system consists of an aerosol nanoparticle source, an aerosol neutralizer to produce a stead state charge distribution, a radial differential mobility analyzer to classify the particles with respect to size, an aerosol concentration detector, and a nanoparticle collection device. Each of these instruments is briefly discussed in this chapter, along with performance models and typical operation conditions used to generate single crystal, spherical, nonagglomerated, uniformly-sized silicon nanoparticles for device applications.

3.2 Aerosol Formation and Particle Growth

Aerosol particles can be synthesized from any vapor source, such as from gaseous species or from vaporized material produced by ablating or evaporating a solid material. Regardless of the precursor material and method, the essential requirement for aerosol synthesis is the generation of a supersaturated vapor of material. At high supersaturation, vapor nucleates into very small particles as shown in Fig. 3.1. These particles act as seeds for particle growth by gas-to-particle or particle-to-particle conversions, such as chemical vapor deposition, vapor condensation, Brownian diffusion, and particle coagulation and coalescence. As particles continue to grow and the aerosol begins to cool, particle coagulation can continue. However, if sufficient thermal energy is not available, then particle coalescence is unable to proceed. The resulting aerosol is populated exclusively by fractal-like structures called agglomerates. Details of particle

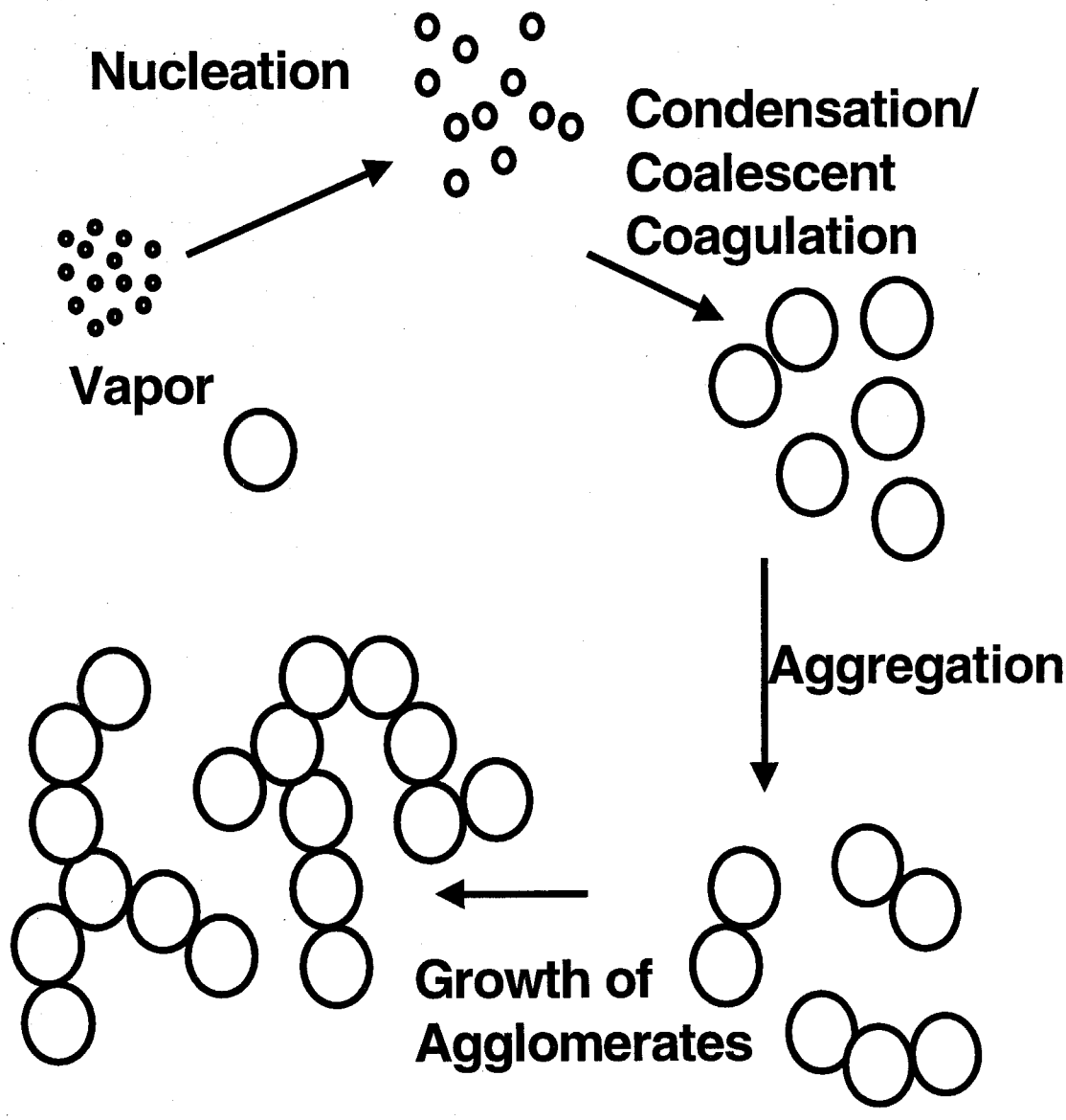

Figure 3.1: Formation and growth of an aerosol particle population.

formation and growth mechanisms can be found in several references [1],[5],[6].

In this thesis, we produce single crystal, nonagglomerated silicon nanoparticle aerosol by the pyrolysis of dilute silane in N_2 in a continuous flow reactor shown in Fig. 3.2. Silane pyrolysis forms an aerosol of silicon nanoparticles in the high temperature reactor depicted in Fig. 3.2. Ultrahigh purity (UHP) N_2 flows through an oxygen getter (<1ppb oxygen) and splits into two flows. A 750 sccm dilution flow of UHP N_2 combines with <1 sccm of 5000 ppm SiH_4 in N_2. This flow enters a 950°C furnace where SiH_4 pyrolyzes in a 3 mm outer / 2 mm inner diameter quartz tube labeled A in Fig. 3.2. Particles form by homogeneous nucleation and grow by vapor deposition and coagulation for about 30 ms, the residence time in the inner quartz tube. An annular quenching flow of 750 sccm UHP N_2 then dilutes the aerosol to suppress further particle coagulation at point B in Fig. 3.2. The annular flow also limits particle deposition on the quartz tube walls. This flow continues through a 9 mm outer / 7 mm inner diameter quartz tube in the 950°C furnace where the particles are sintered for 1.5 s to produce dense, spherical, single-crystal nanoparticles along C in Fig. 3.2.

The sintering of silicon nanoparticles has been extensively studied by Lunden and coworkers. From Lunden's work, we know that in order to sinter silicon nanoparticles, the aerosol must be completely oxygen-free [6]. The presence of oxygen in the pyrolysis furnace would inevitably lead to the production of SiO_x particles, not silicon particles. Moreover, even trace oxygen suppresses surface diffusion thereby inhibiting the sintering of the silicon nanoparticle aggregates [7] that form by coagulation. Without sintering, dense single crystal particles cannot be produced.

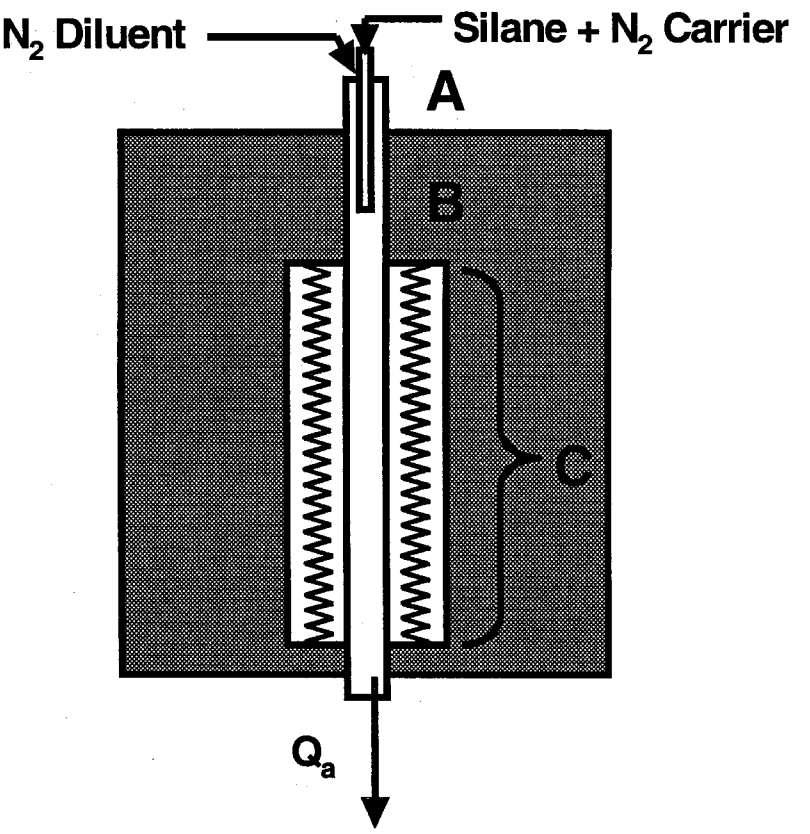

Figure 3.2: Schematic of the silicon nanoparticle pyrolysis and sintering furnace illustrating the annular design of the reactor tubes.

The average particle size can be controlled between 3 and 50 nm, depending upon the flow rate of the dilute silane and the flow rates of the dilution and quenching UHP nitrogen gases. When no quenching gas is added, single particles are not formed at high concentrations (~ 10^7 particles cm^{-3}) and particle agglomerates dominate. However, with a 1:1 dilution of aerosol to quenching gas, particle agglomeration is suppressed, producing single particle aerosol.

3.3 Aerosol Size Classification

Once formed and sintered, the aerosol particles are then charged and subsequently classified with a radial differential mobility analyzer (RDMA)[8],[9]. The RDMA has been extensively characterized in the work by Zhang and coworkers [8],[9] and has also been used by Camata and coworkers to produce classified aerosol silicon nanoparticles [1],[4].

The RDMA is a parallel plate capacitor with radial symmetry as shown in Fig. 3.3. Positively charged nanoparticles enter through the aerosol port and migrate radially inward across a particle-free laminar sheath flow in the presence of an applied negative electric field. Ideally, the particles carry only one elementary charge, in which case their mobility is only dependent on their diameter. For this reason, nanoparticles with different sizes follow different trajectories within the RDMA. At the center of the RDMA is a sampling port in which the classified nanoparticles are removed. Uncharged and large, low mobility particles exit the RDMA with the excess flow. High mobility particles that

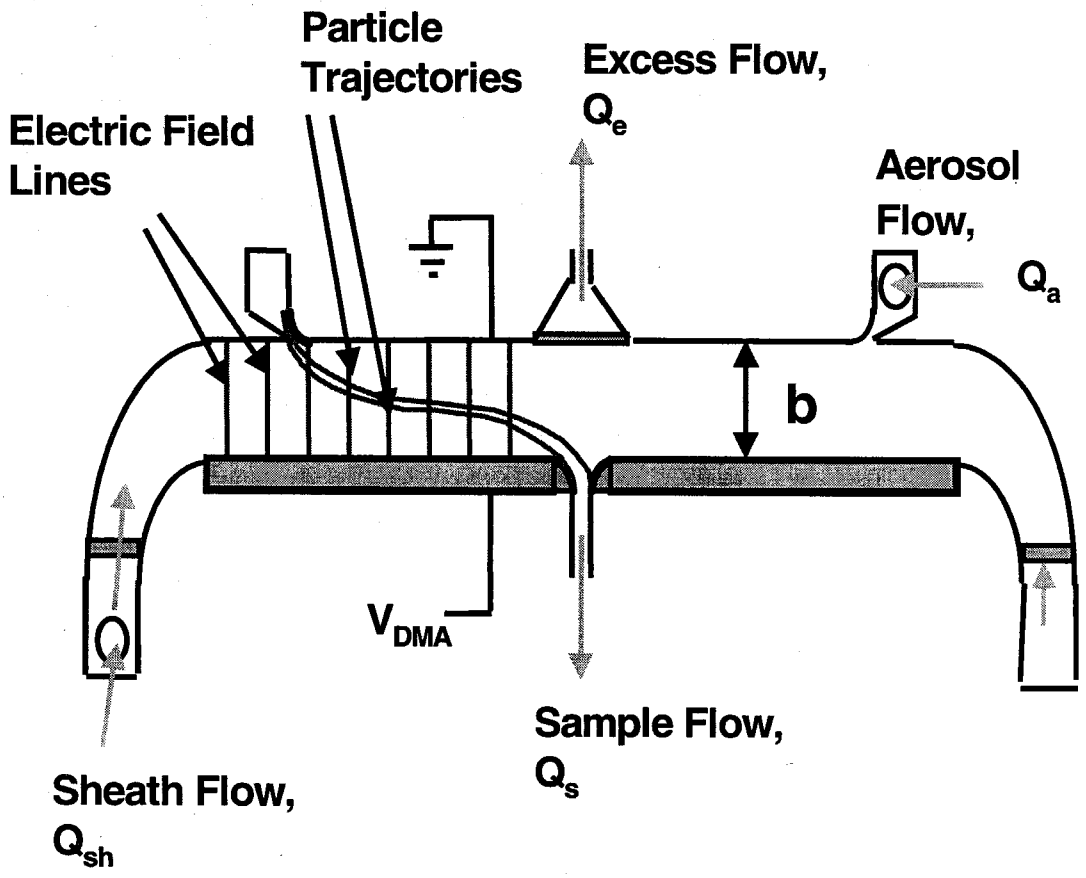

Figure 3.3: Schematic of radial differential mobility analyzer cross section.

are smaller than the target size deposit on the counter electrode of the RDMA. The flow rates and the applied voltage determine the mobility and, hence, diameter of the nanoparticles that are transmitted in the classified sample flow. By varying the voltage applied to the RDMA, the mobility (and, thus, the particle size) of the classified particles can be controlled.

Although details of particle size classification have been discussed elsewhere [1],[4],[8],[9], the size classification of aerosol silicon nanoparticles is vital to this project and will be briefly discussed here. As shown in Fig. 3.3, the RDMA is a parallel plate capacitor with a plate separation b, applied voltage V, and laminar gas velocity **u** and viscosity μ. By neglecting diffusion, the mobility of charged aerosol particles can be described by a balance between electrostatic and drag forces

$$m\frac{dv}{dt} = \frac{3\pi\mu D_p}{C_c}(u - v) + qE_z \qquad (3.1)$$

where m, D_p, and q are the particle mass, diameter, and electric charge. $\mathbf{E}_z$ is the electric field. C_c is the Cunningham slip correction factor that describes deviations from drag forces for particles that are small compared to the mean free path of gas molecules. C_c can be calculated from

$$C_c = 1 + Kn[\alpha + \beta \exp(\frac{-\gamma}{Kn})] \qquad (3.2)$$

where the Knudsen number, Kn, is a dimensionless number defined by

$$Kn = \frac{2\lambda}{D_p} \tag{3.3}$$

and represents the ratio of the gas mean free path, λ, to the particle radius. The values for α, β, and γ have been experimentally determined for $0.001 < Kn < 100$ and are $\alpha = 1.257$, $\beta = 0.40$, and $\gamma = 1.10$. At steady state, eqn (1) reduces to

$$v_e = Z_p E \tag{3.4}$$

where v_e is the particle migration velocity parallel to the direction of the applied electric field and Z_p is the particle electric mobility where

$$Z_p = \frac{qC_c}{3\pi\mu D_p} \tag{3.5}$$

The current design of the RDMA allows 85% transmission efficiency for 3 nm particles, making this instrument suitable for the classification of nanoparticles [9]. A sample of 5 nm classified nanoparticles in TEM as shown in Fig. 3.4 illustrates that the particles are ~ 5nm diameter, single particles, nonagglomerated, spherical. The diffraction pattern and dark field demonstrates the crystalline nature of these nanoparticles.

Since RDMAs can be used to classify aerosol particles (fixed V) or to measure the size distribution (scan V), this thesis also discusses the use of a tandem RDMA experiment. In this set-up, the aerosol nanoparticles are classified with the first RDMA accomplished by fixing the applied voltage to the bottom electrode. After processing this classified aerosol in an oxidation furnace, for example (details are found in Chapter 5),

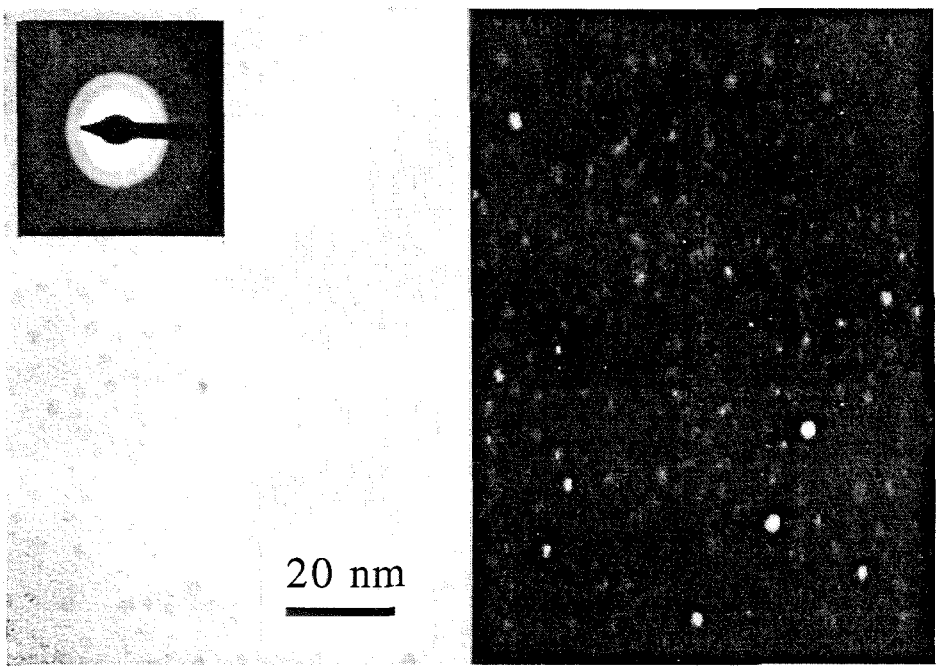

Figure 3.4: Bright field/dark field TEM of 5 nm classified silicon nanoparticles.

the nanoparticles are flowed into the second RDMA to measure the new particle size distribution by scanning over a wide range of voltages. In all cases, charged aerosol particle concentrations are measured with an electrometer with femtoampere sensitivity. Small changes in the nm size range can be detected in the tandem RDMA experiments.

3.3.1 Particle Charging

In order for nanoparticles to be classified with the RDMA, they must first be charged. Many designs exist for the instrument known as the "aerosol neutralizer." Further discussion and governing equations on charge distributions as a function of particle size can be found in other sources [10]. In this work, we use a radioactive bipolar charger. In this aerosol neutralizer, the aerosol and carrier gas are exposed to an ambipolar cloud of N_2 ions produced by a ^{85}Kr radioactive source. In this device, a small fraction of the nanoparticles become charged, with most of those carrying just one charge. Reactions of the aerosol particles with the ambipolar gas ions impart a known charge distribution on the particles. This charge distribution is particle size dependent. In the nm size range, multiple charging of particles is virtually impossible. Furthermore, the single charging efficiency in the nm size range (from 1 - 10 nm) only approaches ~ 0.1 - 1%, meaning that a loss of 99 - 99.9% of particles through the RDMA will occur simply because of the high number of uncharged (and, thus, unclassifiable) particles. The aerosol particle concentration can be monitored throughout the synthesis process by flowing a portion of the classified aerosol flow into an electrometer with femtoampere sensitivity. By varying the voltage applied to the RDMA and detecting the particle

concentration from the electrometer, the particle size distribution of the silicon nanoparticles exiting the furnace is measured. Two types of samples are analyzed in this thesis, namely classified and unclassified samples. Classified samples are produced by setting the RDMA to a given voltage throughout the entire collection period. The unclassified samples are collected as colloids directly downstream from the furnace without mobility classification or by electrostatic precipitation directly following the aerosol neutralizer.

3.4 Particle Collection

Nanoparticles are collected either on substrates or into liquids to form nanoparticle colloids. The colloid collection will be discussed in detail in Chapter. 4. For nanoparticle collection onto substrates and onto TEM grids, we use both electrostatic (or electrophoretic) precipitation and thermophoretic deposition. Impaction of nanoparticles, although possible under hypersonic and supersonic velocities, will not be discussed here [11].

3.4.1 Electrostatic Precipitation

Electrostatic precipitation is a well-known method used to extract charged particles from an aerosol stream and to collect them onto oppositely charged substrates (ref). In this method, an aerosol stream containing charged particles passes through a nozzle with radius R_0 toward an oppositely charged substrate a distance L from the

nozzle. In this nozzle-to-plane electrostatic precipitation, the resulting particle deposition velocity, v_{ED}, can be calculated from

$$v_{ED} = \frac{Q_{ED}L}{2\pi Z_p R(R - R_0)} \tag{3.6}$$

where Q_{ED} is the volumetric flow rate through the nozzle and R is the resulting particle deposit radius on the substrate. Z_p is the particle electrical mobility defined in Eqn. 3.5. For singly charged 10 nm particles, a 20kV/cm electric field produces v_{ED} values of ~ 400 cm/s, velocities insufficient to cause particle deformation upon deposition onto substrates. Since classified nanoparticles must be charged prior to classification, electrostatic precipitation is the preferred method for particle collection in classified aerosol samples.

Electrostatic precipitation is used to collect charged aerosol particles directly on transmission electron microscopy (TEM) grids or other substrates for subsequent analyses. A rod supports a secured TEM grid or substrate 1 mm away from a 2 mm diameter nozzle through which the aerosol passes. A negative ~ 1kV potential is then applied to the rod. The resulting particle deposition is random. At high coverages, the particles tend to agglomerate, often forming three-dimensional structures, especially at the substrate center (corresponding to the center axis of the nozzle). To prevent post-deposition agglomeration, low density deposits (<5% coverage) are used to examine the structures of the particles as they exist in the aerosol phase.

3.4.2 Thermophoretic Deposition

In cases where nanoparticles are not classified or charged prior to collecting, the more favorable collection method known as thermophoretic deposition is used. Thermophoretic deposition does not depend upon particles being charged. Thus, the collection efficiency is higher (remember that charging efficiency for nm sized particles is ~ 0.1 - 1%). The thermophoretic deposition method utilizes the fact that aerosol particles migrate in the presence of a temperature gradient from higher temperatures to lower ones [12]. The basic principle for thermophoretic deposition is that hot gases contain faster moving, higher energetic molecules that hit the particle, moving it toward the cooler gases. The cooler gas molecules also have momentum, but hit the particle with less energy and less frequently. The net result is particle motion from hot gas toward cool gas and can be described by the following equation [5]:

$$v_T = -\frac{Th\mu \frac{dT}{dx}}{\rho T} \tag{3.7}$$

where v_T is the thermophoretic velocity of the particle, dT/dx is the temperature gradient in the direction of particle motion, μ and ρ are the viscosity of gas and particle density, respectively, and T is the gas temperature. Th is a dimensionless thermal number that is assumed to be particle size independent in the nm size regime. Experimental values for Th ~ 0.5 [13]. As will be discussed in Ch. 6, thermophoretic deposition is the preferred method for floating gate deposition since particles are uncharged and because

thermophoretic deposition does not cause any contamination issues within the ultra clean deposition chamber.

3.5 Summary

In this chapter, we discussed the basic mechanisms for aerosol silicon nanoparticle formation from dilute silane. As with any aerosol formation process, supersaturated vapor was formed at elevated temperatures by pyrolyzing silane. Particles continued to grow by silicon chemical vapor deposition. To suppress agglomeration, the aerosol concentration was quenched at 1:1 flow ratio by adding in a separate particle free N_2 stream. By allowing particles to flow through the hot zone of a tube reactor, sufficient thermal energy was added to the aerosol to allow the particles to sinter. The pyrolysis and sintering reactor was modified at different locations within the reactor to control the resulting nanoparticle aerosol such that dense, spherical, single-crystal, nonagglomerated particles are produced. The discussion then described the RDMA as a useful instrument to classify nanoparticles and to measure particle size distributions. Two commonly employed deposition techniques, namely electrostatic precipitation and thermophoretic deposition, were discussed. A third collection technique, colloidal collection, will be discussed in Chapter 4.

Bibliography

[1] R.P. Camata, "Aerosol Synthesis and Characterization of Silicon Nanocrystals," Caltech Thesis (1997).

[2] K.A. Littau, P.J. Szajowski, A.J. Muller, A.R. Kortan, and L.E. Brus, "A Luminescence Silicon Nanocrystal Colloid via a High-Temperature Aerosol Reaction," *J. Phys. Chem.*, **97**, pp. 1224-1230 (1993).

[3] W.L. Wilson, P.F. Szajowski, and L.E. Brus, "Quantum Confinement in Size-Selected Surface-Oxidized Silicon Nanocrystals," *Science*, **262**, pp. 1242-1244 (1993).

[4] R.P. Camata, H.A. Atwater, K.J. Vahala, and R.C. Flagan, "Size Classification of Silicon Nanocrystals," *Appl. Phys. Lett.*, **68**, pp. 3162-3164 (1996).

[5] R.C. Flagan and M.M. Lunden, "Particle Structure Control in Nanoparticle Synthesis from the Vapor Phase," *Mat. Sci. Eng. A-Struct.*, **204**, pp. 113-124 (1996).

[6] M.M. Lunden, "Particle Structure Control in Nanoparticle Synthesis from the Vapor Phase," Caltech Thesis (1996).

[7] M.K. Alam and R.C. Flagan, "Controlled Nucleation Aerosol Reactors - Production of Bulk Silicon," *Aerosol Sci. Tech.* **5**, pp. 237-248 (1986).

[8] S.H. Zhang and R.C. Flagan, "Resolution of the Radial Differential Mobility Analyzer for Ultrafine Particles," *J. Aerosol Sci.* **27**, pp. 1179-1200 (1996).

[9] S.H. Zhang, Y. Akutsu, L.M. Russell, R.C. Flagan, and J.H. Seinfeld, "Radial

Differential Mobility Analyzer," *Aerosol Sci. Technol.*, **23**, pp. 357-372 (1995).

[10] A. Wiendensohler, "An Approximation of the Bipolar Charge Distribution for Particles in the Submicron Size Range," *J. Aerosol Sci.*, **13**, pp. 537-547 (1982).

[11] J. Fernandez del la Mora, S.V. Hering, N. Rao, and P.H. McMurry, "Hypersonic Impaction of Ultrafine particles," *J. Aerosol Sci.*, **21**, pp. 169-187 (1990).

[12] L. Talbot, R.K. Cheng, R.W. Schefer, and D.R. Willis, "Thermophoresis of Particles in a Heated Boundary Layer," *J. Fluid Mech.*, 101, 737-758 (1980).

[13] R.C. Flagan and J.H. Seinfeld, *Fundamentals of Air Pollution Engineering*, Prentice Hall, Englewood Cliffs, NJ (1988).

Chapter 4: Colloid Formation and Particle Size Changes in Colloidal Processing of Silicon Nanoparticles

4.1 Introduction

As discussed in the previous chapters, silicon nanoparticles may have important applications in nonvolatile floating gate memory devices. To prevent device performance variations, particle size and oxide thicknesses may need to be controlled with a high degree of precision. Additionally, producing well-ordered two-dimensional arrays of nanoparticles may require the exploitation of self-assembly techniques and colloidal forces, which in turn, requires that silicon nanoparticles first come into contact with liquids.

Until recently, colloid formation with silicon nanoparticles was assumed to be inert. In fact, silicon nanoparticles produced in the aerosol phase by dilute silane pyrolysis and size classified with a radial differential mobility analyzer undergo a size reduction upon collection in ethylene glycol, water, and ethanol. Unclassified polydisperse silicon aerosol nanoparticles with an average diameter of 11 nm and geometric standard deviation $\sigma_g \sim 1.9$ become monodisperse when collected in a colloid and have a final particle diameter of 2-5 nm and $\sigma_g \sim 1.1$. High resolution transmission electron

microscopy shows that these particles have an amorphous oxide layer of 1 nm, possibly from the presence of dissolved oxygen in the solvent. Previous to colloid collection, these nanoparticles were kept in an oxygen-free environment within the aerosol reactor, so oxidation could not occur before colloid collection. Particles collected in water do not become completely oxidized, even after a year of storage. Experimental evidence also suggests that silicon nanoparticles collected in ethanol undergo a reaction with ethanol to produce tetraalkylorthosilicate-like species. The fact that aerosol-synthesized silicon nanoparticles undergo size reduction due to etching upon collection in ethylene glycol, water, and ethanol, is correlated with the presence of dissolved oxygen in the solvent. Reducing dissolved oxygen to < 3 ppt diminishes the reactivity between the silicon nanoparticles and the solvent molecules, eliminating particle diameter reductions in these solvents.

Our results with silicon nanoparticle collection in ethylene glycol, ethanol, and water suggest that colloidal particles may not be inert. Substantial changes in particle characteristics occur after collection in these solvents. Literature describing reactions between silicon and organic molecules and solvents are common [1],[2],[3],[4],[5] and between silica surfaces and organic molecules to produce organic layers on silica [6]. Literature on the reactivity of silicon surfaces to halogens have also been widely reported [7],[8] and offer ways to silanize oxidized silicon wafers [9],[10],[11]. Studies of silicon wafer dissolution in ethylene glycol report that silica surfaces react to form an alkoxy-modified surface, producing a clear, cross-linked polymer identified as $Si(OCH_2CH_2O)_x$ [12]. Furthermore, reactions of silica in alcohols in general and in

ethanol specifically are well known [13],[14]. The Stöber process is used to produce monodisperse silica spheres from tetraethoxysilane (TEOS) in a basic ethanol solution [15]. Ordered microporous structures called zeolites are also produced from solution-phase reactions of TEOS, although solid sources of silica are also used. Both processes begin with the formation of a gel with a nanometer-scale structure [16]. The disordered network can then organize into the uniform silica spheres or into the zeolite crystalline structure if permitted.

Our results suggest that a reaction product such as TEOS or a related compound forms between silicon nanoparticles and ethanol. In this chapter, we report on the size reduction between aerosol-synthesized and colloidally dispersed particles that occurs upon collection in solvents, and suggest ways to prevent reactions between silicon nanoparticles and solvent molecules while simultaneously producing highly concentrated silicon nanoparticle colloidal solutions (~20% particles by volume).

4.2 Colloidal Synthesis

The controlled synthesis and deposition of nanoparticles has been widely studied. A common synthesis route is to produce nanoparticles directly in the liquid phase so that the final product is a stable colloid of nanoparticles. The stabilization of the particles is usually accomplished by capping or passivating the surface with molecules that covalently attach to the particle and that have a lyophilic group that interacts favorably with the solvent. Particle formation and passivation can occur in the same reaction

mixture; examples include phosphine capped CdSe, CdS, and CdTe [17] and alkyl thiol capped Au [18],[19],[20]. Whereas stable colloids can be formed by chemisorbing an ambiphylic species on the particle surface to impart a steric repulsive force between particles, an unstable colloid occurs when there is no repulsive force strong enough to balance the attractive van der Waals attractions between particles. In an unstable colloid, particle clusters become so massive that they sediment out of solution.

4.2.1 Size Selective Precipitation

The instabilities in unstable colloids can be used to separate colloidal particles according to their sizes to produce monodisperse particle colloids. In size selective precipitation (SSP), an initially stable colloid gradually becomes more unstable by the dropwise addition of a second miscible solvent that imparts a less favorable interaction between the steric stabilizing molecule and solvent, reducing the energetic barrier to flocculation [17],[21]. Since the largest particles experience the greatest van der Waals forces, they are the first to flocculate upon nonsolvent addition. After centrifugation, the precipitate is enriched in the largest particles, and the supernatant is depleted of these largest particles. Thus, both the precipitate and the supernatant become more monodisperse after each SSP step. The precipitate can be resuspended in the original solvent to produce a stable colloid.

4.3 Formation of Ordered Arrays of Colloidal Nanoparticles

Stabilized colloids can be used to produce well ordered close-packed two-dimensional arrays of nanoparticles through Langmuir-Blodgett films, by self-assembly, or by electrophoretic deposition.

4.3.1 Langmuir-Blodgett Films and Self-Assembly

In work by Daboussi and coworkers, the alkyl stabilized nanoparticles themselves act as the traditional amphiphiles used in Langmuir-Blodgett techniques [22]. The nanoparticles are the hydrophilic portion and the exposed alkyl groups are the hydrophobic surfaces. Alkyl thiol stabilized gold nanoparticles have been self-assembled into close-packed structures. After the formation of the close-packed monolayer, the nanoparticles are covalently linked together by organic interconnects that displace the alkyl thiol molecules, thereby stabilizing the particles. The result is a two-dimensional superlattice of covalently coupled gold nanoparticles [8].

4.3.2 Electrophoretic Deposition

Electrophoretic deposition produces well-ordered nanoparticle arrays that can be lifted off of a liquid surface onto a solid substrate to produce close-packed arrays on substrates [23]. Electrophoretic deposition involves the movement of charged particles by applying a DC electric field, resulting in the deposition of particles on the oppositely charged electrode [24],[25]. The first necessary step in electrophoretic deposition is the formation of a stable colloidal suspension of particles such that the attractive Van der Waals forces are balanced by the repulsive double layer forces that are present in charged

particle colloids. The double layer forces are very sensitive to pH and electrolyte concentrations. Thus, these parameters can be used to modify and control the deposition of particles. Electrophoretic deposition has been used to fabricate layered structures by changing the suspension and deposition conditions [26],[27]. Electrophoretic deposition has also been used to fabricate ordered two-dimensional arrays of gold nanoparticles [28],[29].

4.4 Silicon Nanoparticle Synthesis

Colloidal synthesis of silicon nanoparticles has proven to be much more difficult to achieve. Colloidal suspensions of silicon nanoparticles have been produced by dispersal of porous silicon from electrochemically etched wafers [30],[31], albeit with little control over particle size and by silicon precipitation from supercritical solutions [32]. Several groups report the collection of 3 to 7 nm aerosol synthesized silicon nanoparticles in ethylene glycol that have also been passivated with an oxide shell of 1 nm by aerosol phase thermal oxidation and by colloidal phase oxidation [33],[34]. Aerosols of silicon nanoparticles have also been produced by pyrolysis of silane and disilane [35]. Camata also produced aerosol silicon nanoparticles by thermal evaporation [36], laser ablation, and spark ablation [37]. Following synthesis, Camata and coworkers narrowed the size distribution of thermal evaporation synthesized aerosol silicon nanoparticles with a radial differential mobility analyzer (RDMA) discussed in Chapter 3 [35],[36]. We generate monodisperse aerosol silicon nanoparticles by controlled

pyrolysis of dilute silane followed by differential mobility classification of the resulting polydisperse aerosol. In this chapter, we describe investigations of colloidal collection, processing, and reactivity of these aerosol silicon nanoparticles.

4.5 Aerosol Particle Formation and Classification

Nanoparticles are formed, classified, and detected by the procedure described in Chapter 3. Essentially, aerosol silicon nanoparticles are produced in a silane pyrolysis/sintering reactor to produce uniformly sized, nonagglomerated, single crystal silicon nanoparticles illustrated in Fig. 4.1. They are charged with ambipolar gas ions in an aerosol neutralizer, classified in an RDMA, and a portion of the classified aerosol flow is detected with an electrometer with femtoampere sensitivity. The remaining classified aerosol is collected either by electrostatic precipitation or thermophoretic deposition onto substrates. Two types of samples are analyzed in this chapter, namely classified and unclassified samples. Classified samples are produced by setting the RDMA to a given voltage throughout the entire collection period. The unclassified samples are collected without mobility classification as colloids directly downstream from the furnace or by electrostatic precipitation directly following the aerosol neutralizer (Fig. 4.1). In unclassified samples, the RDMA is completely bypassed.

4.6 Colloid Collection of Aerosol Nanoparticles

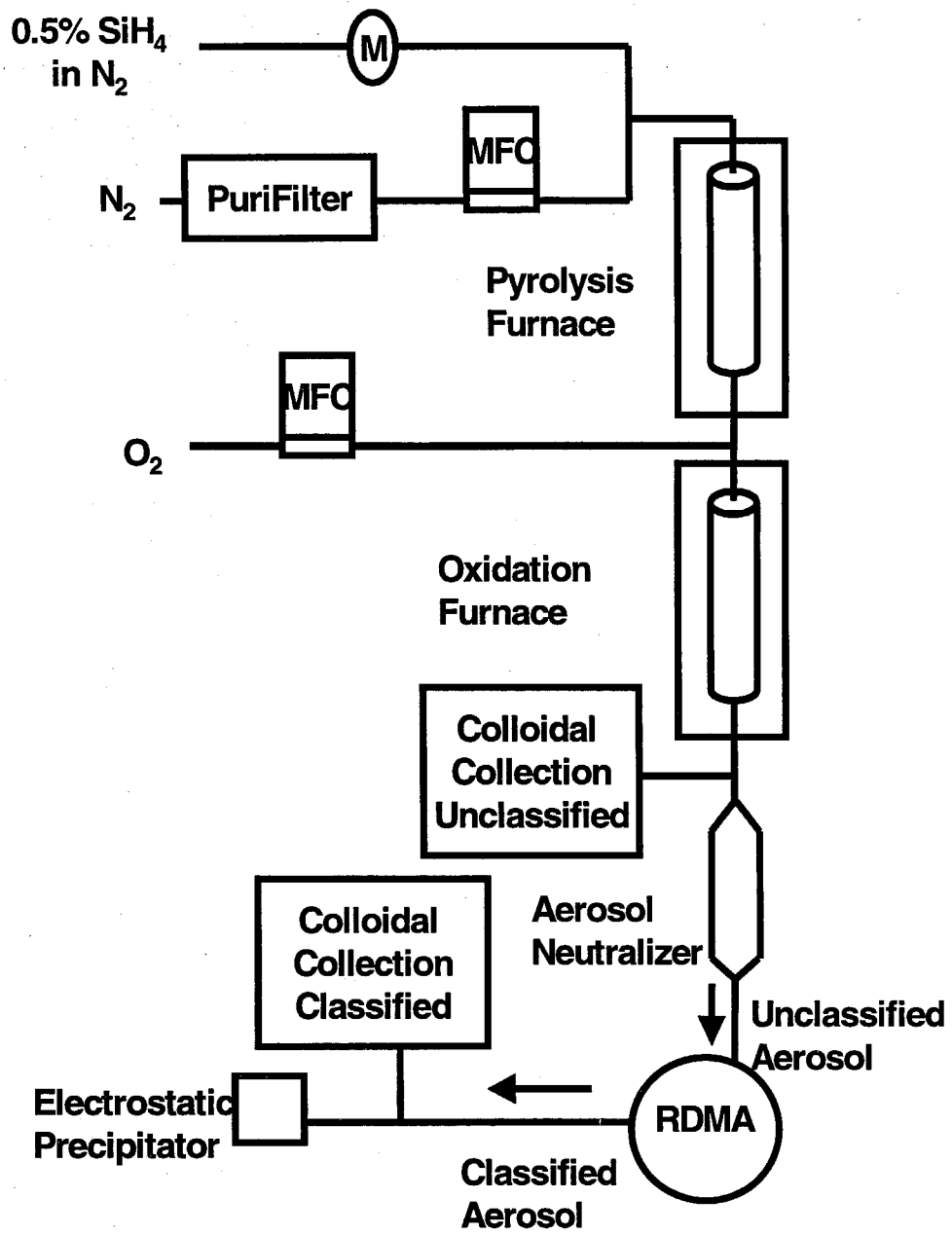

Figure 4.1: Aerosol reactor for the collection of electrostatic samples and classified and unclassified colloid samples.

This chapter concentrates on the formation of nanoparticle colloids from aerosol-synthesized nanoparticles using two different colloid collection methods, referred to as bubbled colloids and condensation colloids.

4.6.1 Bubbled Colloids

Nanoparticles have been collected as bubbled colloids by passing the aerosol through a 50μm pore size glass frit and bubbling it into a liquid, the colloid solvent as shown schematically in Fig. 4.2. Water, ethylene glycol, and ethanol have been used to form nanoparticle colloids. Limited information on toluene, acetone, hexane, and decane is also available. These initially colorless liquids can become increasingly yellow as the volume of aerosol processed increases, indicating a rising concentration of nanoparticles in the liquid. The strong color may, however, indicate that particles larger than ~20 nm and agglomerates of particles are more prevalent in solution than in the dry deposited samples. Typically, bubbled colloids are collected for several hours (~ 4 to 8 hours) in ~ 200 mL solvent for unclassified samples and ~25 mL for classified samples. For more volatile solvents, such as ethanol, the solvent must be continually replenished to compensate for losses due to evaporation, or the solvent must be cooled (in ~ 0°C ice bath) to reduce the solvent evaporation rate. Water and ethylene glycol are sufficiently nonvolatile that replenishing or cooling the solvent is unnecessary. Unclassified aerosols contain more particles (because losses of uncharged and incorrectly sized particles does not occur prior to collection) and form highly concentrated colloid solutions very rapidly

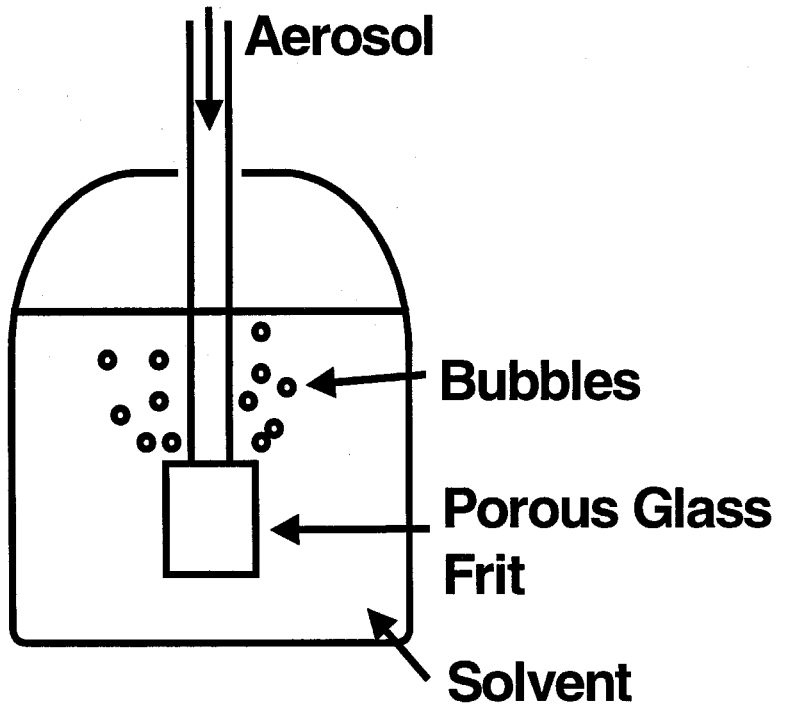

Figure 4.2: Schematic of the collection vessel used to produce bubbled colloids.

in ~200 mL solvent for ~4 hours collection time. Classified samples are usually collected for > ~ 8 hours in much less solvent volume (~ 25mL) to produce concentrated classified colloids.

4.6.2 Condensation Colloids

Aerosol nanoparticles have also been collected in colloids using a method referred to as condensation colloid collection. We have developed this method to improve the collection efficiency of nanoparticles to produce highly concentrated nanoparticle colloids (~ 20% by volume) in a minimal amount of time. In order to form condensation colloids, solvent vapor must first be introduced into the aerosol stream. To condense the solvent onto the aerosol particles, the solvent vapor and aerosol flow into a cooled condenser. Collection occurs at the bottom of the condenser as dropwise collection into vials. A schematic of the condensation collection apparatus is shown in Fig. 4.3. The aerosol flow is saturated with solvent vapor by passage over solvent in a constant-temperature flask maintained at 55°C for water, 37°C for ethanol, and 140°C for ethylene glycol. The aerosol and solvent vapor pass into a condenser cooled to ~ 0°C where the solvent condenses onto the nanoparticles, causing them to grow and deposit onto the cold condenser walls. The condensate drains into a vial at a rate of approximately one drop every 2 minutes. Collection times vary depending upon the final colloid volume required.

4.7 Particle Characterization

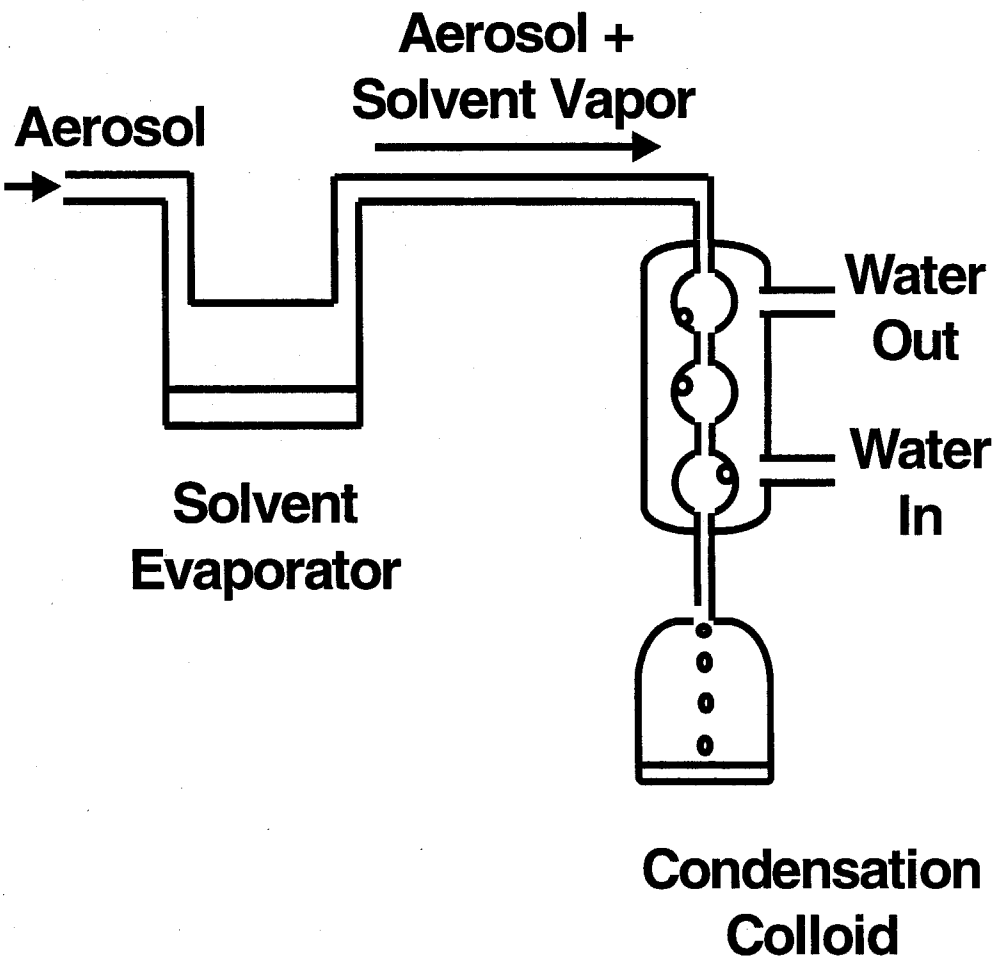

Figure 4.3: Schematic of the collection vessel used to produce condensation colloids.

4.7.1 RDMA Size Distributions

The particle size distribution of the aerosol nanoparticles is determined by scanning RDMA voltages between 10 and 3400 V, roughly corresponding to particle sizes between 3 and 50 nm for aerosol flow rates of 1.5 LPM and sheath gas flow rates of 15 LPM. The portion (~ 0.2 LPM) of classified aerosol is then inserted into an electrometer. The current carried by the classified particles is detected with this electrometer to determine the particle concentration corresponding to each size classified with the RDMA. Using the previously measured transmission efficiency of the RDMA and the known charging efficiency of the aerosol neutralizer, the particle size distribution can be inferred from these measurements [38],[39].

4.7.2 TEM

TEM analysis was performed with a Philips EM430 operating at 300keV to determine the particle morphology, including shape and crystallinity. The particle size distribution was also measured with the TEM to compare with the size distributions obtained from the RDMA. High resolution TEM was used to determine the particle crystalline core diameter and thickness of the amorphous oxide shell that formed in several experiments as described in the next section. Samples for TEM analysis were either collected with electrostatic precipitation directly onto holey carbon copper grids or by placing approximately 3 μL of liquid onto the grid. Ethanol was allowed to evaporate, leaving the colloid collected nanoparticles behind. Water and ethylene glycol were wicked off of the grid using filter paper, leaving behind colloidally collected particles for

analysis.

4.8 Experimental Results

4.8.1 Aerosol Nanoparticles Collected with Electrostatic Precipitation

Figure 4.4 shows a sample of particles classified at 13 nm nominal diameter with geometric standard deviation of $\sigma_g \sim 1.2$ collected on an amorphous holey carbon coated copper TEM grid with the corresponding diffraction pattern shown as an inset. The particles are nonagglomerated, spherical, single crystal nanoparticles with diameters between 11 and 14 nm. The aerosol RDMA measured size distribution shown in Fig. 4.5 shows that these classified nanoparticles have a mean diameter of 13 nm and a geometric standard deviation of $\sigma_g \sim 1.2$.

4.8.2 Aerosol Nanoparticles Collected in Colloids

4.8.2.1 Ethylene Glycol

Several groups have reported the collection of silicon nanoparticles in ethylene glycol in the 3 to 7 nm size range with a 1 nm oxide shell that have been processed by silane pyrolysis and subsequent thermal or wet chemical oxidation [33],[34]. Our results suggest that ethylene glycol may not be as inert as previously suggested and that the particles may be modified substantially after collection in this liquid. Fig. 4.6 shows a

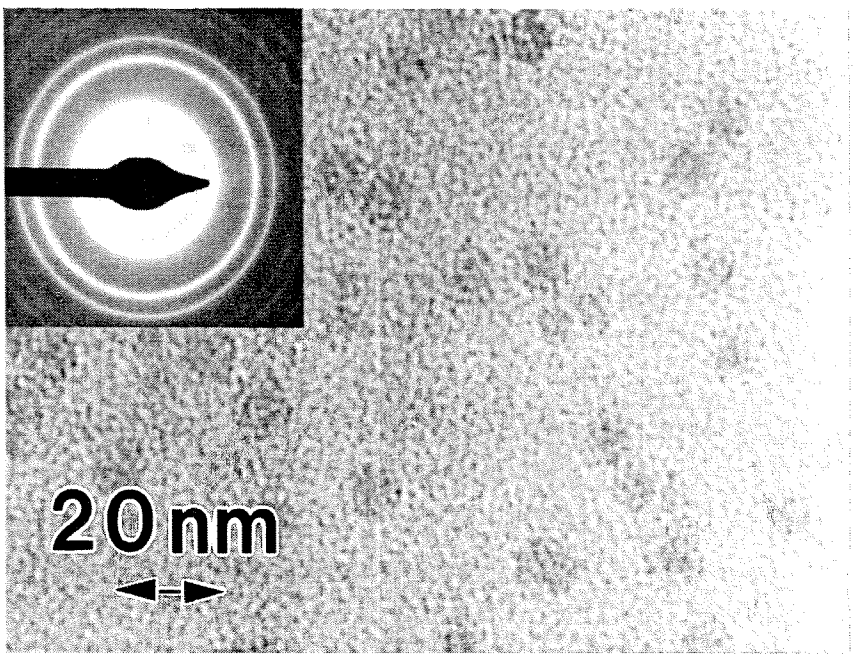

Figure 4.4: 13 nm classified aerosol nanoparticles collected with electrostatic precipitation.

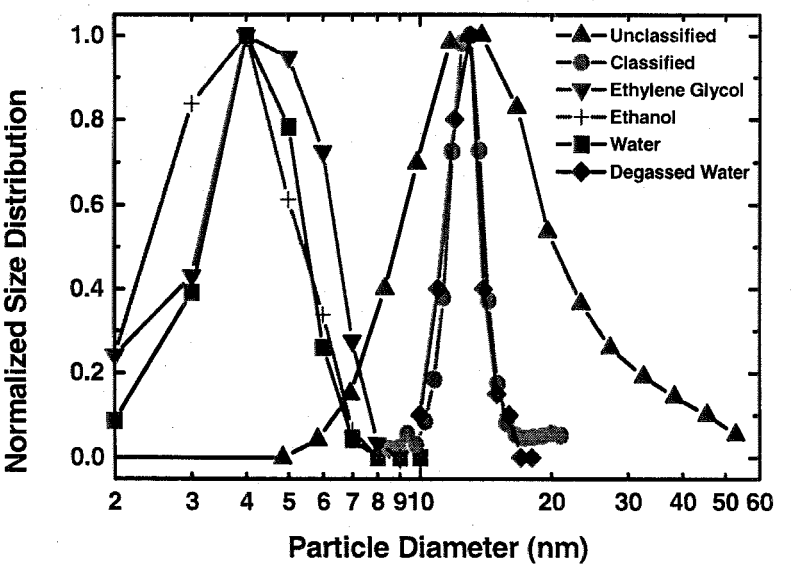

Figure 4.5: Size distributions of aerosol silicon nanoparticles prior to and following collection in various solvents. Aerosol samples were measured with an RDMA and colloid samples were determined from TEM images.

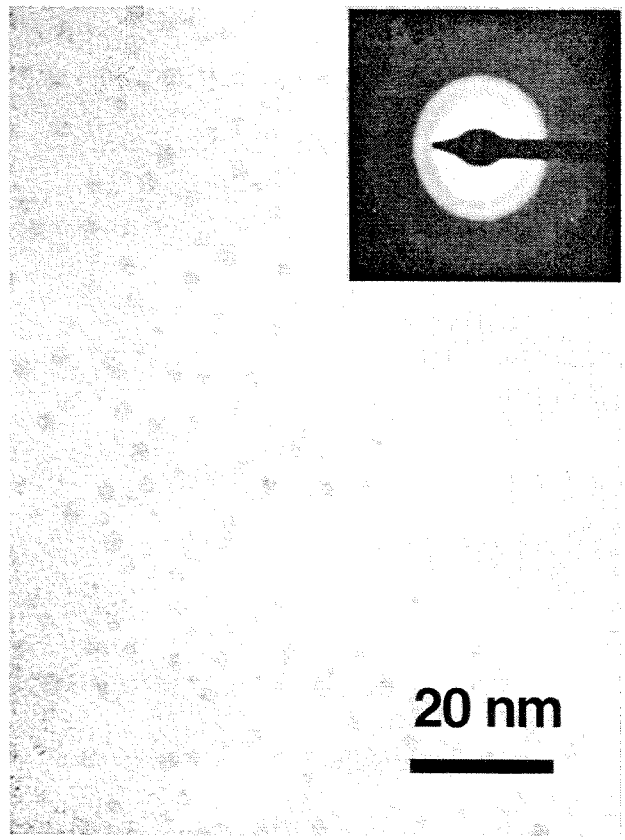

Figure 4.6: Aerosol particles following colloidal collection in ethylene glycol.

sample of monodisperse silicon nanoparticles that was collected in ethylene glycol. The particles in this sample have an average diameter of 4.2 nm and a σ_g ~ 1.4. However, the measured size distribution of unclassified aerosol nanoparticles prior to ethylene glycol collection shown in Fig. 4.5 has a mean diameter of 11 nm and σ_g = 1.5. Few particles are 3 to 5 nm in size. In this sample, high resolution TEM also shows oxide shells of approximately 1 nm on these ethylene glycol collected nanoparticles, even though these nanoparticles were never exposed to oxygen prior to ethylene glycol collection.

High resolution TEM (Fig. 4.7) also shows pronounced facets on the crystalline core of the nanoparticle instead of the nearly spherical cores seen in the electrostatic precipitation samples. This suggests a different mechanism of oxide formation that illustrates differences in reactivity of different crystalline faces to oxidation, a point considered by many researchers [40],[41],[42]. In this colloid, reactions with ethylene glycol and dissolved oxygen in the ethylene glycol are quite possibly responsible for the oxidation of the silicon nanoparticle. These outer silica surfaces then react with ethylene glycol, etching the nanoparticles to produce smaller diameter particles. In dissolution studies of silicon surfaces with ethylene glycol, Blohowiak and coworkers found that planar silica surface reacts with ethylene glycol to form an alkoxy-modified surface. In their attempt to recover the reaction product, a small amount of a clear, cross-linked polymer was found and they tentatively identified it as $Si(OCH_2CH_2O)_x$ [12]. A reaction between the ethylene glycol and silicon nanoparticles has some major advantages; the nanoparticles are sterically stabilized by the ethylene glycol to form a stable colloid and they become more monodisperse (from σ_g ~ 1.5 to σ_g ~ 1.4) in the colloid compared with

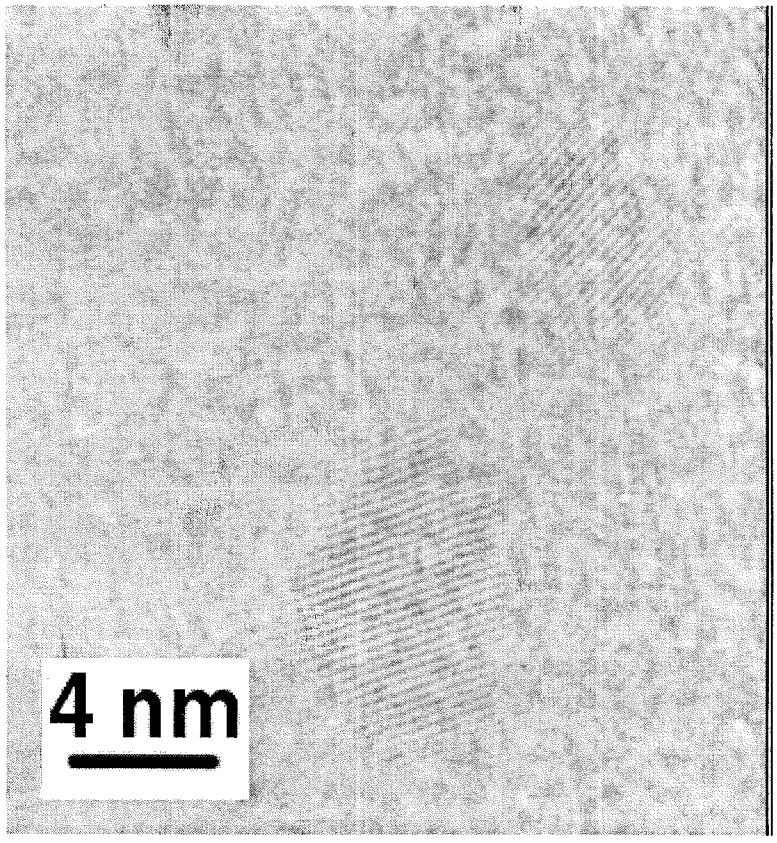

Figure 4.7: High resolution TEM of faceted crystalline cores following colloidal collection in ethylene glycol.

the original aerosol.

4.8.2.2 Ethanol

Silicon nanoparticles collected in ethanol show the same trends as seen in the ethylene glycol colloid. Monodisperse particles of 2 to 5 nm result from the collection of an unclassified aerosol sample having an RDMA-determined size distribution similar to that of Fig. 4.5. The ethanol colloid particles have an average diameter of 3.5 nm and σ_g ~ 1.4, but the original aerosol mean diameter was 14 nm and $\sigma_g = 1.9$. Even when aerosol particles are classified at 15 nm prior to collection, monodisperse particles with diameters of 2 to 5 nm are formed in the colloid, as shown in Fig. 4.8. It has been reported that ethanol dissociatively adsorbs on silicon at room temperature to form hydrogen and ethoxy groups bound on the surface [43]. These ethoxy groups could be responsible for sterically stabilizing the nanoparticles to produce the observed stable ethanol colloid.

4.8.2.3 Stöber Synthesis with Silicon Nanoparticle Ethanol Colloids

Reactions of silica in ethanol are well known. The Stöber process is a method used to produce monodisperse silica spheres from tetraethoxysilane (TEOS) in a basic ethanol solution [15]. Ordered microporous structures called zeolites are also produced from solution-phase reactions of TEOS, although solid sources of silica are also used. Both synthesis routes begin with the formation of a gel with a nanometer-scale structure. The disordered network later organizes into the uniform silica spheres or into the zeolite crystalline structure [16]. The reaction conditions of the present nanoparticle colloid

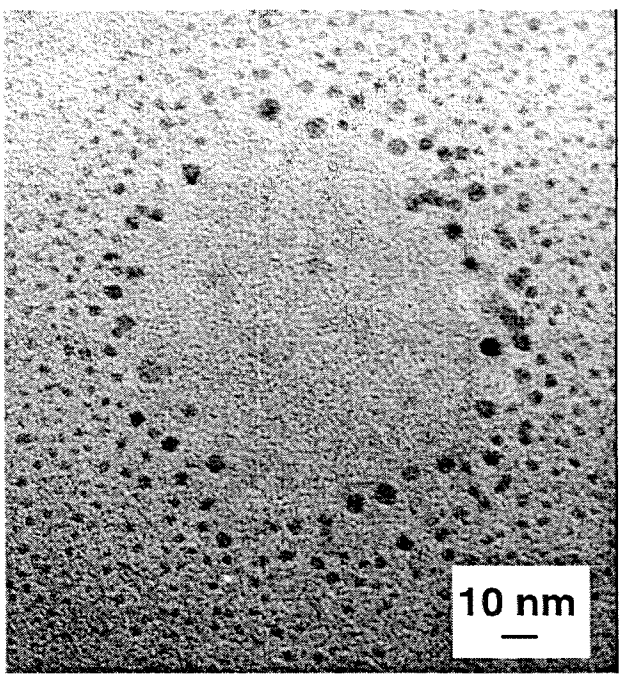

Figure 4.8: Aerosol nanoparticles following colloidal collection in ethanol.

studies do not allow the disordered network to become organized.

In the ethanol colloid, a possible reaction product between ethanol and silicon nanoparticles may resemble a TEOS-like species. Goodwin and Kenney have demonstrated that silicon dioxide can be used as a starting point to produce alkoxysilanes via esterification reactions in basic solutions [44],[45]. Blohowiak and coworkers acknowledge that this esterification reaction can occur even in the absence of the base [12], as when the ethanol colloid was made with the silicon nanoparticles. To examine this possibility of forming a tetraalkoxysilane species directly in the ethanol colloid, a small amount of the silicon nanoparticle ethanol colloid was used in place of pure ethanol in the Stöber reaction. The reaction mixtures are described in Table 4.1. The classified sample contains 15 nm particles collected in ethanol, and the unclassified sample contains particles with an average diameter of 11 nm. After 24 hours, TEM samples were prepared from these solutions.

Comparing Fig. 4.9a with Fig. 4.9b and 4.9c, it is apparent that amorphous silica is present in all three, indicating that the ethanol and silicon nanoparticle colloid already contains a TEOS-like reactant, either free in solution or bound to the surface of the nanoparticle. Indeed, Crowell and coworkers contends that the chemistry of TEOS can be modeled by ethanol adsorption on SiO_2 surfaces [46]. Figure 4.9a illustrates the formation of approximately 25 nm silica particles which are slightly agglomerated with small necks. Figure 4.9b shows a similar silica particle network of ~15 nm particles incorporating ~ 3 nm silicon nanoparticles. Since no TEOS was added to the reaction mixture, a TEOS-like material must already be present in the ethanol colloid in order to produce the silica

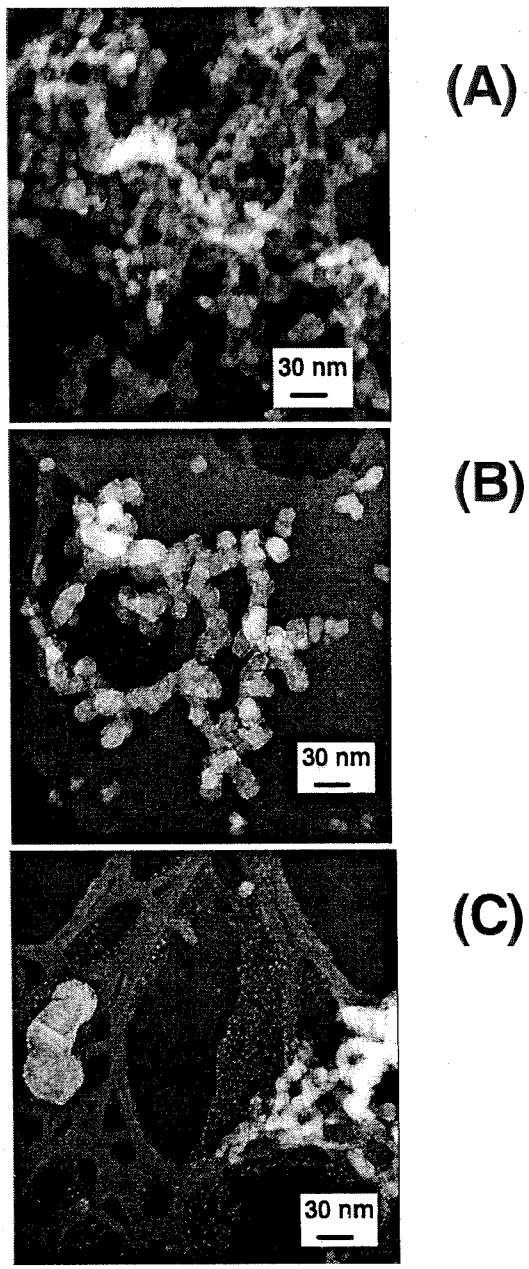

Figure 4.9: Stöber reaction **(A)** with TEOS added, **(B)** with no TEOS added, but with ethanol and classified silicon nanoparticle colloid, and **(C)** with no TEOS added, but with ethanol and unclassified silicon nanoparticle colloid.

	Figure 4.9a	Figure 4.9b	Figure 4.9c
EtOH	15.42 M	15.30 M	15.30 M
EtOH + Si	0M	0.12 M	0.12 M
[NH4OH]	0.59 M	0.59 M	0.59 M
[H2O]	2.48 M	2.48 M	2.48 M
[TEOS]	0.017mM	0 M	0 M

Table 4.1: Reaction composition of images shown in Fig. 4.9.

network. The necking is more pronounced in Fig. 4.9b and the silica spheres are smaller, indicating that less TEOS-like material is available to react. When unclassified nanoparticles are collected in ethanol (Fig. 4.9c), they also produce silica. Dark field TEM verifies that nanoparticle cores remain crystalline even after the reaction is complete.

4.8.2.4 Water

Since high temperature steam is often used in wet chemical oxidation of silicon, it is not surprising that oxidation occurs when silicon and water come into contact. A uniform oxide shell forms on the silicon particles but does not completely consume the crystalline core. As with the ethylene glycol and ethanol samples, an initially unclassified sample of silicon nanoparticles becomes relatively monodisperse when suspended in water (Fig. 4.10a). The final particle diameters are 2 to 5 nm and the geometrical standard deviation is $\sigma_g = 1.3$. These particles remained unchanged even after a year of storage in water. It is believed that stresses in the oxide layer prevent the diffusion of oxygen into the unreacted silicon core and that the volume increase when silicon reacts to form silicon dioxide prevents the complete consumption of the silicon nanoparticle [47]. The dark field image in Fig. 4.10b confirms that particle cores are still crystalline after a year of storage in water.

Figure 4.11 shows silicon nanoparticles encased in a gel-like amorphous material that forms as a reaction product between water and silicon. This amorphous material solidifies when the water evaporates from the grid during sample preparation. With

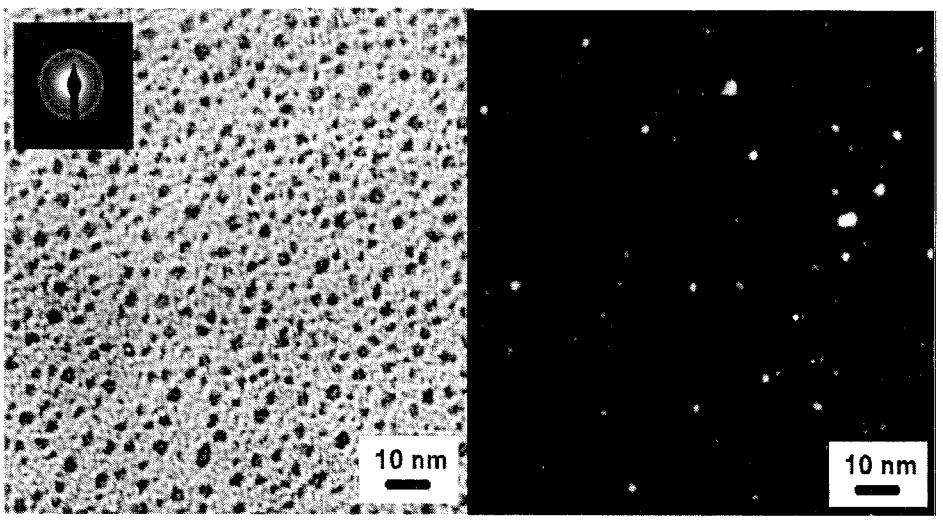

Figure 4.10: Aerosol nanoparticles following collection in water. These images were taken one year after the water colloid was produced and have remained unchanged during that year.

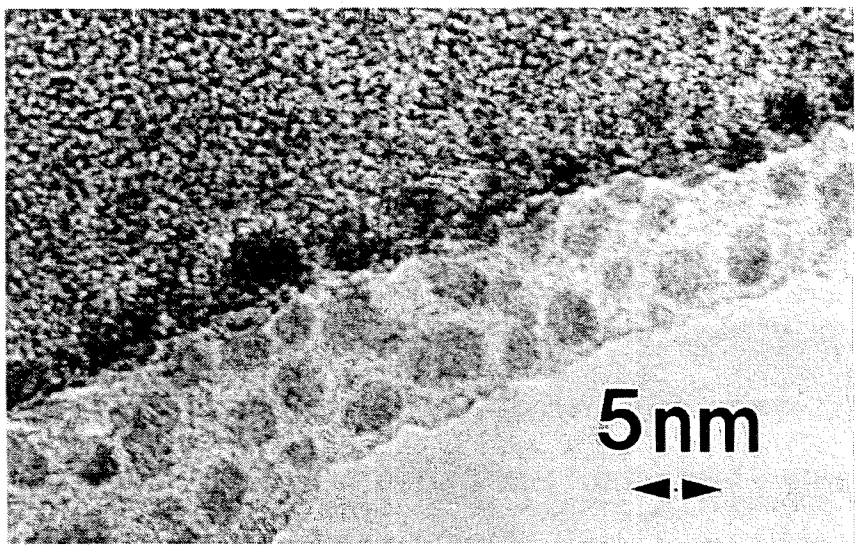

Figure 4.11: 13 nm classified aerosol nanoparticles following water collection. The amorphous material is able to support particles beyond the edge of the amorphous holey carbon grid coating.

greater nanoparticle concentrations, the water colloid begins to develop into a cloudy solution. Under TEM, this cloudy suspension is seen to form vast networks of amorphous material with incorporated crystalline nanoparticles. This sol-gel like structure in the colloid may be responsible for colloidal stability, although it also raises contamination concerns about using this colloid to prepare device structures.

4.8.2.5 Degassed Water

It has been reported that dissolved oxygen in solvents is able to initiate the formation of etch sites in otherwise ideal Si and H-Si surfaces[48] and oxygen has been suggested as a reactant in etching and oxidation studies of silicon surfaces [49],[50],[51],[52],[53]. In order to test the hypothesis that dissolved oxygen plays a key role in the reactivity of the silicon nanoparticles to the solvent, we attempted to remove the oxygen in water prior to collecting a nanoparticle sample. The first degassing process was attempted by bubbling UHP N_2 through 200mL of 18MΩ water in a sealed glass container for one hour. The same glass container was then used as the collection vessel for the bubbled colloid by bubbling the silicon nanoparticle aerosol stream and for the condensation colloid by evaporating the degassed 18MΩ water into the aerosol stream followed by condensation. Because the silicon nanoparticle aerosol is formed in UHP N_2, no oxygen was added to the degassed water even during bubbled colloid collection. TEM samples of this solution were made and gel-like material was still clearly observed for both methods. Particle diameter reductions were still apparent and the extent of the size reduction seemed consistent with the size reduction observed with solvent that was not

degassed. Clearly, degassing water by simply bubbling UHP N_2 through water did not reduce the dissolved oxygen concentration to sufficiently low levels to prevent reactions between the solvent and silicon nanoparticles.

4.8.2.6 Aggressively Degassed Solvents

Since the initial degassing procedure failed to reduce the dissolved oxygen concentration sufficiently, a more aggressive degassing procedure was followed. To reduce the concentration of dissolved oxygen to as low a level as possible, a round bottom flask was evacuated with a vacuum pump to ~ 10's mTorr. Two liters of solvent (i.e.,18MΩ water, ethanol, and ethylene glycol) were introduced into the flask. A ~ 2 LPM flow of UHP He was introduced into the flask while the vacuum pump was running. Initially, small bubbles could be seen coming from the solvent. After 10 minutes, these bubbles were no longer observed. The degassing process continued for 40 minutes under these conditions, after which the solvent was carefully transferred from the evacuated flask and into a sealed 3-neck round bottom flask to prevent oxygen contact. The solvent was used immediately in condensation colloid collection. No attempts were made to produce a bubbled colloid with these degassed solvents because the condensation colloid collection proved to be an excellent technique to produce very concentrated silicon nanoparticle colloids. Attempts to measure the dissolved oxygen concentration showed that the level was below the detection limit of the oxygen detector, meaning that the levels were below < 3 ppt.

To collect aerosol silicon nanoparticles efficiently and to produce highly

concentrated suspensions, we employ the condensation colloid collection method described earlier. The solvents used in these experiments are the aggressively degassed solvents prepared according to the description provided above and the silicon nanoparticles are 13 nm classified particles. Because solvent in the collection vial is not *being evaporated (as is the case in bubbled colloid collection), solvent does not need to be* replaced in the collection container, even for volatile solvents, such as ethanol. As a colloid drop was being formed, 5 μL was collected on a TEM grid and immediately analyzed. As seen in Fig. 4.12, extremely high concentrations of ~ 13 nm classified nanoparticles collected in degassed water are observed. These nanoparticles have not undergone serious decreases in their particle diameters, their cores are very spherical, and no amorphous gel-like material is observed in this sample, even though the nanoparticle concentration is extremely high. These nanoparticles have an average core dimension of 12.7 nm and σ_g ~ 1.1 as measured both from dark field and from high resolution TEM.

4.9 Summary of Solvents

One of the reasons that we have been able to detect this silicon nanoparticle etching that occurs in solvents is because we are able to measure the aerosol nanoparticle size distribution before (and during) colloid collection. This data can then be compared to the size distributions determined from TEM, including samples prepared both with electrostatic precipitation and colloid collection. Table 4.2 details the results from both

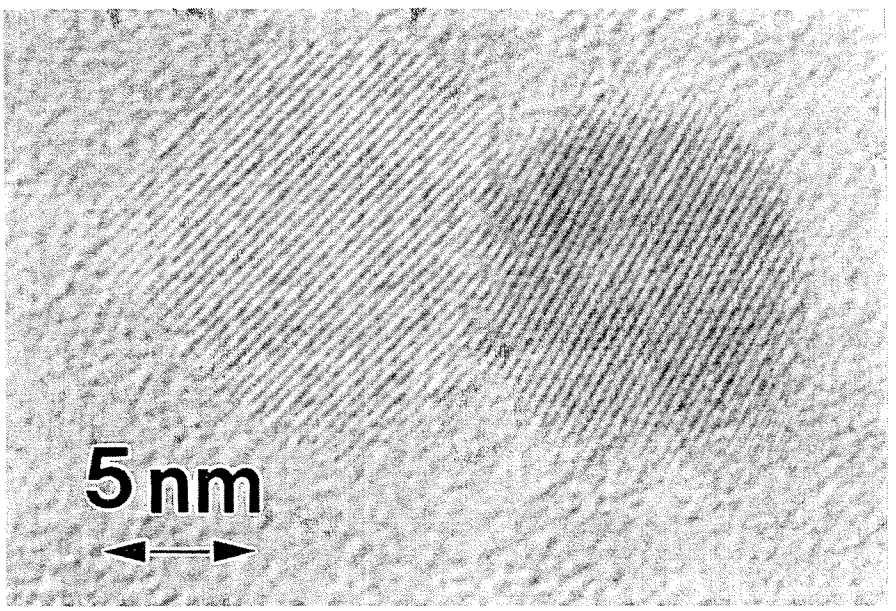

Figure 4.12: High resolution of 13 nm classified aerosol nanoparticles collected with colloidal collection into aggressively degassed water.

	RDMA		TEM	
	<Dp> (nm)	σg	<Dp> (nm)	σg
Ethylene Glycol	14	1.9	4.2	1.4
Ethanol	14	1.9	3.5	1.4
Water	13	1.2	3.8	1.3
Aggressively Degassed Water	13	1.2	12.7	1.1

Table 4.2: RDMA and TEM measured size distributions. Aerosol nanoparticle size distributions were measured with an RDMA and colloidal nanoparticle size distributions were measured with TEM.

the RDMA and TEM measured size distributions for all solvents.

4.10 Summary

The results from these experiments indicate that silicon nanoparticle colloids may not be completely inert. Indeed, reactions with untreated solvents may etch particles, resulting in a lower than expected particle diameter for particles collected in colloids. The diameter is significantly smaller than those measured in the aerosol phase and those observed in dry deposition techniques, such as electrostatic precipitation. Collection of large silicon nanoparticles in reactive, untreated solvents may not be possible due to this dramatic diameter reduction. However, colloidal reactivity may provide a way to produce monodisperse silicon nanoparticles in the 2 to 5 nm size range from a polydisperse source material. Furthermore, particles suspended in these colloids are stable, possibly indicating a steric stabilization from the solvent or from gel-like formation from solvent/particle reactions. This stabilization is useful in that it prevents particle agglomeration once the solvent is evaporated from the particles. These colloidal particles are surface passivated, either through solvent or dissolved oxygen reactions. The oxide passivation layer may not be the high quality oxide layer that is needed to insure semiconductor device performance, so additional processing steps may be required to produce a high quality oxide layer. Furthermore, the presence of gel-like amorphous material that remains once the solvent has evaporated remains a serious contamination problem. Additional processing may be required to remove solvent molecules and hydrocarbons from the

surface of these silicon nanoparticles. The gel-like material that forms in these colloids could present serious contamination problems in use of these colloid solutions in semiconductor device fabrication.

Fortunately, particle etching can be reduced or prevented by using aggressively degassed solvents where oxygen levels are below ~ 3 ppt. Since no amorphous material has been seen in these materials, the contamination issue is mitigated although not completely eliminated. More work is required in this area, especially if close-packed arrays of these silicon nanoparticles are required for device layers. Not only will these applications require the formation of stable colloids, but they will also require that the stabilizing entity be free of contamination or easily (and completely) removed before device processing.

Bibliography

[1] J.M. Lauerhaas, G.M. Credo, J.L. Heinrich, and M.J. Sailor, "Reversible Luminescence Quenching of Porous Si by Solvents," *J. Am. Chem. Soc.*, **114**, pp. 1911-1912 (1992).

[2] J.K.M. Chun, A.B. Bocarsly, T.R. Cottrell, J.B. Benziger, and J.C. Lee, "Proton Gated Emission from Porous Silicon," *J. Am. Chem. Soc.*, **115**, pp. 3024-3025 (1993).

[3] B. Sweryda-Krawiec, R.R. Chandler-Henderson, J.L. Coffer, Y.G. Rho, R.F. Pinizzotto, "A Comparison of Porous Silicon and Silicon Nanocrystallite Photoluminescnece Quenching with Amines," *J. Phys. Chem.*, **100**, pp. 13776-13780 (1996).

[4] K.D. Keefer, *Mater. Res. Soc. Symp. Proc.* **32**, p. 15 (1984).

[5] M.R. Linford, P. Fenter, P.M. Eisenberger, and C.E.D. Chidsey, "Alkyl Monolayers on Silicon Prepared from 1-Alkenes and Hydrogen-Terminated Silicon," *J. Am. Chem. Soc.*, **117**, pp. 3145-3155 (1995).

[6] J. Duchet, B. Chabert, J.P. Chapel, J.F. Gerard, J.M. Chovelon, and N. Jaffrezic-Renault, "Influence of the Deposition Process on the Structure of Grafted Alkylsilane Layers," *Langmuir*, **13**, pp. 2271-2278 (1997).

[7] J. Terry, R. Mo, C. Wigren, R. Cao, G. Mount, P. Pianetta, M.R. Linford, and C.E.D. Chidsey, "Reactivity of the H-Si(111) Surface," *Nucl. Instr. And Meth. In Phys. Res. B*, **113**, pp. 94-101 (1997).

[8] G.S. Higashi, Y.J. Chabal, G.W. Trucks, and K. Raghuachari, "Ideal Hydrogen Termination of the Si-(111) Surface," *Appl. Phys. Lett.*, **56**, pp. 656-658 (1990).

[9] J.B. Brzoska, N. Shahidzadeh, and F. Rondelez, "Evidence of a Transition Temperature for the Optimum Deposition of Grafted Monolayer Coatings," *Nature*, **360**, pp. 719-721 (1992).

[10] W.C. Bigelow, D.J. Pickett, and W.A. Zisman, *J. Colloid Sci.*, **1**, pp. 513 (1946).

[11] E.P. Plueddeman, *Silane Coupling Agents*, New York, Plenum (1982).

[12] K.Y. Blohowiak, D.R. Treadwell, B.L. Mueller, M.L. Hoppe, S. Jouppi, P. Pansal, K.W. Chew, C.L.S. Scotto, F. Babonneau, J. Kampf, and R.M. Laine, "SiO_2 as a Starting Material for the Synthesis of Pentacoordinate Silicon Complexes," *Chem. Mater.*, **6**, pp. 2177-2192 (1994).

[13] B. Sweryda-Krawiec, T. Cassagneau, and J.H. Fendler, "Surface Modification of Silicon Nanocrystallites by Alcohols," *J. Phys. Chem. B.*, **103**, 9524-9529 (1999).

[14] N.Y. Kim and P.E. Laibinis, "Thermal Derivatization of Porous Silicon with Alcohols," *J. Am. Chem. Soc.* **119**, pp. 2297-2298 (1997).

[15] W. Stöber, A. Fink, and E. Bohn, "Controlled Growth of Monodisperse Silica Spheres in the Micron Size Range," *J. Coll. Inter. Sci.*, **26**, pp. 62-69 (1968).

[16] A. Tuel, "Layered Intermediates in Zeolite Synthesis: Are Structures Related?" *Chem. Mater*, **11**, pp. 1865-1875 (1999).

[17] C.B. Murray, D.J. Norris, and M.G. Bawendi, "Synthesis and Characterization of Nearly Monodisperse CdE (E = S, Se, Te) Semiconductor Nanocrystallites," *J. Am. Chem. Soc.*, **115**, pp. 8706-8715 (1993).

[18] M. Brust, M. Walker, D. Bethell, D.J. Schiffrin, and R. Whyman, "Synthesis of

Thio-Derivatized Gold Nanoparticles in a 2-Phase Liquid-Liquid System," *J. Chem. Soc. Chem. Comm.*, **7**, pp. 801-802 (1994).

[19] D.V. Leff, P.C. O'Hara, J.R. Heath, and W.M. Gelbart, "Thermodynamic Control of Gold Nanocrstal Size - Experiment and Theory," *J. Phys. Chem.*, **99**, pp. 7036-7041 (1995).

[20] R.P. Andres, J.D. Bielefeld, J.I. Henderson, D.B. Janes, V.R. Kolagunta, C.P. Kubiak, W.J. Mahoney, and R.G. Osifchin, "Self-Assembly of a Two-Dimensional Superlattice of Molecularly Linked Metal Clusters," *Science*, **273**, pp. 1690-1693 (1996).

[21] N. Herron, J.C. Calabrese, W.E. Farneth, and Y. Wang, "Crystal-Structure and Optical-Properties of $Cd_{32}S_{14}(SC_6H_5)_{36}.DMF_4$, A Cluster with a 15-Angstrom CdS Core," *Science*, **259**, pp. 1426-1428 (1993).

[22] B.O. Daboussi, C.B. Murray, M.F. Rubner, and M.G. Bawendi, "Langmuir-Blodgett Manipulation of Size-Selected CdSe Nanocrystallites," *Chem. Mater.*, **6**, pp. 216-219 (1994).

[23] M. Bohmer, "In Situ Observation of 2-Dimensional Clustering during Electrophoretic Deposition," *Langmuir*, **12**, pp. 5747-5750 (1996).

[24] H.M. Chan, "Layered Ceramics: Processing and Mechanical Behavior," *Annual Review of Materials Science*, **27**, pp. 249-282 (1997).

[25] Y. Solomentsev, M. Bohmer, and J.L. Anderson, "Particle Clustering and Pattern Formation During Electrophoretic Deposition: A Hydrodynamic Model," *Langmuir*, **13**, pp. 6058-6068 (1997).

[26] P. Sarkar and P.S. Nicholson, "Structural Ceramic Microlaminates by Electrophoretic Deposition," *J. Am. Chem. Soc.*, **75**, pp. 2907-2909 (1992).

[27] P.S. Nicholson, P. Sarkar, and X. Huang, "Electrophoretic Deposition and its Use to Synthesize ZrO_2/Al_2O_3 Micro-Laminate Ceramic-Ceramic Composites," *J. Mater. Sci.*, **28**, pp. 6274-6278 (1993).

[28] M. Giersig and P. Mulvaney, "Formation of Ordered Two-Dimensional Gold Colloid Lattices by Electrophoretic Deposition," *J. Phys.Chem*, **97**, pp. 6334-6336 (1993).

[29] M. Giersig and P. Mulvaney, "Preparation of Ordered Colloid Monolayers by Electrophoretic Deposition," *Langmuir*, **9**, pp. 3408-3413 (1993).

[30] L.T. Canham, "Silicon Quantum Wire Array Fabrication by Electrochemical and Chemical Dissolution of Wafers," *Appl. Phys. Lett.*, **57**, pp. 1046-1048 (1990).

[31] V. Lehmann and U. Gösele, "Porous Silicon Formation: A Quantum Wire Effect," *Appl. Phys. Lett.*, **58**, pp. 856-858 (1991).

[32] J.D. Holmes, K.P. Johnston, R.C. Doty, and B.A. Korgel, "Control of Thickness and Orientation of Solution-Grown Silicon Nanowires," *Science*, **287**, pp. 1471-1473 (2000).

[33] K.A. Littau, P.J. Szajowski, A.J. Muller, A.R. Kortan, and L.E. Brus, "A Luminescence Silicon Nanocrystal Colloid via a High-Temperature Aerosol Reaction," *J. Phys. Chem.*, **97**, pp. 1224-1230 (1993).

[34] W.L. Wilson, P.F. Szajowski, and L.E. Brus, "Quantum Confinement in Size-Selected Surface-Oxidized Silicon Nanocrystals," *Science*, **262**, pp. 1242-1244

(1993).

[35] J.J. Wu, H.V. Nguyen, and R.C. Flagan, "A Method for the Synthesis of Submicron Particles," *Langmuir*, **3**, pp. 266-271 (1987).

[36] R.P. Camata, H.A. Atwater, K.J. Vahala, and R.C. Flagan, "Size Classification of Silicon Nanocrystals," *Appl. Phys. Lett.*, **68**, pp. 3162-3164 (1996).

[37] R.P. Camata, "Aerosol Synthesis and Characterization of Silicon Nanocrystals," Caltech Thesis (1997).

[38] S.H. Zhang, Y. Akutsu, L.M. Russell, R.C. Flagan, and J.H. Seinfeld, "Radial Differential Mobility Analyzer," *Aerosol Sci. Technol.*, **23**, pp. 357-372 (1995).

[39] S.H. Zhang and R.C. Flagan, "Resolution of the Radial Differential Mobility Analyzer for Ultrafine Particles," *J. Aerosol Sci.* **27**, pp. 1179-1200 (1996).

[40] E.A. Irene, H.Z. Massoud, and E. Tierney, "Silicon Oxidation Studies - Silicon Orientation Effects on Thermal Oxidation," *J. Electrochem. Soc.*, **133**, pp. 1253-1256 (1986).

[41] H.Z. Massoud, J.D. Plummer, and E.A. Irene, "Thermal-Oxidation of Silicon in Dry Oxygen - Accurate Determination of the Kinetic Rate Constants," *J. Electrochem. Soc.*, **132**, pp. 1745-1753 (1985).

[42] T. Hirata, "Orientation Dependence of Infrared Spectra on Thermal Oxidation and Subsequent Etching of Single Crystal Si," *Solid State Comm.*, **111**, pp. 421-426 (1999).

[43] J. Eng, K. Raghavachari, L.M. Struck, Y.J. Chabal, B.E. Bent, G.W. Glynn, S.B. Christman, E.E. Chaban, G.P. Williams, K. Radermacher, and S. Manti, "A Vibrational Study of Ethanol Adsorption on Si(100)," *J. Chem. Phys.*, **106**, pp.

9889-9898 (1997).

[44] G.B. Goodwin and M.E. Kenney, "A New Approach to the Synthesis of Alkyl Silicates and Organosiloxanes," *ACS Symp. Ser.*, **360**, pp. 238-248 (1988).

[45] G.B. Goodwin and M.E. Kenney, "A New Route to Alkoxysilanes and Alkoxysiloxanes of Use for the Preparation of Ceramics by the Sol-Gel Technique," *Inorg. Chem.*, **29**, pp. 1216-1220 (1990).

[46] J.E. Crowell, L.L. Tedder, H.C. Cho, F.M. Cascarano, and M.A. Logan, "Model Studies of Dielectric Thin-Film Growth - Chemical Vapor Deposition of SiO_2," *J. Vac. Soc. & Tech. A.*, **8**, pp. 1864-1870 (1990).

[47] D.B. Kao, J.P. McVittie, W.D. Nix, and K.C. Saraswat, "Two-Dimensional Thermal Oxidation of Silicon - II. Modeling Stress Effects in Wet Oxides," *IEEE Trans. Electr. Dev.*, ED-35, pp. 25 - 37 (1988).

[48] C.P. Wade and C.E.D. Chidsey, "Etch-Pit Initiation by Dissolved Oxygen on Terraces of H-Si(111)," *Appl. Phys. Lett.*, **71**, pp. 1679-1681 (1997).

[49] S.A. Campbell, K. Cooper, L. Dixon, R. Earwaker, S.N. Port, and D.J. Schiffrin, "Inhibition of Pyramid Formation in the Etching of Si P[100] in Aqueous Potassium Hydroxide-Isopropanol," *J. Micromech. Microeng*, **5**, pp. 209-218 (1995).

[50] M.L.W. van der Zwan, J.A. Bardwell, G.I. Sproule and M.J. Graham."Mechanism of the Growth of Native-Oxide on Hydrogen Passivated Silicon Surfaces," *Appl. Phys. Lett.*, **64**, pp. 446-447 (1994).

[51] S. Watanabe and Y. Sugita, "The Role of Dissolved-Oxygen in Hot-Water During Dissolving Oxides and Terminating Silicon Surfaces with Hydrogen," *Surf. Sci.*

327, pp. 1-8 (1995).

[52] G.S. Higashi, Y.J. Chabal, K. Raghavachari, R.S. Becker, M.P. Green, K. Hanson, T. Boone, J.H. Eisenberg, S.F. Shive, G.N. DiBello, and K. L. Fulford, *Proc. Electrochem. Soc.*, *93-13*, pp. 1989 (1993).

[53] S.L. Yau, F.-R.F. Fan, and A.J. Bard, "In Situ Imaging of Silicon(111) in HF Under Potential Control," *J. Electrochem. Soc.*, **139**, pp. 2825-2829 (1992).

Chapter 5: Oxide-Passivation of Silicon Nanoparticles

5.1 Introduction

As previously mentioned, silicon nanoparticle-based floating gate metal-oxide-semiconductor field effect devices are attractive candidates for terabit cm^{-2} density nonvolatile memory applications. However, variability in the size, location, and interface electronic quality of the nanoparticles in an ensemble limits memory speed and retention time. Furthermore, in a discontinuous nanoparticle layer, nanoparticles must be electrically isolated from each other, presumably with a high quality oxide. To address these issues and to reduce performance variability, we have designed a two-stage aerosol process reactor to integrate deposited oxide-passivated aerosol silicon nanoparticles into floating gate devices.

As discussed in Chapter 3, the first stage is used to synthesize silicon nanoparticles by thermal decomposition of silane gas in an aerosol reactor that has been optimized to produce spherical, single-crystal, nonagglomerated nanoparticles at sufficiently high rates for layer deposition. The nanoparticles are size-classified with a differential mobility analyzer to produce narrow size distributions (less than 10% at 5 nm diameter) in the aerosol nanoparticles. In the second stage, the monodisperse silicon particles are passivated with an oxide layer, either by thermal oxidation that partly consumes the particle or by aerosol vapor phase tetraethylorthosilicate (TEOS) deposition

as discussed in this chapter. Depending upon the process conditions, such as TEOS partial pressure, oxygen concentration, and reactor temperature, uniform oxide layers in the nanometer thickness range can be grown or deposited on the nanoparticles. At temperatures of 500-700°C, TEOS reacts on the nanoparticles, depositing a final uniform 1 nm oxide layer on the particle. At temperatures greater than 800°C, TEOS vapor undergoes homogeneous nucleation to form silica nanoparticles, producing large scale agglomerates of many tens to hundreds of nanometers with high fractal dimension.

Electronic measurements used to determine the insulating properties of the oxide passivation layer indicate that native oxide allows current flow between adjacent nanoparticles, whereas high temperature thermal oxide and deposited TEOS oxide produce oxide shells of sufficient quality and thickness to isolate electrically adjacent nanoparticles from each other. Photoluminescence (PL) measurements used to probe the Si/SiO_2 interface indicate the presence of a high quality interface between deposited TEOS oxide and silicon nanoparticles. The processes used to grow and deposit oxides and to probe oxide insulator qualities will be discussed in the following sections.

5.2 Discontinuous Nanoparticle Floating Gate Layer

As previously mentioned and to be discussed in greater detail in Chapters 6,7 and 8, nonvolatile floating gate memory devices have been previously fabricated by embedding silicon nanoparticles within the gate oxide of metal-oxide semiconductor field effect transistors by (i) implanting excess silicon into the gate oxide; and (ii) direct

deposition of nanometer-scale silicon islands in the floating gate region [1],[2],[3]. We propose to deposit aerosol-synthesized nanoparticles into the floating gate region of devices. In these floating gate devices, the insulation of the silicon nanoparticles is important, not only to insulate the nanoparticles from the conductive channel and gate, but to insulate individual nanoparticles from adjacent nanoparticles to prevent electron transfer within the floating gate layer. If the nanoparticles have a high quality oxide shell, then adjacent nanoparticles, even in contact, will remain electrically isolated from each other. Since these nanoparticle floating gate memories depend upon discrete charge storage, the prevention of lateral charge conduction throughout the nanoparticle layer is absolutely essential. In fabricating this floating gate layer, efforts need to be taken to insure the discreteness of the floating gate so that lateral carrier conduction does not occur.

As already mentioned, the performance of devices made of nanoparticle ensembles is potentially limited by a distribution in charge transit times of electrons from the channel to the nanoparticles, charging voltages, and threshold shifts caused by a broad distribution in nanoparticle size, position, oxide thickness, interface states, or shifts in energy of the electron levels due to quantum confinement effects [1],[2],[3]. Thus, fabricating nanoparticles in a way that is compatible with silicon ultra-large scale integration (ULSI) processing with controlled size distributions and oxide thicknesses that can be deposited on a substrate in a controlled manner with good control of electronic properties is vital to the development of reliable silicon nanoparticle-based nonvolatile floating gate memories.

As discussed in detail in Chapter 3, aerosol synthesis by silane efficiently generates silicon nanoparticles without surface organics. In one case, researchers at Bell Laboratories [4],[5] passivated the surface of silicon nanoparticles by passing the aerosol through a furnace along with oxygen to form a thermal oxide coating.

This chapter describes a method for the synthesis and oxide passivation of single crystal, spherical nonagglomerated silicon nanoparticles of controlled size. As discussed in Chapter 3, we pyrolyze dilute silane to nucleate and grow single crystal silicon nanoparticles. We then classify the nanoparticles with a RDMA to select particles within a narrow size interval and then passivate them with an oxide to achieve a very precise control over the critical dimensions in the final Si/SiO_2 heterostructure. The structure and morphology of these nanoparticles are investigated using TEM and tandem RDMA experiments with which particle size distribution can be monitored on-line. Current-voltage and PL measurements on deposited nanoparticles arrays are performed to probe passivation and interface quality of these nanoparticles. Control of the crystalline silicon core diameter, oxide thickness, and density facilitates the engineering control required for applications of silicon nanoparticles in nonvolatile memory devices.

5.3 Particle Oxidation

5.3.1 Thermal Oxidation

5.3.1.1 Native Oxides

In the first stage of the aerosol reactor (the pyrolysis and sintering furnace), the

oxygen level is kept below ~ 1 ppb with active oxygen scrubbers. Within the reactor and aerosol instruments, such as the neutralizer, RDMA, and collection chamber, the aerosol and gas can still be kept oxygen free. It is also possible to introduce oxygen into the system after particle formation is complete by adding in a separate oxygen flow or by using a gas containing oxygen as the RDMA sheath gas. Therefore, the aerosol system is capable of producing either bare unpassivated silicon or oxide passivated silicon nanoparticles, depending upon the requirements of the experiment. However, after removing an unpassivated silicon nanoparticle sample from the dry ultrahigh purity (UHP) nitrogen environment of the collection chamber, a native oxide shell rapidly forms on any exposed silicon surface, consuming the outer silicon material and converting it to SiO_x. With sufficient particle density, particles contact each other in random, three-dimensional deposits on substrates housed within the UHP collection environment. Even in low density deposits, contact with the substrate limits oxygen access to part of the particle surface. Once exposed to oxygen, native oxide passivates only that portion of the particle surface exposed to the ambient environment.

5.3.1.2 High Temperature Thermal Oxides

The two-stage aerosol reactor shown in Fig. 5.1 was developed to produce device-quality silicon dioxide passivated silicon nanoparticles. Silicon nanoparticles are formed and sintered in the first reactor stage. The second reactor is dedicated to the oxide passivation of these particles, either by thermal oxidation or by TEOS oxide deposition to produce stoichiometric SiO_2 shells. When thermal oxide passivating layers are required,

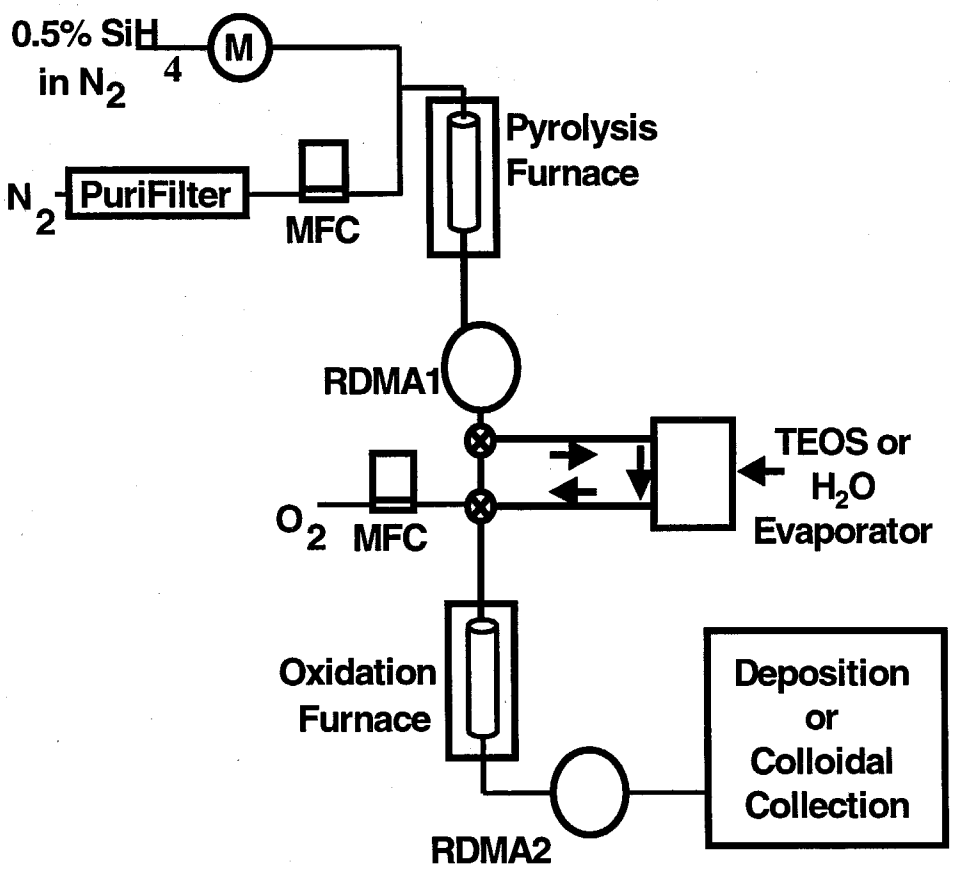

Figure 5.1: Two-stage aerosol reactor for the production of oxide-passivated silicon nanoparticles.

the silicon nanoparticle aerosol is either combined with a controlled flow rate of oxygen or oxygen is introduced into the system via the RDMA sheath gas. In general, oxygen concentrations of 20% oxygen in nitrogen are more than sufficient to produce the desired results. More importantly, low concentrations of oxygen ~ < 1 % have been experimentally found to produce SiO, a volatile species that evaporates at elevated temperatures, causing the particles to etch in low oxygen environments. A tandem size distribution showing this etching effect can be found in Fig. 5.2a with oxygen concentrations ~ 0.5%. Typical oxidation furnace temperatures are in the range of 700 to 1100°C with residence times ~ 8 sec. Lower oxidation temperatures produce poorer quality, nonstoichiometric oxides, whereas higher temperatures can evaporate silicon and SiO_x as it forms on the surface of the silicon nanoparticles. At the reactor exit, the evaporated volatile species can then produce a nucleation burst, leading to the formation of small particles that coagulate and attach to larger particles. Since oxygen is present, these particles can no longer be sintered, and distinct particles can be seen in these structures. A typical particle morphology shown in Fig. 5.3 results. In addition to changing the oxidation temperature, the oxide thickness can also be controlled by changing the residence time of the aerosol within the oxidation furnace where a longer residence time increases the oxide shell thickness.

Water vapor can also be used to oxidize silicon nanoparticles in a furnace via steam oxidation. In this case, the aerosol flows through a water evaporator that is maintained at a controlled temperature. The aerosol flow rate and water evaporator temperature are adjusted to control the water vapor partial pressure in the oxidation

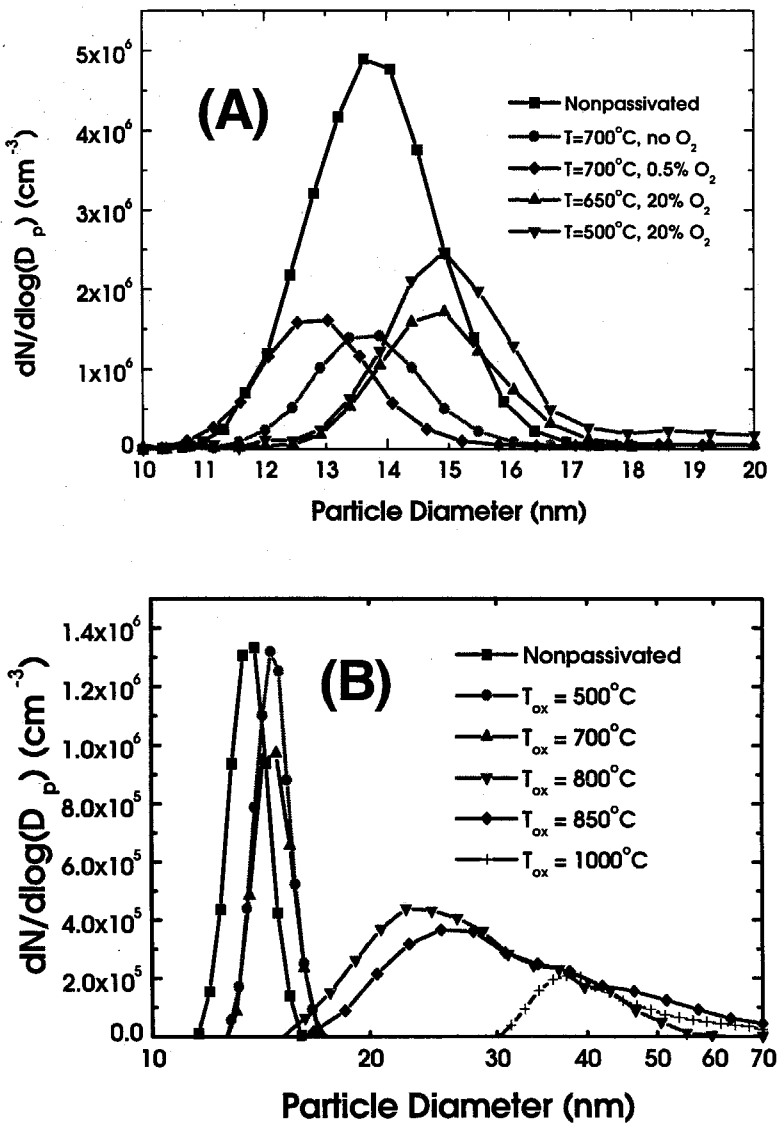

Figure 5.2: Size distributions following **(A)** thermal oxidation and **(B)** TEOS oxidation.

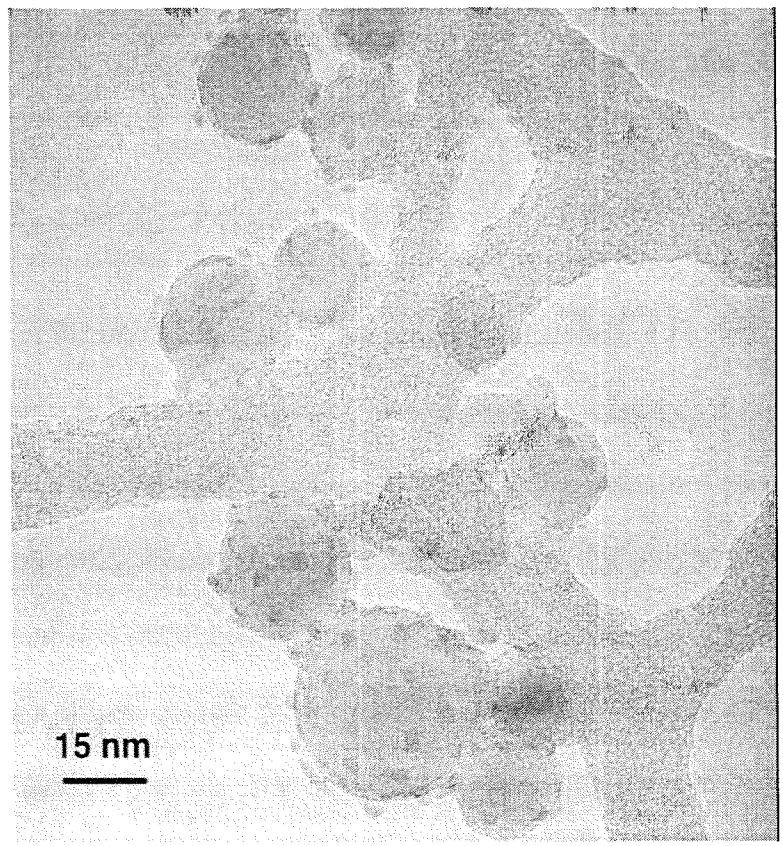

Figure 5.3: Silicon nanoparticle morphology following a nucleation burst at the exit of an oxidation furnace operating at a sufficient temperature to evaporate volatile species from the nanoparticle surface.

reactor. Downstream of the water evaporator, the aerosol and water pass through a high temperature tube reactor where surface oxidation at temperatures of 700°C to 1000°C passivates the particles. Excess water vapor does not appear to influence significantly the extent of oxidation of the particles.

5.3.2 TEOS Oxidation

Not only can silicon nanoparticles be oxide passivated by consuming the outer silicon material in the oxidation reactor, but precursors can be used to form SiO_2 that are then deposited onto silicon nanoparticles. To passivate particles with a TEOS oxide, the silicon nanoparticle aerosol passes over liquid TEOS in a temperature-controlled TEOS evaporator (or saturator). The temperature of the saturator (-23°C to 50°C) and the aerosol flow rate determine the TEOS concentration in the oxidation reactor. The TEOS containing aerosol stream enters a tube furnace where the TEOS reacts to form a silicon dioxide shell around the particle. The final silicon/silicon dioxide particle morphology and oxide thickness can be controlled by the oxidation temperature, the TEOS concentration, and the residence time within the reactor. Typical oxidation temperatures investigated were 300°C to 1000°C, and TEOS concentrations in the aerosol stream were 100 - 5000 ppm. The residence time in the TEOS oxidation reactor was ~ 8 s.

5.4 Particle Characterization

5.4.1 TEM

Samples for TEM analysis were collected by electrostatic precipitation directly onto amorphous holey carbon coated copper grids. TEM analysis was performed with a Philips EM430 operating at 300keV to determine the particle morphology, including shape, crystallinity, particle diameter, and dimensions of the crystalline core and amorphous shell. Bright field/dark field microscopy was used to measure particle dimensions and to estimate the core and shell dimensions from hundreds of individual particles. High resolution TEM was used to determine the particle crystalline core diameter and thickness of the amorphous oxide shell with a higher degree of accuracy than is possible with bright field/dark field images, although high resolution TEM provides fewer data points. Because these particles were deposited on amorphous holey carbon, the amorphous shell could only be measured in high resolution TEM on particles overhanging the holey carbon. Otherwise, the difference between amorphous SiO_2 on the particles and the amorphous holey carbon substrate was impossible to discern and an accurate measurement of the oxide shell could not be made.

5.4.2 Tandem RDMA

In a tandem RDMA experiment, two RDMAs are operated simultaneously in series. A thorough experimental description of tandem RDMA experiments can be found elsewhere [6],[7]. In this thesis, the first RDMA is continuously used to classify the polydisperse aerosol originating from the pyrolysis reactor by setting the voltage applied to the RDMA electrode to a specified value. The classified particles are then passivated with thermal oxide or TEOS oxide in the oxidation furnace, the second reactor. From this

oxidation reactor, the particles pass through a second RDMA that continuously measures the size distribution by scanning through a wide range of voltages that correspond to particle diameters between ~ 3 to 50 nm. With tandem RDMAs, the change in the particle size distribution that occurs after oxidation can be monitored on-line. The resolution of the RDMA is such that it can detect diameter changes on the nm scale.

5.4.3 Electrical Measurements

Electrical measurements were made by depositing silicon nanoparticles with native oxide, thermal oxide, or TEOS deposited oxide layers onto silicon substrates with a grown 100 nm wet thermal oxide layer. Two control samples, namely a bare 100 nm wet thermal oxide and a 50 nm polycrystalline film deposited by hot wire chemical vapor deposition, were also examined in this study for comparison of the electrical data. Aluminum gates were then deposited onto all samples under vacuum with a shadow mask to produce a well defined array of individual gates. Two metallic probes were placed onto neighboring aluminum gates and the voltage on one of the probes was scanned between 0 and 2 volts. The current flow between the two metallic probes was then measured.

5.4.4 Photoluminescence

Visible PL spectra were taken at room temperature using excitation with the 457 nm line of an Ar-ion laser at a power density of approximately 1 mW mm^{-2}. Phase sensitive detection was performed using a lock-in amplifier and accousto-optical

modulation of the excitation beam at a frequency of 1.1kHz. The luminescence spectrum was analyzed using a grating spectrometer with an InGaAs photomultiplier. All spectra were corrected for the system response. For PL decay measurements, samples were pumped to steady state using a power density of approximately 2 mW mm^{-2}. A multichannel photon counting system then monitored the luminescence decay with an InGaAs photomultiplier, proving time resolution of 500 ns.

5.5 Results

5.5.1 Native Oxide

Native oxide forms within minutes on a silicon surface upon exposure of silicon to air. In our particle synthesis reactor, native oxide on bare, unpassivated silicon nanoparticles begins to grow as soon as the sample is removed from the oxygen-free collection chamber. Within the particle collection chamber, oxidation is minimized by continuous flow of UHP N_2 aerosol carrier gas through the electrostatic precipitator nozzle toward the sample. Once the sample is removed from the collection chamber and is exposed to oxygen, the native oxide that forms on the particles forms only on the exposed areas of the silicon nanoparticles. Thus, in high density samples where particles accumulate into three-dimensional piles, regions where particles contact one another or the substrate are somewhat protected from oxidation.

The electrical measurements summarized in Fig. 5.4a show that the electrical behavior of dense layers of native oxide passivated samples closely resembles that of a

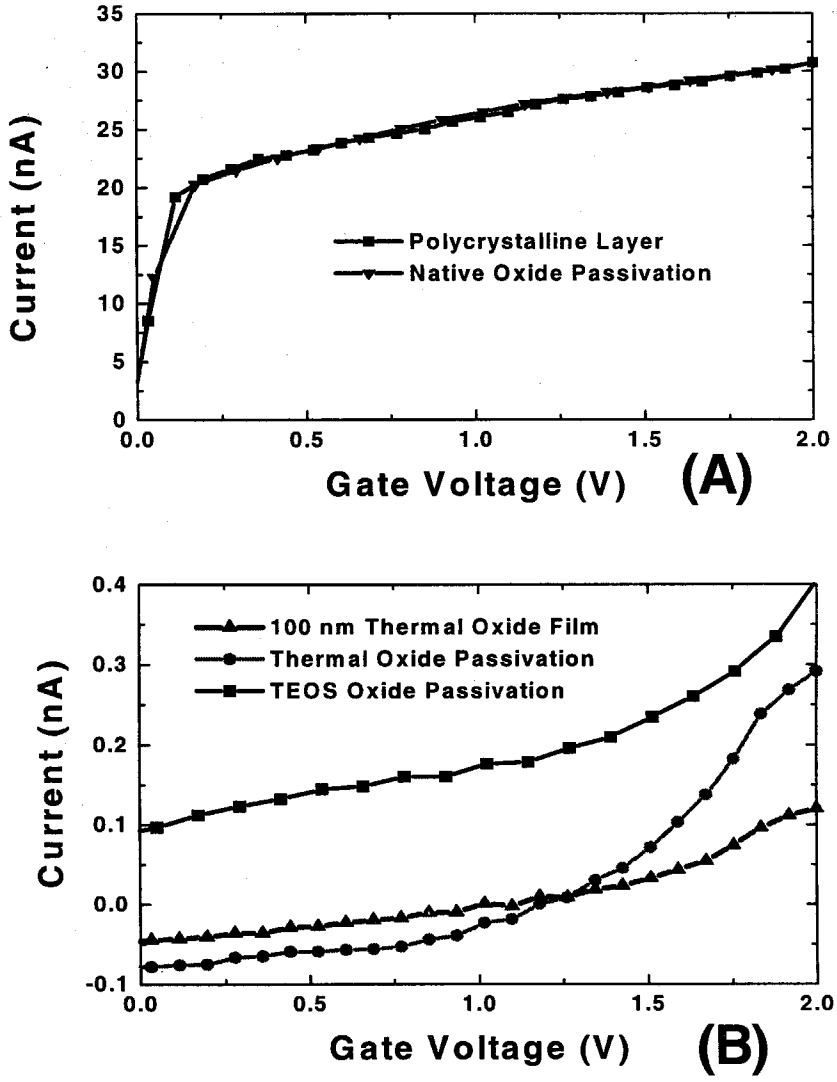

Figure 5.4: Current-Voltage relationships for **(A)** native oxide and **(B)** thermal and TEOS oxide -passivated samples with control samples.

deposited polycrystalline film. The high conductivity reveals that the native oxide passivated nanoparticles are in electrical contact with each other, providing evidence that the native oxide does not form within contact areas between adjacent nanoparticles.

TEM shows that particles that were initially classified at 10 nm form highly agglomerated structures once deposited on substrates. Furthermore, high resolution TEM reveals that the particles have undergone partial sintering at room temperature to produce grain boundaries between adjacent, contacting particles. Thus, the exposure of aggregates of unpassivated silicon nanoparticles can form electrically interconnected polycrystalline ensembles of particles that are encased in a native oxide shell, a statement supported by both electrical measurements and TEM observations.

Figure 5.5 shows that the crystalline cores of native oxide passivated nanoparticles typically amount to only 40 - 50% of the total particle volume. The native oxide thickness that forms on these particles is also relatively independent of particle diameter in the 3 to 30 nm size range. Room temperature oxidation consumes a large fraction of the silicon particle to produce a thick amorphous oxide shell. In contrast to the other oxidation processes examined in this thesis, room temperature oxidation forms the thickest oxide shells at small particle diameters. The poor quality native oxide is not stoichiometric silicon dioxide as measured by XPS, so it apparently can allow oxygen diffusion to continue through to the crystalline core even after the oxide thickness reaches several nanometers, a behavior that is unique to native oxidation.

5.5.2 High Temperature Thermal Oxides

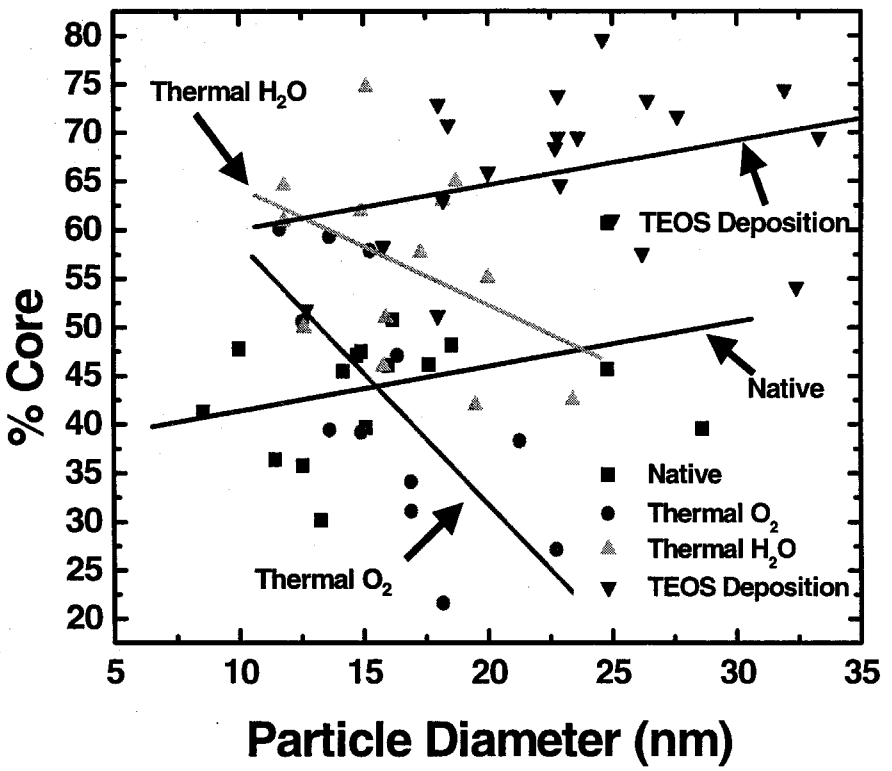

Figure 5.5: % Core versus Particle Diameter for four oxide-passivation methods.

5.5.2.1 Oxygen

Passivation of particles prior to substrate deposition leads to different particle morphologies than if oxide passivation occurs after particle deposition. As shown in Fig. 5.6, oxide passivated silicon nanoparticles can agglomerate after deposition due to the attractive van der Waals forces that cause these mobile nanoparticles to move towards each other. Despite the fact that these particles agglomerate together following deposition, no chemical bonding develops between particles. Individual particles remain easily distinguishable because the passivating oxide layer prevents the crystalline silicon cores from sintering together at room temperature.

As shown in Fig. 5.4b, thermal oxide passivated nanoparticle layers have a much lower conductivity than observed in the native oxide passivated particle deposits. Indeed, the conductivity of the thermal oxide passivated sample is comparable to the thermally grown SiO_2 film measured as a control, indicating that little current flows between adjacent nanoparticles. Thus, the particles are electrically isolated from one another, again, a result confirmed with both electrical and TEM observations.

From the analysis of numerous high resolution images and bright field/dark field TEM image pairs, the volume fraction occupied by the crystalline core ranges from 20 to 60% (see Fig. 5.5) and is seen to decrease with increasing total particle size (core plus oxide shell). Thus, thermal oxidation consumes more of large particles than it does small ones [8]. SiO_2 shells easily develop on small silicon nanoparticles. However, as the silicon dioxide shell thickens and the silicon core dimension decreases toward 10 nm diameter, oxidation of the remaining core becomes increasingly difficult at the oxidation

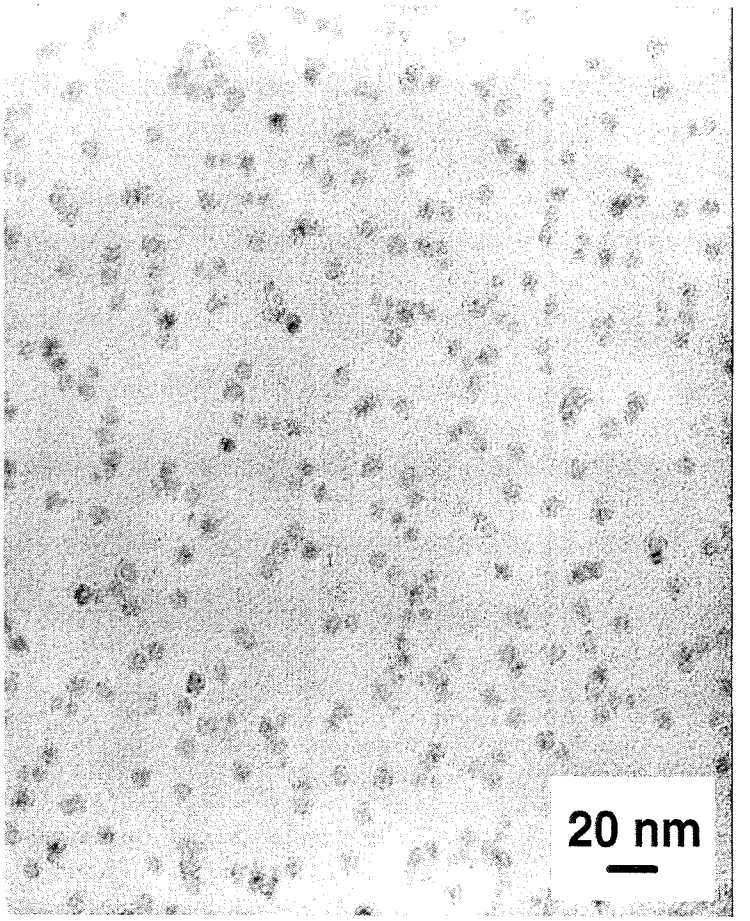

Figure 5.6: Thermal oxide passivated silicon nanoparticles. Oxidation occurred prior to particle deposition.

times and temperatures examined in this study. The residual core size is insensitive to the initial particle size, suggesting that as the core diameter approaches 10 nm, the silicon dioxide shell acts as an effective barrier to diffusion of oxygen from the gas phase to the crystalline core [9],[10]. High resolution TEM also reveals that the crystalline cores of these thermal oxide passivated silicon nanoparticles sometimes develop facets, especially in the smallest nanoparticles (~ 2 to 3 nm); the oxidation rate of silicon is a function of crystal orientation [11]. Indeed, XPS confirms that stoichiometric SiO_2 forms at temperatures between 1000 to 1100°C. Electrical measurements indicate high insulation quality SiO_2 and PL shows low defect density in the Si/SiO_2 interface.

Figure 5.2a shows tandem RDMA measurements of the changes in particle diameter that result from processing in the thermal oxidation reactor. Passing classified aerosol through the oxidation furnace at 700°C without exposure to oxygen does not shift the particle size to larger diameters, indicating that heat alone has no effect on particle size. The particle concentration decreases ~70% due to particle loss by thermophoretic deposition in the steep temperature gradient that persists near the furnace exit [12]. When a low amount of oxygen is added to the oxidation furnace (~ 0.5%), etching of the silicon nanoparticles occurs, resulting in a decrease in the particle diameter as measured by the second RDMA. Lower concentrations of oxygen in these thermal oxide reactors produce smaller particles than the original classified size. Low oxygen concentrations allow the formation of SiO, a volatile species that can evaporate from the particle surface, reducing the final particle size. When a controlled amount of oxygen (~ 20%) is added to the aerosol upstream of the oxidation furnace, the tandem RDMA experiments show a mean

particle size increases from 13.4 nm to 14.6 nm, indicating the presence of a silicon dioxide layer of 0.8 nm around the silicon crystalline core. As in the case of the thermal oxides, the oxide layer thickness results from the difference in the molecular volume of silicon and silicon dioxide. The thickness is larger than simply the difference in particle radii because silicon is consumed by thermal oxidation.

5.5.2.2 Water Vapor - Steam Oxidation

Amorphous oxide shells are also grown on silicon surfaces by exposure of silicon to water vapor at elevated temperatures [13]. Several samples of silicon nanoparticles oxidized with steam were prepared for TEM analysis. High resolution TEM indicates the presence of uniform oxide shells around these particles, with prominent faceting of many of the crystalline cores. In general, steam oxidation produced thinner amorphous shells than did either room temperature native oxide formation or thermal oxidation. The core volume fractions resulting from steam oxidation, summarized in Fig. 5.5, range from 45 to 65%. Steam oxidation penetrates less deeply into the particle cores than does O_2 oxidation. The amorphous shells of these steam oxidized particles are correspondingly thinner. The core volume fraction generally decreases with the increasing particle sizes, a trend also observed for the thermal oxide grown with oxygen, again indicating that resistance to steam oxidation is higher for small particles than for larger ones. At the oxidation temperatures and residence times used in this study, oxidation slows once the core diameter decreases below about 12 to 13 nm regardless of the initial particle sizes. However, particles below ~ 12 to 13 can still be oxidized, but only develop thin shells ~ <

1 nm.

5.5.3 TEOS Oxides

Thermal oxidation reduces the benefits of particle classification because of variability inherent in particle oxidation and the particle size dependence on oxide shell formation. As measured with TEM, thermal and steam oxide passivated particles have crystalline cores that are smaller than the diameter originally classified with the RDMA. To retain control over the silicon crystalline core size, we have developed a method for the deposition of silicon dioxide directly onto classified silicon nanoparticles using TEOS as the precursor. This enables oxide passivation of silicon nanoparticles without altering the diameter of the silicon core because the silicon particle does not react and silicon is not consumed.

A number of particle morphologies occur in TEOS oxide deposition, depending upon the oxidation temperature and processing conditions used. When TEOS partial pressures are maintained at ~ 100 ppm and at oxidation temperatures below 700°C, uniformly coated silicon nanoparticles are formed. Figure 5.7a shows a typical example of TEOS oxidation at TEOS concentrations 100 ppm and 700°C that produces a uniform 0.6 nm thick oxide layer on 10 nm classified silicon nanoparticles. High resolution TEM images, Fig. 5.7c, show a 1.2 nm thick amorphous shell uniformly deposited around a 20 nm classified silicon nanoparticle. The observed deposition rate (~ 4 - 9 nm/min) is within the range of previously reported rates (4-12 nm/min for atomic oxygen induced chemical vapor deposition (CVD) [14] and 2-200 nm/min for thermal TEOS (CVD)[15].

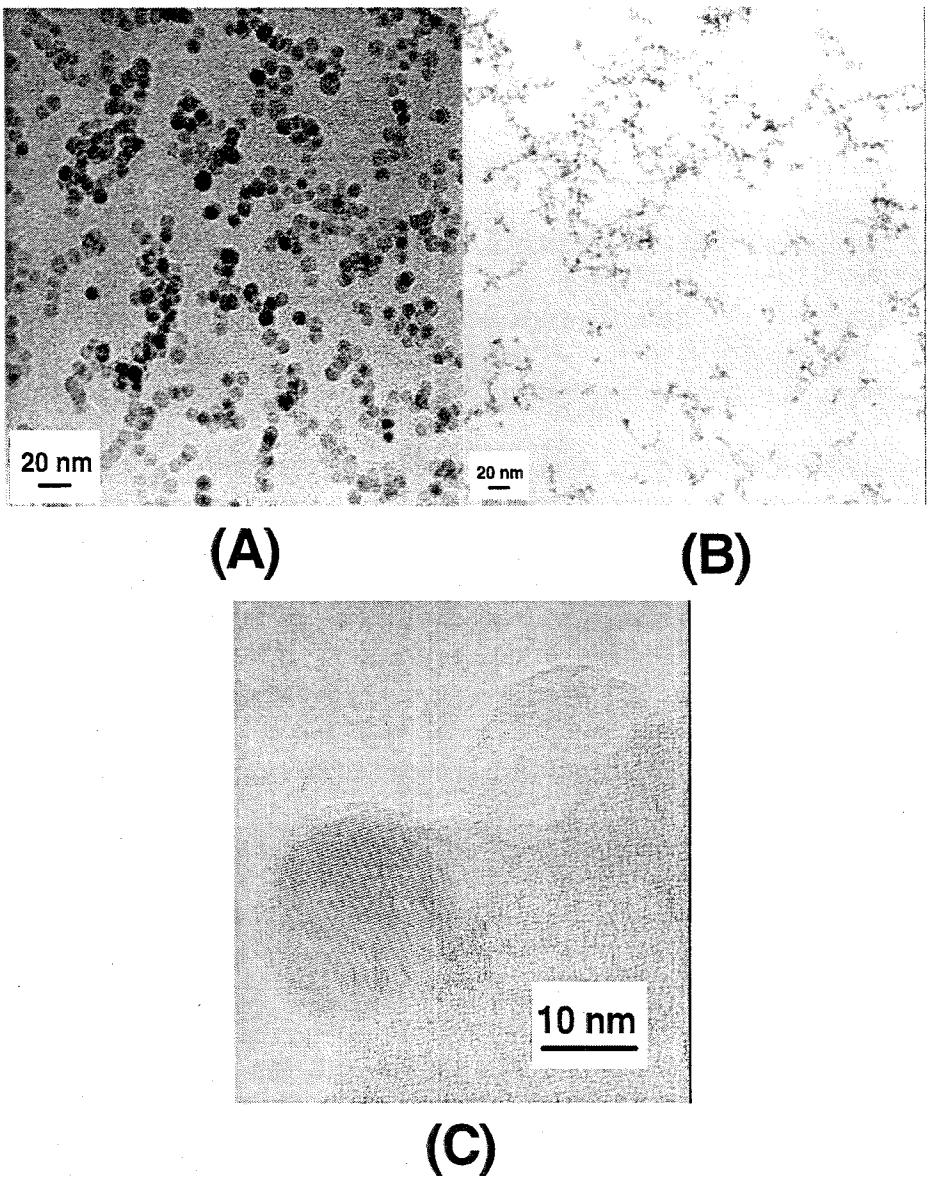

Figure 5.7: TEOS oxide passivated silicon nanoparticles at oxidation temperatures of **(A)** 700°C and **(B)** 900°C. **(C)** shows high resolution image of a uniform oxide shell from TEOS oxide passivated nanoparticles processed at 700°C.

At higher temperatures, 800 - 1000°C, and the same TEOS concentrations used in the previously discussed experiments, TEOS undergoes homogeneous nucleation to produce large concentrations of silica particles that then coagulate to form larger aerosol agglomerates or predominantly SiO_x material. These agglomerates form prior to particle deposition onto substrates. These agglomerates, shown in Fig. 5.7b, range in size from tens to hundreds of nanometers in size and are primarily composed of amorphous silica. TEOS is able to undergo homogeneous nucleation even at lower temperatures ~ 500°C, provided that the TEOS partial pressure in the reactor is sufficiently high ~ 1000 ppm. Care must be taken to insure that TEOS concentrations in the oxidation furnace do not exceed levels sufficient for homogeneous nucleation (~ 1000 ppm) since the agglomerates can quickly plug reactor tubes and fittings, restricting air flow rates and acting as effective filters in removing particles from the aerosol stream. A white film or "fluff" downstream of a TEOS oxidation furnace is usually good evidence of TEOS homogeneous nucleation.

From TEM, we find that silicon is not significantly consumed in the deposition (the core diameter measured from TEM is within the classified transmitted particle diameters measured with an RDMA). As shown in Fig. 5.2b, tandem RDMA measurements provide a direct measure of the TEOS oxide thickness *in situ*. At oxidation temperatures of 500°C and 700°C, particle diameters increase by about 1.2 nm. The thickness of the resulting oxide is simply the difference in the 2 radii, i.e., about 0.6 nm. Above about 750°C, the different TEOS oxide particle morphologies seen in the TEM are

also apparent in the tandem RDMA measurements. This agglomeration manifests itself as a drastic increases in measured particle diameters in the size distribution as well as a significant broadening of the size distribution.

The electrical conductivity of the TEOS oxide passivated samples shown in Fig. 5.4b is comparable to the 100 nm thermally grown SiO_2 film and the thermal oxide passivated nanoparticles. Thus, we conclude that the TEOS oxide passivated silicon nanoparticles are electrically isolated from one another. Furthermore, the TEOS oxide barrier is sufficient to insulate the nanoparticle cores from adjacent contacting particles.

Figure 5.5 shows that TEOS oxidation produces significantly thinner oxide shells than do the three previously discussed oxide passivation methods. For TEOS oxides, the core volume fraction ranges from 60 to 70%. Only the steam oxidation samples approach the thin shells obtained with TEOS oxidation. The TEOS oxide deposition rate and oxide thickness does not vary significantly with particle size. Since an oxidant need not diffuse through the oxide layer to produce the TEOS oxide shells, silica deposition proceeds unabated. This is in contrast to the decelerating oxide formation rate seen in both of the thermal oxidation samples (for oxygen and water).

In order to probe the quality and defect density of the silicon/silicon dioxide interface, we measured the room temperature PL of TEOS oxide passivated silicon nanoparticles. Figure 5.8a shows the PL spectra taken from TEOS oxide passivated nanoparticles with 8 nm and 12 nm cores. For the 12 nm TEOS oxide passivated sample, the ~ 1.1 μm peak wavelength in the luminescence spectra corresponds to an energy of 1.13 eV, close to the bandgap of bulk silicon, E_g = 1.17eV. Thus, 12 nm silicon

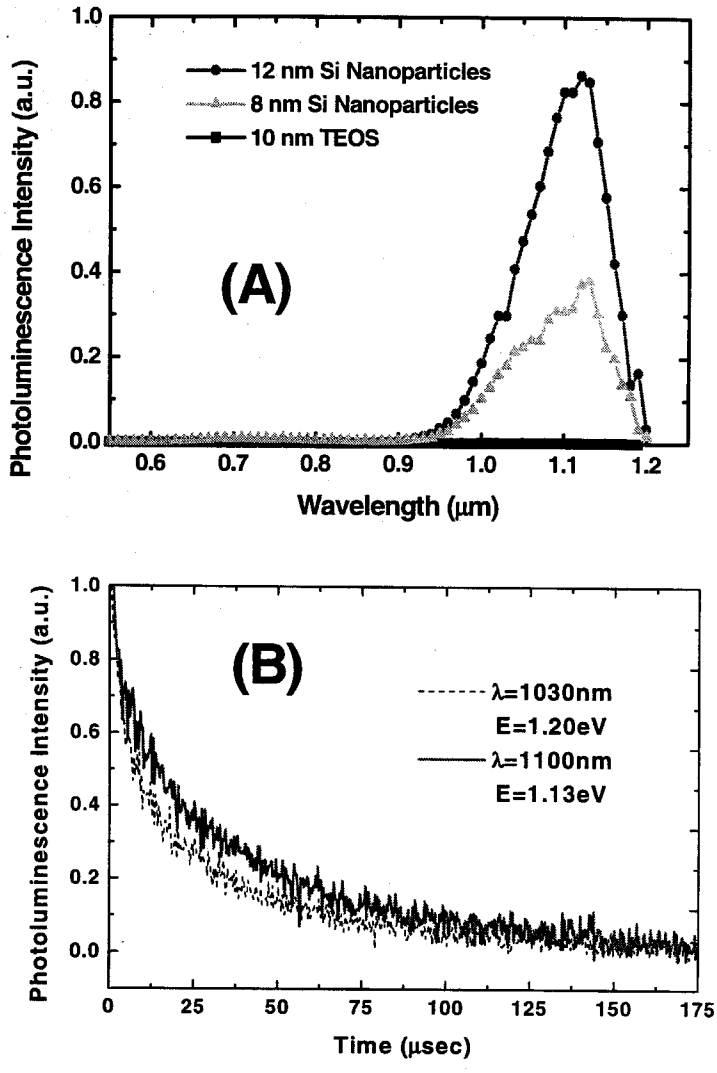

Figure 5.8: Photoluminescence measurements of TEOS oxide-passivated silicon nanoparticles: **(A)** photoluminescence spectra and **(B)** photoluminescence lifetime measurements.

nanoparticles behave as bulk silicon. For the 8 nm nanoparticle sample, the 1.03 μm peak wavelength corresponds to 1.21 eV, indicating that 8 nm particles are showing evidence of quantum confinement effects. It is well established that dangling bonds and defects in the silicon/silicon dioxide interface enable nonradiative decay processes that quench PL. The observed PL from silicon nanoparticles is an indication of the high quality interface that exists between the silicon nanoparticle core and the TEOS oxide coating. TEOS deposited SiO_2 with no silicon nanoparticles produced no PL spectrum, indicating that the observed PL results from the presence of TEOS oxide passivated silicon nanoparticles rather than from the TEOS oxide.

The room temperature PL lifetime decay reveals rather long lifetimes, consistent with phonon-mediated recombination of electron-hole pairs in cores of silicon nanoparticle. Figure 5.8b shows that the PL lifetime at 1.03 μm (t = 16 μs) is about half of the PL lifetime at 1.1 μm (t = 30 μs), providing direct evidence that lifetime is dependent on particle size. Moreover, the lifetime increases with increasing particle size in accordance with quantum confinement theory. The long PL lifetimes indicate that the PL is due to the presence of silicon nanocrystalline material and not from SiO_2 defects which have shorter lifetimes ~ 10 - 100 ns.

5.5.3.1 Pre-Treatment for TEOS Oxide

Efforts to passivate silicon nanoparticles with TEOS oxide at oxidation temperatures below about 450°C do not always produce a uniform coating. Instead, silica particles are observed to attach to the surface of the classified silicon nanoparticle. This

doublet structure is seen in Fig. 5.9. One explanation for this undesirable particle morphology is that TEOS does not wet the particle surface. It has been found that pretreating the nanoparticle surface prevents the formation of this undesirable doublet particle morphology. By exposing the classified nanoparticle aerosol to ethanol vapor prior to TEOS condensation and oxidation, a uniform amorphous shell forms around the crystalline core, even at oxidation temperatures below 450°C.

One important conclusion from the pretreatment of silicon nanoparticle surfaces is that the surface of the nanoparticle has a large effect on the final TEOS oxide wetting and conformation. Indeed, several sources also report on the necessity to pretreat silicon wafers in order to deposit TEOS oxides onto these planar surfaces [16],[17]. The method reported here has been found to improve the wetting behavior of TEOS for the silicon surface, but care should be taken to protect the silicon surface from adsorption of other species prior to oxidation. The present two-stage aerosol reactor set-up enables controlled oxidation before any surface contaminants can absorb onto the silicon nanoparticle that could potentially alter the Si/SiO_2 interface structure and electronic properties.

5.6 Summary

We have demonstrated the utility of multi-stage aerosol reactors for producing uniformly-sized oxide-passivated single crystal, nonagglomerated, spherical silicon nanoparticles. Uniform oxide shells can be grown or deposited on entrained aerosol

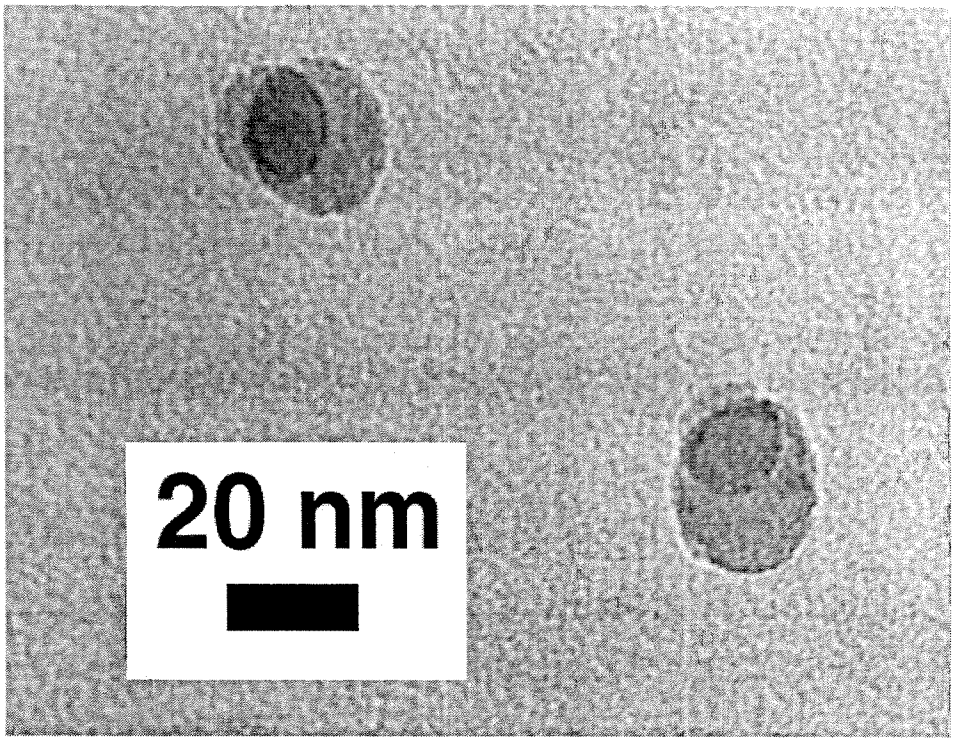

Figure 5.9: Doublet particle morphology following TEOS oxide passivation of untreated silicon nanoparticles at oxidation temperatures of 450°C.

particles by a number of routes. Thermal oxidation is an attractive method that has formed the basis of our device fabrication efforts because it is compatible with existing semiconductor technology and produces very high quality silicon dioxide layers of appropriate thickness on these nanoparticles. To prevent the reduction in the crystalline core size that is a necessary consequence of thermal oxide formation, we have developed alternate methods for depositing silicon dioxide directly onto the silicon nanoparticle using a TEOS deposition process. The resulting TEOS oxide is uniform around the entire nanoparticle and is sufficiently thin to be of use in nanoparticle memories. PL measurements indicate the presence of a high quality interface between deposited TEOS oxide and silicon nanoparticles.

In situ oxide passivation of silicon nanoparticles remains an area of active research because of the importance of producing high quality, well passivated silicon nanoparticles for electronic memory devices. The ability to produce uniform shells of very thin silicon dioxide around single crystal silicon nanoparticles is an exciting development in the applications of these particles for future devices.

Bibliography

[1] S. Tiwari, F. Rana, H. Hanafi, A. Hartstein, E.F. Crabbe, and K. Chan, "A Silicon Nanocrystals Based Memory," *Appl. Phys. Lett.*, **68**, pp. 1377-1379 (1996).

[2] S. Tiwari, F. Rana, K. Chan, L. Shi, and H. Hanafi, "Single Charge and Confinement Effects in Nano-Crystal Memories," *Appl. Phys. Lett.*, **69**, pp. 1232-1234 (1996).

[3] H.I. Hanafi, S. Tiwari, and I. Khan, "Fast and Long Retention-Time Nano-Crystal Memory," *IEEE Trans. Electron Dev.*, **43**, pp. 1553-1558 (1996).

[4] K.A. Littau, P.J. Szajowski, A.J. Muller, A.R. Kortan, and L.E. Brus, "A Luminescence Silicon Nanocrystal Colloid via a High-Temperature Aerosol Reaction," *J. Phys. Chem.*, **97**, pp. 1224-1230 (1993).

[5] W.L. Wilson, P.F. Szajowski, and L.E. Brus, "Quantum Confinement in Size-Selected Surface-Oxidized Silicon Nanocrystals," *Science*, **262**, pp. 1242-1244 (1993).

[6] S.H. Zhang, Y. Akutsu, L.M. Russell, R.C. Flagan, and J.H. Seinfeld, "Radial Differential Mobility Analyzer," *Aerosol Sci. Technol.*, **23**, pp. 357-372 (1995).

[7] S.H. Zhang and R.C. Flagan, "Resolution of the Radial Differential Mobility Analyzer for Ultrafine Particles," *J. Aerosol Sci.* **27**, pp. 1179-1200 (1996).

[8] R. Okada and S. Iijima, "Oxidation Property of Silicon Small Particles," *Appl. Phys. Lett.*, **58**, pp. 1662-1663 (1991).

[9] D.B. Kao, J.P. McVittie, W.D. Nix, and K.C. Saraswat, "Two-Dimensional Thermal Oxidation of Silicon - II. Modeling Stress Effects in Wet Oxides," *IEEE*

Trans. Electr. Dev., ED-35, pp. 25 - 37 (1988).

[10] J. Tersoff, Y. Tu, and G. Grinstein, "Effect of Curvature and Stress on Reaction Rates at Solid Surfaces," *Appl. Phys. Lett.*, **73**, pp. 2328-2330 (1998).

[11] E.A. Irene, H.Z. Massoud, and E. Tierney, "Silicon Oxidation Studies - Silicon Orientation Effects on Thermal Oxidation," *J. Electrochem. Soc.*, **133**, pp. 1253-1256 (1986).

[12] H.V. Nguyen and R.C. Flagan, "Particle Formation and Growth in Single-Stage Aerosol Reactors," *Langmuir*, **7**, pp. 1807-1814 (1991).

[13] J. Appenzeller, J.A. del Alamo, R. Martel, K. Chan, and P. Solomon, "Ultrathin 600 degree C Wet Thermal Silicon Dioxide," *Electrochem. Solid State*, **3**, pp. 84-86 (2000).

[14] A.M. Wrobel, A. Walkiewicz-Pietrzykowska, S. Wickramanayaka, and Y. Hatanaka, "Mechanism of Amorphous Silica Film Formation from Tetraethoxysilane in Atomic Oxygen-Induced Chemical Vapor Deposition," *J. Electrochem. Soc.*, **145**, pp. 2866-2876 (1998).

[15] S. Nguyen, D. Dobuzinsky, D. Harmon, R. Gleason, and S. Fridmann, "Reaction-Mechanisms of Plasma-Assisted and Thermal-Assisted Chemical Vapor-Deposition of Tetraethylorthosilicate Oxide-Films," *J. Electrochem. Soc.*, **137**, pp. 2209-2215 (1990).

[16] K. Tsukamoto, D.G. Cheng, H. Komiyama, Y. Nishimoto, N. Tokumasu, and K. Maeda, "Tetraethylorthosilicate Vapor Treatment for Eliminating Surface Sensitivity in Tetraethylorthosilicate/O-3 Atmospheric-Pressure Chemical Vapor

Deposition," *Electrochem. Solid State*, **2**, pp. 24-26 (1999).

[17] K. Kinashi, M. Niwano, N. Miyamoto, and K. Honma, "UV-Assisted Deposition of TEOS SiO2-Films Using the Spin-Coating Method," *App. Surf. Sci.*, **80**, pp. 332-337 (1994).

Chapter 6: Ultra Clean Two-Stage Aerosol Reactor for the Production of Oxide-Passivated Silicon Nanoparticles for Novel Memory Devices

6.1 Introduction

Silicon nanoparticle-based floating gate MOS field effect devices are attractive candidates for terabit cm^{-2} density nonvolatile memory applications. Several methods exist for the fabrication of these nanoparticle floating gate structures embedded in SiO_2, including ion implantation, silicon-rich oxide (SRO) deposition and anneal, low pressure chemical vapor deposition (LPCVD), and aerosol deposition. As already discussed, aerosol synthesis is an important route toward the formation of silicon nanoparticle floating gate structures that affords excellent control over particle size and size distribution, particle density, and oxide passivation to prevent lateral charge conduction. For this reason, we have designed an ultra clean two-stage aerosol process reactor and 200 mm wafer deposition chamber in order to integrate aerosol Si/SiO_2 nanoparticles into floating gate memory devices. In the first stage, silicon nanoparticles are synthesized by thermal decomposition of silane gas in a reactor that has been optimized to produce nonagglomerated nanoparticles at rates sufficient for layer deposition. In the second stage, the silicon particles are passivated with thermal oxide that is sufficient to electrically

isolate adjacent nanoparticles to produce a truly discontinuous floating gate. This two-stage aerosol reactor has been integrated to a 200 mm silicon wafer deposition chamber that is contained within a class 100 cleanroom environment. This entire reactor system conforms to rigorous cleanliness specifications dictated by the semiconductor industry such that we can control transition and alkali metal contamination to as good as 10^{10} atoms cm^{-2}. The deposition chamber has been designed to produce a controllable particle density profile along a 200 mm wafer where particles are thermophoretically deposited uniformly over three-quarters of the wafer. Thus, we have the capability to deposit controlled densities of oxide-passivated silicon nanoparticles onto 200 mm silicon wafers for state-of-the-art ultra-large scale integration (ULSI) fabrication of silicon nanoparticle memory devices.

Aerosol and other particles are anathema to microelectronic device fabrication. Not only do particles create defects that lead directly to device failure, they may also transport contaminants such as transition metals that degrade device performance. We seek to produce near-monolayer coverage of the floating gate region with nanoparticles that are formed in a high-temperature aerosol reactor. A monolayer is defined as the number of particles required to produce a single hexagonal close-packed particle layer. The high temperature reactive atmosphere could lead to evaporation of such contaminants from surfaces in the reactor. The high surface area of the nanoparticles, approximately 7 times the wafer area at monolayer coverage by uniformly-sized particles, increases the risk of contamination since the particles will effectively getter contaminant vapors as the aerosol cools. Furthermore, contaminants can also be introduced into or on particles

during synthesis and oxidation processing. An aerosol process can only be incorporated into device fabrication if the contamination issues can be addressed and minimized to acceptably low contamination levels.

This chapter describes an aerosol synthesis and deposition tool that meets the stringent cleanliness requirements of a modern fabrication facility while simultaneously offering the advantages that aerosol synthesis of these nanoparticle floating gate devices is able to provide. Surface contamination of transition metals, e.g., Fe, Cr, and Zn, and Li, Na, K, and Al have been kept below or close to 10^{10} atoms cm^{-2} while depositing approximately 10^{12} silicon nanoparticles cm^{-2} on the surface of 200 mm wafers, enabling ULSI compatible production of aerosol nanoparticle discontinuous floating gate devices with novel properties.

6.2 Experimental Set-Up

6.2.1 Gas Delivery System

The ultra clean two-stage aerosol reactor system is illustrated in Fig. 6.1. Electronic grade gases (0.5% silane(SiH_4) in nitrogen, nitrogen, and oxygen) were used as received from Matheson. Ultraline gas regulators were purchased from Matheson Tri-Gas. To remove trace amounts of oxygen from the pyrolysis furnace upstream of the oxidation furnace, a Nanochem PuriFilter PF-25 was placed after the gas regulator on the nitrogen stream. Mass flow controllers (2000 sccm MKS Instruments, Inc.) with VCR connections control the 1500 sccm nitrogen and variable oxygen flows. An ultra clean

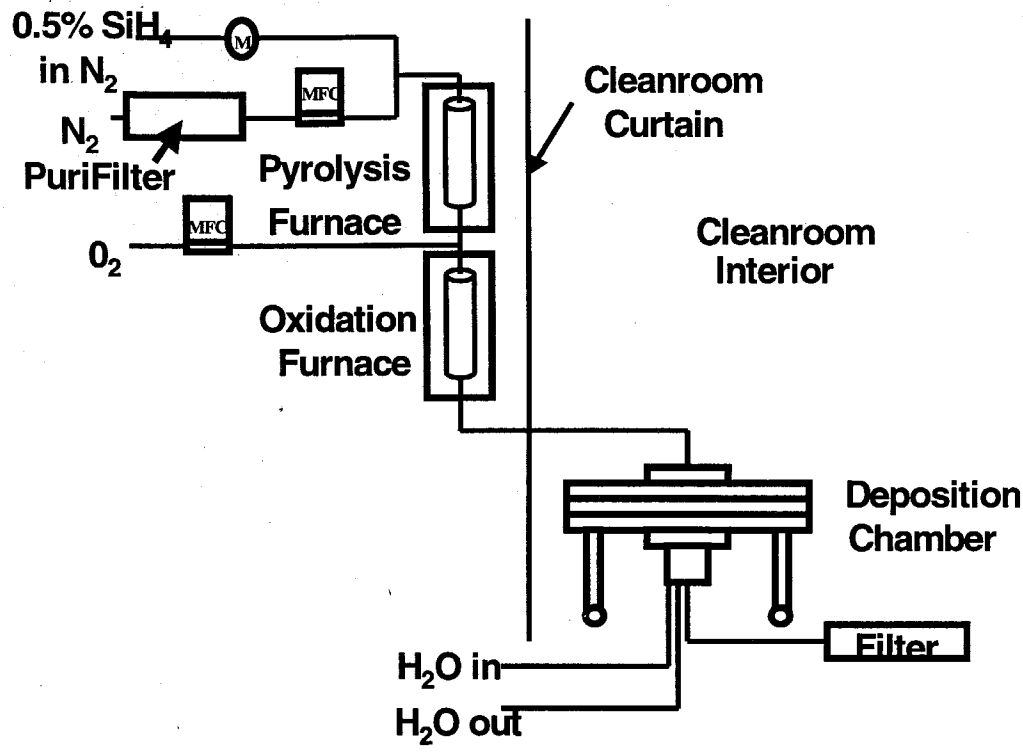

Figure 6.1: Schematic of the ultra clean two-stage aerosol reactor and 200 mm wafer deposition chamber.

metering valve from Nupro Co. was used to control the very small yet reproducible (<1 sccm) silane flow rate. Quarter-inch 316 stainless steel tubing was obtained from Valex Corp. with an electropolished finish maximum of 10 roughness average (R.A.). All connections were made with VCR fittings from Cajon Co. with an electropolished finish of 7-10 R.A. Straight pieces of 1/4" 316 stainless steel tubing were cut and VCR glands were welded in an ultra high pure argon environment at G.R. Babcock Co. All pieces were then electropolished and passivated at Electromatic to an R.A. of 7-10. Any bends in the system were made with VCR elbows, not by bending the electropolished tubing.

6.2.2 Furnaces

The SiH_4 pyrolysis tube furnace operates at 900 - 950°C with a total heated length of 20 cm. The oxidation tube furnace operates at 1050 - 1100°C with a total heated length of 36 cm. Given typical flow rates of gases through both furnaces (1.5 LPM for pyrolysis and 1.75 LPM for oxidation), a 19 mm outer diameter /17 mm inner diameter quartz tube gives a residence time of ~ 3 sec in each furnace. An hour prior to making silicon nanoparticle samples, the nitrogen flow is turned on so that most residual oxygen in the system is removed. No SiH_4 is introduced into the system until the temperature of the pyrolysis furnace reaches 900°C to insure complete reaction of SiH_4.

Electronic grade quartz tubing (19 mm outer diameter /17 mm inner diameter) from GM Associates, Inc., was treated with an RCA clean (a recipe developed by the RCA Company) prior to installation in each furnace. For the RCA clean, all liquid reagents used were electronic or semiconductor grade purity obtained from Aldrich. For

the RCA clean, the quartz tubes were first immersed in 18MΩ H_2O:30%H_2O_2:NH_4OH in the volume ratio of 5:1:1 at 80°C for 20 minutes. The tubes were then rinsed with 18MΩ H_2O. To remove heavy metals, the tubes were immersed in 18MΩ H_2O:30%H_2O_2:HCl in the volume ratio of 6:1:1 at 80°C for 20 minutes. Again, the tubes were rinsed with 18MΩ H_2O. At no time in the cutting, cleaning, or installation process were these tubes touched with bare hands. Furthermore, the quartz tubes were not firepolished on the ends because no clean system is available at Caltech. A clean, certified system is required for quartz tube firepolishing or else metallic contaminants can easily be melted into the quartz tube ends, producing extremely high sources of contamination that can leach out of the quartz at high temperatures (as those encountered in the 900 to 1100°C furnaces) during the entire lifetime of the quartz tubing. The quartz tubes were installed in the reactor system with electropolished Ultra-Torr fittings (R.A. 7-10) and semiconductor grade viton o-ring seals from Cajon Co. that interfaced to VCR fittings.

6.2.3 Deposition Chamber

The deposition chamber is constructed from 316 stainless steel vacuum flanges from MDC Vacuum Products Corp. as shown schematically in Fig. 6.2. This chamber is radially symmetric. The aerosol flow enters the top of the deposition chamber along its centerline axis. The gas velocity decreases as it moves radially outward along the wafer surface. The gas then exits the chamber below the wafer at the center of the deposition chamber. The particles deposit on the top of the cooled wafer surface by thermophoresis. The top of the deposition chamber is heated to ~ 200°C and the water cooled disk in the

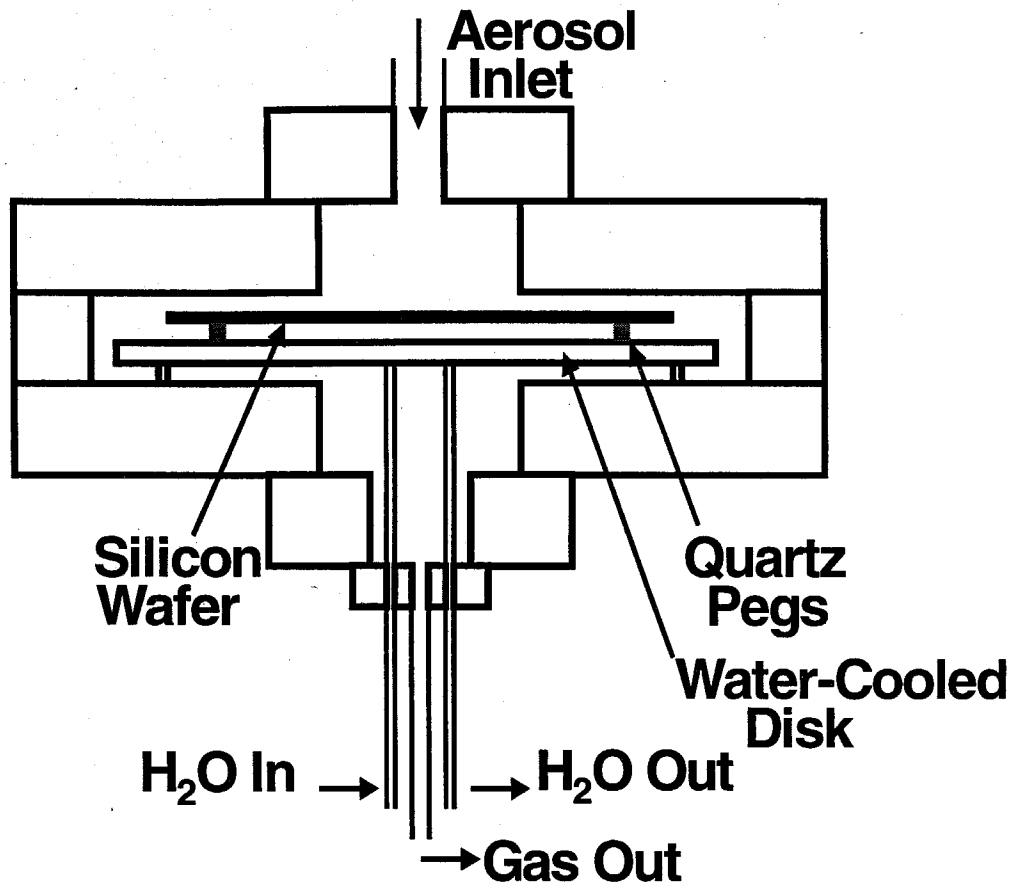

Figure 6.2: Schematic of the ultra clean 200 mm wafer deposition chamber.

interior of the chamber is maintained at 23°C with a cooling water supply. Since the particles migrate by thermal diffusion from high temperatures toward lower ones, the particles deposit onto the silicon wafer. By controlling the temperatures of the deposition chamber and the water-cooled disk and the position of the wafer with respect to these structures, the approximate temperature of the wafer can be calculated. On the bottom side of the 9 inch diameter water cooled disk (away from the aerosol inlet), 1/8" copper tubing encased in a stainless steel shell is wound around the disk to maximize heat exchange. Room temperature water flows through this 1/8" copper tubing and serves to maintain a temperature gradient within the deposition chamber, the important temperature gradient being the one between the deposition chamber and the silicon wafer. To eliminate any physical contact between the metallic deposition chamber and the silicon wafer, the silicon wafer is supported by three quartz pegs that have been RCA cleaned using the same procedure used to clean the furnace quartz tubes. The quartz pegs rest on the top surface of the water cooled disk or into shallow indentations drilled into the disk. Only a small contact area is made between these three quartz pegs and the silicon wafer. The interior surfaces of the deposition chamber and the entire water cooled disk assembly were electropolished to an R.A. of 7-10 at Electromatic prior to use.

6.2.4 Class 100 Cleanroom

A class 100 cleanroom from Terra Universal, Inc., is used to store wafers and to house the deposition chamber. The two-stage aerosol reactor is located outside of the cleanroom. The 1/4" stainless steel tube that connects the reactor to the deposition

chamber passes through a small hole in the cleanroom wall. Basic cleanroom procedures are outlined in Appendix B of this thesis.

6.3 TXRF/SIMS

Total Reflection X-Ray Fluorescence (TXRF) and Secondary Ion Mass Spectrometry (SIMS) measurements were made by Charles Evans & Associates (CE&A). TXRF analysis was performed with a TREX 610-T TXRF instrument and SurfaceSIMS analysis was performed with a CAMECA IMS. Prior to building the class 100 cleanroom, ultra clean reactor and deposition chamber, TXRF analysis was performed on a 1 cm^2 wafer sample with deposited silicon nanoparticles. For this sample, the substrate and particles were exposed to normal laboratory operating conditions. Great care was taken to insure that the sample would be as clean as possible. As will be discussed in the next section, the high contamination measured on this sample provided the necessary motivation to design and build the ultra clean reactors and deposition chamber in the cleanroom environment.

Once the cleanroom and ultra clean reactor and deposition chamber were built, 200 mm wafer samples were prepared for TXRF/SIMS analysis. A cleanroom sample was prepared by exposing a silicon wafer to the cleanroom environment for 5 minutes. In preparing this sample, the wafer was removed from the wafer box, carried to and from the deposition chamber with a quartz fork (purchased from Quartz Intl.) a total of five times without putting the wafer into the deposition chamber. The wafer was then replaced in the

wafer box. This procedure was used to simulate the worst-case scenario of wafer transport around the cleanroom prior to and following sample preparation. The next samples prepared were two TXRF/SIMS samples that were made without depositing particles onto the wafers. These samples were prepared with the silane flow off, but the nitrogen and oxygen flows on for estimated collection times approximately five times longer than expected for actual sample collection. These samples were used to verify the cleanliness of the gas delivery systems and the furnaces operating at normal conditions.

Four additional wafer samples were put into the deposition chamber separately and particles were then deposited on them: two wafers with particle deposits onto the front side of the wafers and the other two wafers with particle deposits onto the back side of the wafers. Both frontside and backside deposition was required to verify that both sides of the wafers would remain clean in this deposition chamber and with the wafer transport available. In these experiments, the reactor was operating at the normal conditions expected for sample collection. For each of the frontside and backside samples, one wafer was made with the oxidation furnace off (no thermal) and the other with it turned on (thermal). Particles were deposited on the wafer surface for a total collection time five times longer than expected for nanoparticle device fabrication, providing a worst-case scenario for contamination. Dense nanoparticle deposits were readily visible on these wafer surfaces.

The TXRF results performed by CE&A appear in Fig 6.3a. The "lab conditions" sample was prepared prior to building the ultra clean reactor and deposition chamber. Since this sample showed unacceptably high levels of contamination, the necessity for

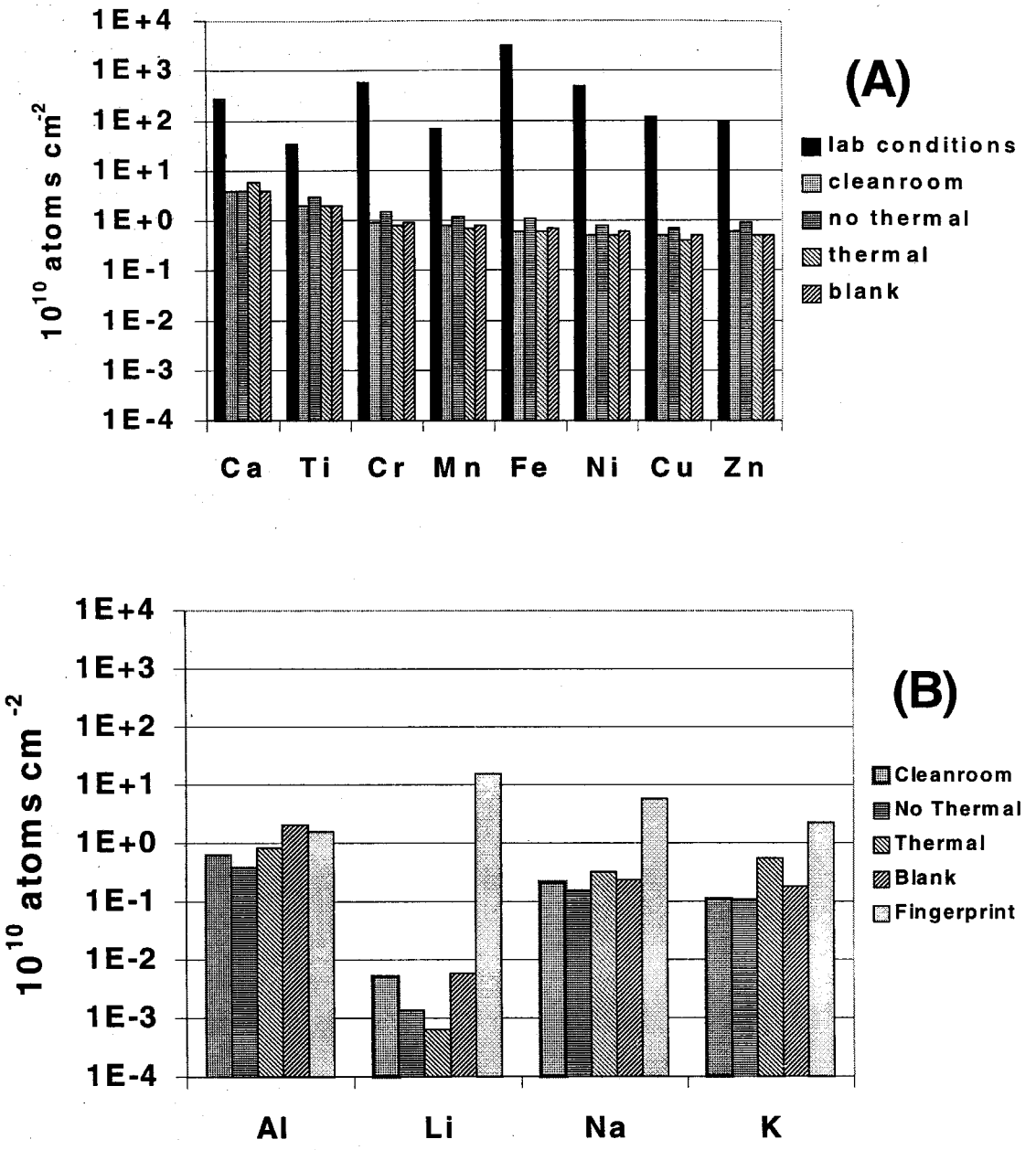

Figure 6.3: **(A)** TXRF and **(B)** SIMS results for wafer samples.

building the ultra clean reactor, deposition chamber, and cleanroom became apparent. The "blank" sample provided by CE&A was considered to be free of any contamination. All wafers made in the ultra clean reactor and deposition chamber clearly demonstrates dramatic decreases in the levels of contamination measured by TXRF. SIMS measurements of Al, K, Na, and Li of the wafers produced in the ultra clean reactor and the cleanroom exposed wafer are presented in Fig. 6.3b along with the "blank" sample. Again, no significant contamination was detected in the samples handled in the ultra clean reactor and deposition chamber. A fingerprint on the outside of a quartz tube did leave significant contamination.

When analyzing TXRF and SIMS data, any reported contamination values within a factor of 2 of the atoms cm^{-2} values measured on the "blank" are regarded as the upper limits of the actual contamination. Thus, a wafer is still considered to be contamination-free if its measured surface concentration is a factor of 2 larger than the "blank" wafer. Since no contamination levels greater than 10^{11} atoms cm^{-2} were detected, the system is operating within acceptable contamination levels.

6.4 Particle Characterization

6.4.1 Particle Size Distribution

To date, the ultra clean reactor does not utilize size classification because an ultra clean RDMA has not been built. Thus, the particle size distribution has to be controlled by the silane concentration in the two-stage aerosol reactor (done by varying the silane

inlet flow rate). Figure 6.4 shows the resulting variation in the particle size distribution with silane concentration of thermal oxide passivated silicon nanoparticles produced in the two-stage aerosol reactor. These size distributions have been measured with a radial differential mobility analyzer and an electrometer as a detector. These instruments are connected downstream of the aerosol reactors and before the deposition chamber and are not connected in series within the ultra clean reactor. In measuring the size distributions, great care must be taken to insure that no contamination from the RDMA equipment and plumbing enters the ultra clean reactors and deposition chamber. When not in use and always when collecting wafer samples, the RDMA is isolated from the ultra clean system via two ultra clean valves.

The resulting particle size distributions of thermal oxide-passivated silicon nanoparticles from the ultra clean reactor vary by about 50% on diameter. By decreasing the silane concentration in the reactor, the particle size distribution shifts to smaller particle sizes and lower particle concentrations. At a given silane concentration, the resulting particle size distribution is extremely stable over time with unmeasurable fluctuations even over a 7 day period.

6.4.2 Particle Structure

As described in earlier chapters, extensive work has been done to produce uniformly-sized, nonagglomerated, single crystal Si/SiO_2 nanoparticles for applications in nonvolatile memory devices. The two-stage aerosol reactor is capable of making high quality particles that are dense, spherical, nonagglomerated single crystals. Samples of

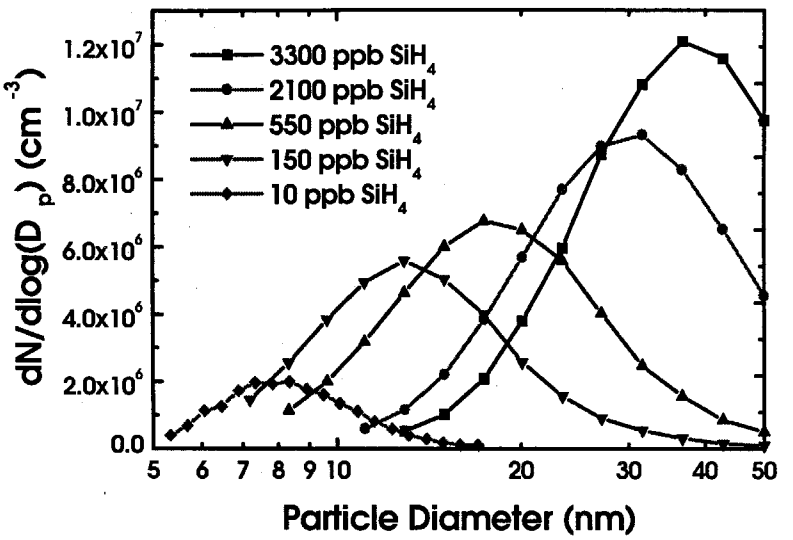

Figure 6.4: Effect of silane concentration on the thermal oxide-passivated silicon nanoparticle size distribution.

thermal oxide passivated silicon nanoparticles fabricated in the ultra clean system were examined with TEM and are spherical single crystal nonagglomerated particles between 3 - 7 nm in size as represented by the 10 ppb SiH_4 curve in Fig. 6.4. There is good agreement between the RDMA size distributions and the particle diameters as measured with TEM.

6.5 Deposition Chamber Modeling

The 200 mm wafer deposition chamber was modeled using the commercial computational fluid dynamics code FLUENT to calculate velocity streamlines and temperature contours. Particle trajectories were determined by modifying FLUENT to include the thermophoretic velocity of particles in a temperature gradient. These particle trajectories were used to estimate the uniformity of particle deposits and the particle deposition profile and to understand design improvements that could be implemented in the future to obtain more uniform nanoparticle deposits. This model allows one to vary such parameters as the inlet aerosol flow rate, the temperature of the heated deposition chamber top, the temperature of the water cooled disk, and the gap spacing between the inside of the top deposition chamber and the upper wafer surface. Figure 6.5 shows calculated (a) velocity streamlines, (b) temperature contours, and (c) particle trajectories for appropriate conditions used in device fabrication.

As seen in the velocity streamlines (Fig. 6.5a), the abrupt expansion in the flow cross section near the entrance to the deposition chamber (top) leads to a large

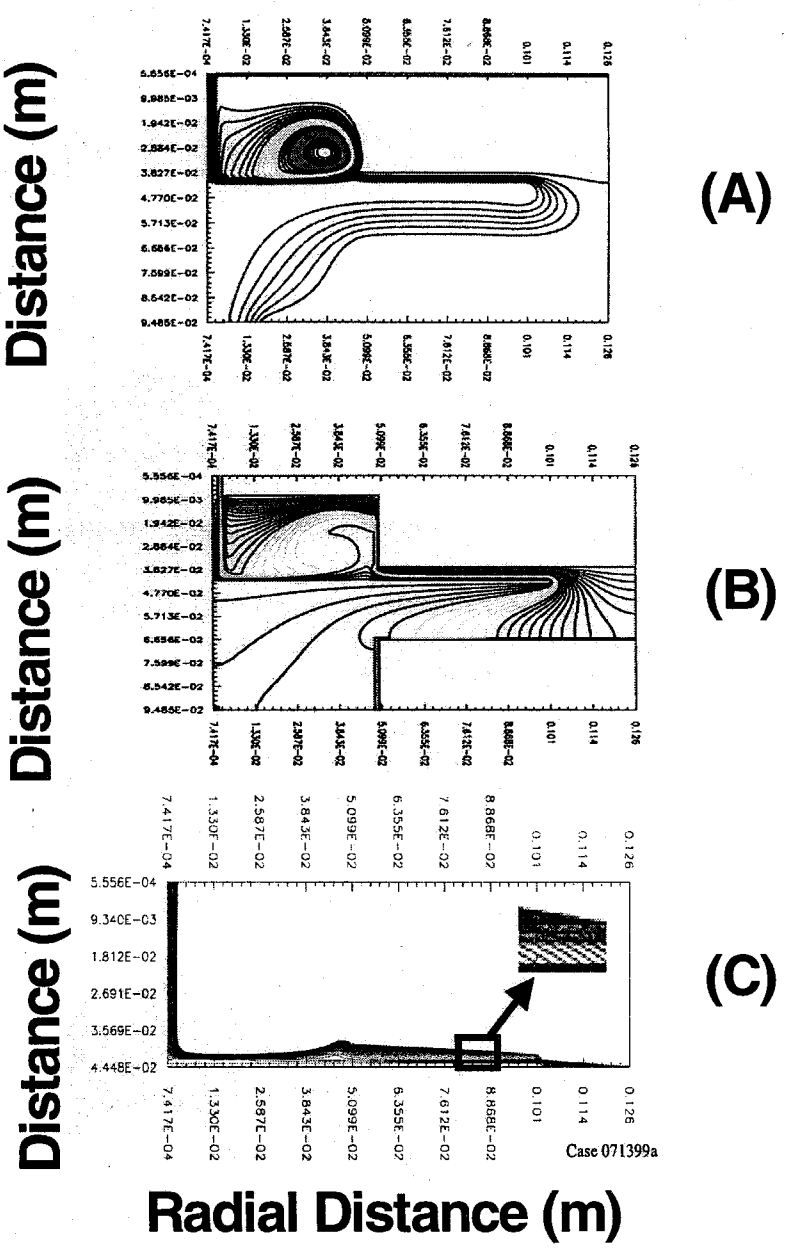

Figure 6.5: FLUENT calculations of **(A)** velocity streamlines, **(B)** temperature contours, and **(C)** particle trajectories.

recirculation region. Most of the incoming flow remains in a well defined jet near the centerline until it approaches the wafer surface where it forms a radial outward wall layer flow. The flow deviates from the wafer surface near the edge of this expansion region, but quickly reestablishes laminar radial flow in the outer regions where the spacing between the deposition chamber plate and wafer are constant. Below the wafer and the cooling plate, the flow is drawn radially inward toward the central outlet port.

The temperature contours (Fig. 6.5b) are also strongly influenced by the recirculation within the expansion region. The temperature gradient is high in the central jet impingement region, decreases near the expansion region edge, and then increases dramatically but remains uniform in the outer region where the flow is confined to the constant small gap between the deposition chamber plate and the wafer surface.

In the absence of a thermal gradient or any other external force, such as an electrostatic or gravitational force, particle trajectories (Fig. 6.5c) follow the incoming gas streamlines. However, the particles are affected by the temperature gradient within the deposition chamber. To account for these thermophoretic forces, an additional component to the particle velocity, the thermophoretic velocity v_t, is calculated using the expression

$$v_T = -\frac{Th\mu \frac{dT}{dx}}{\rho T} \tag{6.1}$$

Th is the thermal dimensionless group and is assumed to be 0.5 for nanoparticles, and μ,

ρ, and T are the viscosity, density, and temperature of the carrier gas (nitrogen in this study). As seen from the equation, as the temperature gradient (dT/dx) increases, the thermophoretic velocity also increases. This v_t is normal to the temperature gradient. This thermophoretic force produces the necessary driving force to the particle motion so that particles will deposit onto the wafer surface instead of simply following the velocity streamlines.

6.6 Particle Deposition

In order to verify particle deposition, a total of ten separate aerosol samples were collected on 200 mm wafers by changing such parameters as the inlet aerosol velocity, the temperature of top plate, the collection time, and the gap spacing between the wafer and the deposition chamber. The aerosol flow rate was changed by altering the flow rate of oxygen in the oxidation furnace. The gap spacing was changed by using different lengths of quartz pegs to support the silicon wafer. After each specified collection time, the wafers were removed from the deposition chamber and particle densities were measured with an atomic force microscope (AFM). Ten measurements of particle density were taken per wafer at 1 cm intervals from the edge of the wafer toward the wafer center to obtain a radial particle density profile. The resulting AFM images were used to estimate particle densities by counting number of particles on each image and using their size to estimate the particle cross-sectional area projection on the wafer. A typical AFM example is shown in Fig. 6.6. Although the AFM cannot accurately measure the lateral

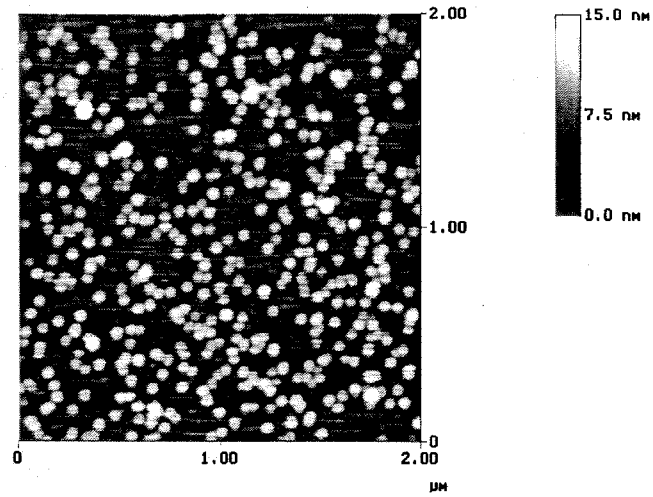

Figure 6.6: AFM image of silicon nanoparticles deposited onto a 200 mm wafer. These image were used to obtain density profile estimates across the wafer surface.

dimensions of the particles, the particle heights are accurate representations of the particle diameter, enabling measurement of the particle size and, thus, a calculation of the particle density as a function of radial wafer position.

From the AFM experiment, the main observation of changing collection times was rather intuitive: doubling the deposition time roughly doubled the nanoparticle density and doubled the total number of deposited particles. Surprisingly, only small deviations were detected in changing the aerosol inlet velocity and the temperature of the top plate of the deposition chamber. The gap spacing, however, does alter the particle deposition profile.

Since aerosol particle concentrations were measured with the electrometer and correlated to the deposited particle density and total deposition time, the collection efficiency of the deposition chamber could be obtained. The deposition collection efficiency, η_{eff}, is defined the percent ratio of the number of particles deposited over the number of particles entering the deposition chamber. The η_{eff} was verified by attaching an aerosol neutralizer and electrometer to the exit of the deposition chamber and counting particles that were not deposited on the wafers. Admittedly, the large volume of the tubing could have reduced the particle concentrations detected. Regardless of the inlet velocity and total deposition time, the η_{eff} for $\Delta T \sim 150^{o}C$ (top plate temperature - wafer temperature) ~ 80 to 85%, and $\Delta T \sim 100^{o}C$ gave η_{eff} ~ 70 to 75%. The ΔT was partially controlled by the top plate temperature, but more commonly controlled by changing the wafer position within the deposition chamber.

The temperature of the wafer can be calculated from a simple expression

$$T_w = \frac{q_1 T_2 + q_2 T_1}{q_1 + q_2} \tag{6.2}$$

where T_w is the temperature of the wafer, T_1 is the temperature of the top plate, T_2 is the temperature of the water-cooled disk, q_1 is the gap spacing between the top plate and the wafer, and q_2 is the gap spacing between the wafer and the water-cooled disk. In this approximation, the width and thermal conductivity of the wafer is assumed to be negligible. Thus, by changing the gap size, not only are the deposition densities changed, but the wafer temperature is different, changing the temperature gradient within the deposition chamber.

By controlling these variables, it was possible to deposit reasonably controlled and known particle densities along the wafer radius. This is extremely useful in the next chapter where particular particle densities must be consistently and reproducibly deposited on many wafers. Regardless of the variables changed, the particle density along the outer edges of the wafer was always more uniform and lower density and, thus, more accurately measured because the AFM measurements were able to distinguish adjacent particles more clearly and three-dimensional particles structures were rarely observed (unlike in towards the center). Therefore, the outer particle density values were used to determine the total deposition time required to reach a specific particle density on the outer wafer edges. Total deposition times were calculated from

$$t_d = \frac{t_m \times [part]_m \times \rho_m}{[part]_d \times \rho_d} \tag{6.3}$$

where t is the collection time, [part] is the particle concentration measured by the RDMA, and ρ is the particle density on the outer edges of the wafer. The subscript m refers to measured values from the wafers and subscript d refers to the wafer sample to be prepared. Since the aerosol particle concentration was relatively stable over time, this equation simplified to

$$t_d = \frac{t_m \times \rho_m}{\rho_d} \tag{6.4}$$

The estimated radial particle density profiles calculated from the experimental AFM images for each of the ten samples are shown in Fig. 6.7 together with the model predictions for the particle density profiles. In general, the outer edges of the wafer show very uniform particle deposits as the model predicts. Toward the center of the wafer, a large increase in the particle density is observed, again, a trend reflected in the model. The wafer center had the highest concentration of particle deposits since particles are depositing because of stagnation flow.

Currently, the nonuniform nanoparticle densities collected on each wafer are tremendously advantageous. With a single silicon wafer, we can produce devices with nanoparticle densities ranging over two orders of magnitude depending upon the device location on the wafer. For each individual device, though, their small size allows us to consider them to have a uniform density of nanoparticles along the entire channel length and width. Thus, we do not need to prepare separate wafer samples to determine the

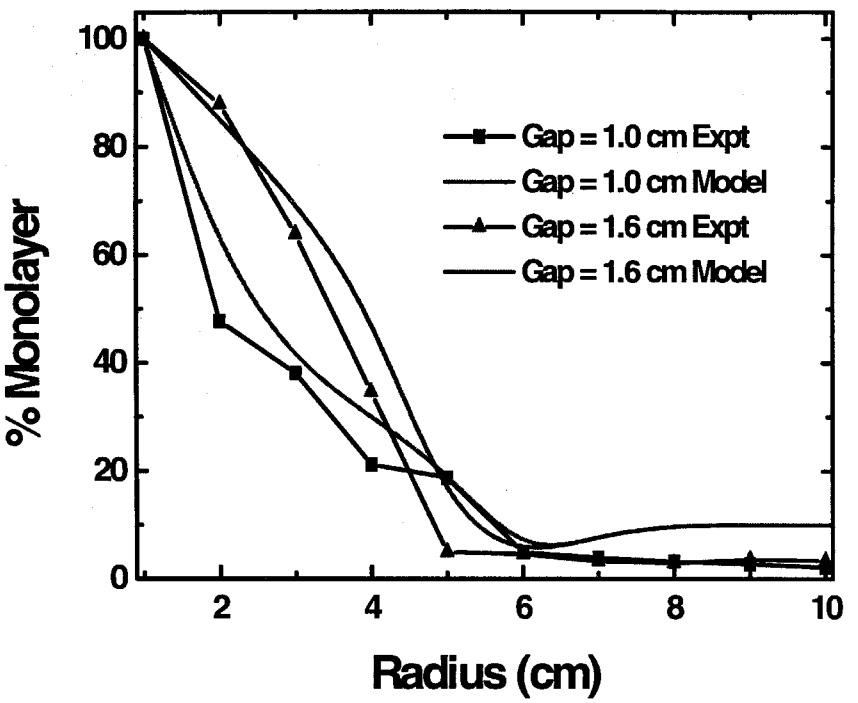

Figure 6.7: Nanoparticle density profiles measured as a function of radial position on 200 mm wafers.

effect of particle density on memory performance. All density effects can be probed on the same wafer simply by moving to a device with a different radial position. However, once nanoparticle density effects on memory performance are known, future devices will require uniform particle densities over the entire wafer surface. Thus, a new deposition chamber will then be required. The existing model will facilitate the design improvements that will need to be made to this deposition chamber.

6.7 Summary

We have designed an ultra clean two-stage aerosol process reactor and 200 mm wafer deposition chamber that is currently being used to integrate Si/SiO_2 nanoparticles into memory devices. Silicon nanoparticles are synthesized by thermal decomposition of silane gas and are passivated with thermal oxide. This two-stage aerosol reactor has been successfully integrated with a 200 mm silicon wafer deposition chamber that is contained within a class 100 cleanroom. This entire reactor system conforms to rigorous cleanliness specifications such that we can control the contamination of transition metals to levels below or close to 10^{10} atoms cm^{-2} while still obtaining particle deposition densities of 10^{12} particles cm^{-2}. The deposition chamber has been designed to produce a controllable particle density profile along a 200 mm wafer where particles are thermophoretically deposited uniformly over three-quarters of the wafer area. Thus, we now have the capability to deposit controlled densities of oxide-passivated silicon nanoparticles onto 200 mm silicon wafers for production of silicon nanoparticle memory devices.

Improvements for the future include designing a deposition chamber that produces uniform deposits over the entire wafer surface. Once current memory devices have been experimentally tested and analyzed, appropriate nanoparticle densities for optimal memory performance will be known. The deposition chamber flow model of which the accuracy has been experimentally verified will be used to identify suitable reactor designs. At that point, nanoparticle wafers will be produced that have constant and optimal nanoparticle densities over the entire wafer. We also eventually plan to add an ultra clean differential mobility analyzer to size classify the particles prior to deposition to improve control over the particle size distribution beyond that attained with the present ultra clean reactor.

Chapter 7: Silicon Nanoparticle Device Fabrication and Structural Characterization

7.1 Introduction

The work discussed in the preceding chapters laid the groundwork for fabrication of state-of-the-art aerosol silicon nanoparticle floating gate devices on 200 mm wafers in collaboration with the microelectronics division of Lucent Technologies/Bell Laboratories (Lucent). After certifying that the contamination levels in the ultra clean two-stage aerosol reactor and deposition chamber were sufficiently low, a free exchange of wafers and cleanroom supplies between Lucent and Caltech was established. Lucent assumed responsibility for designing the masks and transistors and for fabricating all device features, except for the aerosol-deposited floating gates in 29 device and monitor wafers. The wafers processed with silicon rich oxide (SRO) and direct growth (DG) floating gates were fabricated entirely at Lucent. They were only handled at Caltech after they were completed.

To date, two wafer lots have been processed at Caltech in collaboration with Lucent. The first wafer lot split described in Tables 7.1 and 7.2 consists of monitor (MON) and device wafers. The tables describe the physical dimensions of the different oxide layers and the floating gate fabrication method.

1	A	B			C	D	E			F	G
1	2	3	4	5	6	7	8	9	10	11	12
Tub implants											
15A	Tunnel oxide: 40A				Tunnel oxide: 50A						
AE3		**AE1**	**AE2**	**AE3**		DG1	**AE1**	**AE2**	**AE3**	SRO1	SRO2
12		12				12					

Table 7.1: Monitor wafer lot overview. Critical features of the wafers are listed, including tunnel oxide thickness, floating gate fabrication technique, and high temperature oxide thickness.

1				A				B		C						D		E				F	
1	2	3	4	5	6	7	8	9	10	11	12	13	14	15	16	17	18	19	20	21	22	23	24
Tub implants																							
Tox: 40A				Tunnel oxide: 50A														Tox: 70A					
AE1		**AE2**		DG1		DG2		DG3		**AE1**		**AE2**		**AE3**		SRO1		DG1		DG2		SRO1	
8	12	8	12	8	12	8	12	8	12	12	16	12	16	8	12	8	12	12	16	12	16	12	16

Table 7.2: Device lot overview: Critical features of the wafers are listed, including tunnel oxide thickness, floating gate fabrication technique, and high temperature oxide thickness.

In the aerosol floating gate devices, the nanoparticle core diameter and the oxide passivation layer thickness were varied. Furthermore, some aerosol silicon nanoparticles were processed without a thermal oxide passivation layer, but, nevertheless, possess a native oxide due to the unavoidable, prolonged exposure of these deposited nanoparticles to ambient, cleanroom air during shipping back to Lucent for complete processing.

Three aerosol nanoparticle wafer batches were produced at Caltech in the first wafer lot split: AE1 wafers contain an 8 nm crystalline core with 2 nm thermal oxide passivation layer, AE2 wafers contain a 3 - 4 nm crystalline core with 1.5 nm thermal oxide passivation layer, and AE3 wafers contain an 8 nm crystalline core but no thermal oxide passivation layer. The SRO is the synthesis of silicon nanoparticles by depositing silicon rich oxide onto the tunnel oxide, followed by an anneal to crystallize the silicon nanoparticles. DG is the abbreviation used to describe the direct chemical vapor deposition of silicon nanoparticles onto the tunnel oxide by nucleation of silicon islands from the gas phase and growth of these islands to form nanoparticle structures. The DG dose changes the nanoparticle size and density.

The wafers from the first wafer lot that demonstrated the best electrical behavior formed the basis set for the second wafer lot. This second device lot split is detailed in Table 7.3. DG and AE1 were the selected floating gate materials due to the electrical results of the aerosol wafers that will be discussed in Chapter 8 and the ambiguous (and unexpected) results of the DG wafers that needed more work to gain a full understanding of the device behavior. No SRO wafers were produced in the second lot. Additionally, Caltech selected the floating gate structures of four wafers to contain floating gate layers

1				A				B				C				D			
1	2	3	4	5	6	7	8	9	10	11	12	13	14	15	16	17	18	19	20
T1	T2	T1	T2	T1	T2	T1	T2	T1	T2	T1	T2	T1	T2	T1	T2	T1	T2	T1	T2
Tunnel Oxide: 4nm																			
AE1								Caltech				DG1							
8		10		8		10		8				8		10		8		10	

Table 7.3: Device lot overview: Critical features of the wafers are listed, including tunnel oxide thickness, floating gate fabrication technique, and high temperature oxide thickness. Those wafers specified with the Caltech designation have floating gates defined by Caltech as being of scientific interest. Gray background indicates Al_2O_3 instead of SiO_2.

of scientific interest to Caltech. The gray boxes also signify the wafers that incorporate Al_2O_3 as the gate oxide instead of SiO_2.

7.2 Monitor Wafers

Both monitor (MON) and device wafers were processed into nanoparticle structures. MON wafers were dedicated primarily to Caltech characterization and for Caltech purposes. These wafers were not destined to become full-scale devices, but rather structures that contained aerosol silicon nanoparticles embedded between high-quality thermally grown tunnel oxide and TEOS deposited high temperature SiO_2 (HTO). Transmission electron microscopy (TEM) studies of the nanoparticles layers were performed on the MON wafers. These studies focused on the adhesion between the HTO and the nanoparticle layer, the conformation of the film that was deposited onto discrete nanoparticles, and especially when the film layer thickness approaches the diameter of the deposited nanoparticles, and when the nanoparticle density was sufficiently high to produce three-dimensional formations of nanoparticles. The MON wafers were also used to verify the dimensions of the thermal oxide and HTO layers processed by Lucent to insure that their processing facilities were performing as expected. A few MON wafers were used by Lucent to develop specific process and etch steps unique to processing the nanoparticle layer in order to ensure that complete etching through the nanoparticle layer in locations where nanoparticles are not desired actually occurs. These wafers were sacrificed in these process development experiments.

To produce these MON wafer structures, Lucent first grew high quality thermal oxides on the wafers at specific dimensions described in Table 7.1. These wafers were then sealed into 200 mm wafer cleanroom boxes in a class 100 mini environment and were shipped overnight to Caltech. Once the floating gate was deposited at Caltech as described in Table 7.1, the MON wafers were sent back to Lucent in a class 100 mini environment. Lucent then deposited the final structure, the HTO layer which served to embed the silicon nanoparticles in oxide. MON wafers were completed in ~ 2 to 3 weeks.

These MON wafers provide virtually unlimited samples for AFM charging experiment and for capacitance experiments designed to probe the behavior of the nanoparticle floating gate without interference from device structures, such as the gate stack and the substrate implant regions. For added convenience, the nanoparticle floating gate layers in these MON wafers (in addition to the tunnel oxide and HTO layer dimensions) are identical to the corresponding nanoparticle floating gates on the device wafers. Thus, MON wafers can be used to probe the charging and discharging behavior of the nanoparticle floating gate layer with unique characterization techniques, and these results can be correlated with device and electrical measurements made on the corresponding location on device wafers.

7.3 Device Wafers

Device wafers listed in Table 7.2 were initially processed at Lucent. To build the

silicon nanoparticle floating gate devices on device wafers, Lucent initially processed the silicon wafers by performing tub implantation and thermal oxidation to produce a uniform high-quality SiO_2 tunnel oxide on the wafers with dimensions also listed in Table 7.2. These wafers were then sealed into 200 mm wafer cleanroom boxes in a class 100 mini environment and were shipped overnight to Caltech. Once the floating gate was deposited at Caltech, the device wafers were sent back to Lucent in a class 100 mini environment to complete the device processing. The entire process took ~ 4 - 6 months to complete the device wafers.

7.4 Aerosol Nanoparticle Floating Gate Layers

In depositing the aerosol nanoparticle floating gate, careful steps were taken to insure that the deposited layer was as carefully controlled as possible and that the characteristics of that deposited layer were known and well documented and that they were consistent for both the MON and device wafers. Of particular interest in the aerosol nanoparticle floating gate layer was the size distribution of the nanoparticles and the approximate radial density of the nanoparticles. For this reason, before and after each aerosol wafer was processed, a size distribution was recorded. The total collection time was also measured. The size distribution was measured both before and after wafer samples were processed to detect any drift in particle properties that might occur during collection. For each wafer sample, the aerosol nanoparticle size distribution is known. From the total collection time and particles concentrations also recorded, the radial

nanoparticle density could be calculated.

Typical size distributions of the AE1, AE2, and AE3 sample designations are shown in Fig. 7.1. For all wafers, before and after size distributions were measured. Since wafers were made immediately after each other, the size distribution measured after one wafer corresponds to the size distribution measured before the next wafer. In general, the silicon nanoparticle source was extremely stable over time, no large fluctuations were observed. This stability was even present after replacing empty nitrogen cylinders, since the silane valve was not touched and nitrogen flow rates were not changed. For all MON and device wafers, approximately 40% nanoparticle density was desired on the uniform outer edges of the wafers. Using the methods described in Chapter 6, these densities were fairly easy to obtain and reproduce from wafer to wafer.

7.5 Structural Characterization

Extensive structural characterization of completed MON wafers and device structures in device wafers has been performed using optical microscopy, AFM, and TEM. Before the comparisons between MON and device wafers are made, basic structural characterization of the tunnel oxide layer, the nanoparticle layer, and the HTO deposited layer on the MON wafers will be discussed. Of major concern in the fabrication of the aerosol nanoparticle floating gate memories is the characterization of the deposited HTO layer. We need to understand the adhesion of the deposited HTO

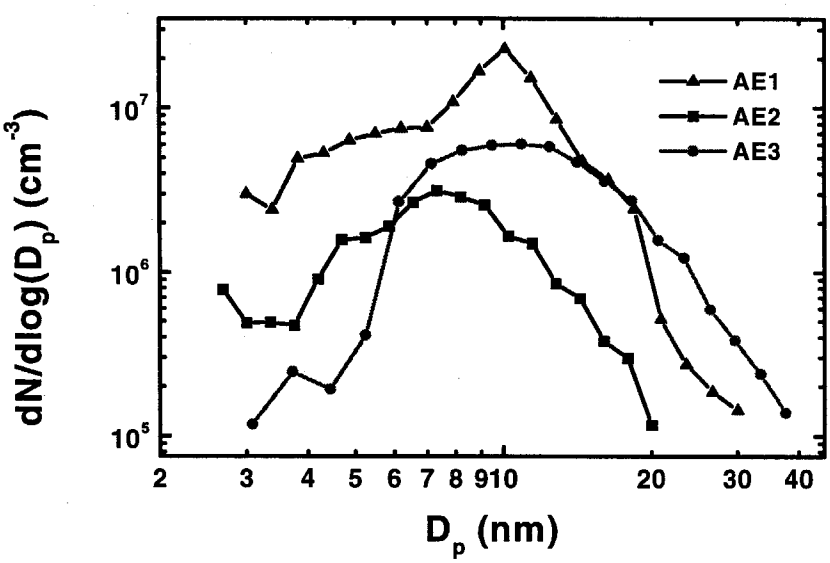

Figure 7.1: Typical aerosol size distributions for AE1, AE2, and AE3 deposited nanoparticle layers.

layer to the nanoparticle layer and to the thermally grown SiO_2 film, conformational deposition of the HTO film for layers containing both large and small nanoparticles and both high and low particle density deposits. Does film deposit conformally around the particles, or does it have layers that are flat regardless of the topography of the nanoparticle layer? Does the HTO to fill in all spaces between adjacent particles and between particles and substrate or will void volumes exist around the nanoparticles? Does the HTO deposition process consume enough silicon to oxidize the deposited nanoparticles completely? Are the temperatures and gas velocities used in the HTO deposition process sufficient to remove nanoparticles from the wafer before the HTO can be completely deposited? Could three-dimensional piling of nanoparticles short the gate and channel, e.g., if a chain of nanoparticles extends across the entire oxide layer to cause device failure?

Finally, structural characterization of the MON wafers will be used to examine the nanoparticle layer and to compare the different layers formed by SRO, DG, and aerosol methods. Of particular concern is the verification of crystalline material to probe whether or not the subsequent HTO deposition was sufficient to oxidize the particles. Floating gate characterization also probes nanoparticle size and density to compare the three methods for silicon floating gate fabrication and to determine the effect of nanoparticle density on the subsequent device layer processing and performance.

7.6 Tunnel Oxide Characterization

7.6.1 TEM

TEM characterization of the tunnel oxide layer has been done to measure the thickness of the oxide layer to compare directly to the anticipated tunnel oxide layer grown by Lucent and to examine the interface quality between the silicon and grown SiO_2 film. Comparison of the three thickness of tunnel oxide (3, 4, and 5 nm) described in Table 7.1 are in good agreement with the thicknesses measured with TEM and the Si/SiO_2 interface appears to be smooth. Thermal oxide characterizations indicate that Lucent has good control over the growth of high quality thermal oxide at thicknesses within ~ < 0.5 nm uniformly across the wafer.

7.6.2 AFM

AFM has been used to measure the surface topography of the tunnel oxide layer prior to nanoparticle deposition. AFM confirms that the thermal oxide is smooth at an atomic level as seen in Fig.7. 2. AFM measurements taken on various MON wafers at 1 cm intervals from the wafer edge toward the wafer center are shown in Table 7.4. These average roughness values indicate that the thermally grown oxide is consistently smooth on the atomic level, irregardless of the thermal oxide thickness or wafer location.

7.7 Nanoparticle Floating Gate Layer

7.7.1 SRO

Cross section TEM has been vital to the characterization of the floating gate

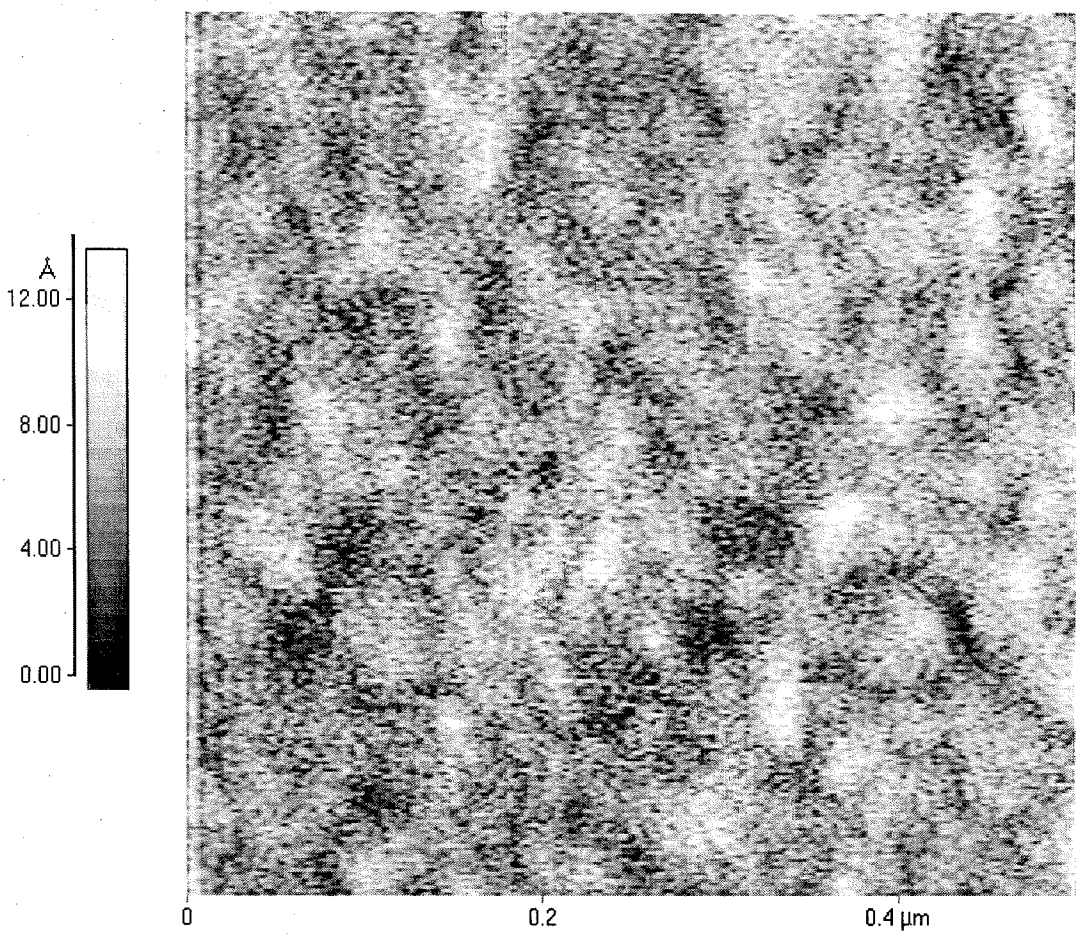

Figure 7.2: AFM of thermal oxide indicates that the tunnel oxide is smooth on the atomic level across the entire wafer.

material in all three floating gate fabrication methods (i.e., SRO, DG, aerosol). The most ambiguous floating gate devices are the SRO wafers. The TEM indicates that the oxide layers do contain excess silicon as seen in density variations within the oxide approximately located where the silicon floating gate is expected to be present. However, high resolution imaging of these nanoparticles has not been possible, mostly because the material in the floating gate interacts with the TEM high energy electron beam. This interaction creates a shimmer or moving image that is very difficult to capture on a photograph, especially if silicon crystalline lattice fringes are required to verify silicon nanoparticle presence. Furthermore, TEM does not indicate any remarkable difference between non annealed and annealed SRO samples, an unexpected and unexplained observation. In the annealed SRO sample, nanocrystalline silicon particles should be seen. However, of the floating gate structures produced in this thesis, the SRO floating gate material is of least interest, mainly because the floating gate layer is not nearly as novel as is the aerosol deposited nanoparticle floating gate.

7.7.2 DG

TEM has also been used to examine the floating gate fabricated by direct silicon CVD onto the tunnel oxide, or DG as it is referred to in this thesis. In these wafers, the floating gate has been examined both as cross-section and as planar samples. The cross section TEM samples provide both partial information on the density of the nanoparticle layer and on the layer depositions following nanoparticle growth. In the DG cross section shown in Fig. 7.3, the HTO layer, in addition to the gate layers (poly silicon

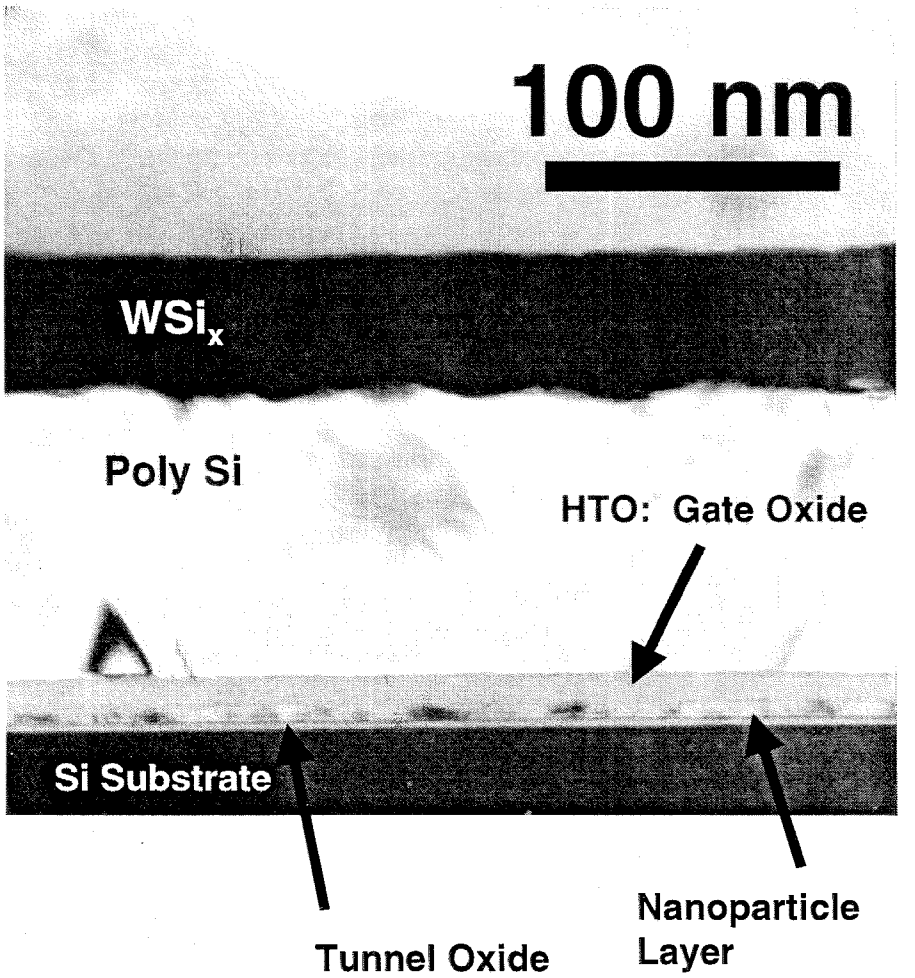

Figure 7.3: Cross section TEM of DG device layers.

and WSi_x) appear to be relatively flat, indicating that the nanoparticle layer has not disrupted normal transistor processing. Furthermore, the floating gate appears to be ~6 nm in height and high resolution TEM shows crystalline material. The floating gate does show high crystalline density, so one main issue of interest that a planar view TEM sample can begin to address is whether or not the floating gate material in the DG samples is comprised of nanometer-sized interconnected silicon islands or if it is truly discontinuous as originally envisioned.

Planar TEM samples were prepared by careful, tedious removal of the underlying silicon substrate with hydrofluoric acid (HF). Approximately 3mm diameter wafer samples were glued face down onto the front side of TEM slot grids. Etching progress was continuously monitored with light microscopy. HF was added to the sample with the tip of a toothpick until a reddish-orange color could be seen through the sample. The etching was promptly stopped by dipping the entire grid and sample into water. Images were taken in these chemically thinned regions.

Planar view high resolution TEM shows a high coverage of crystalline silicon lattice fringes, often forming meandering islands that span several 10s of nanometers. However, not all possible crystallographic orientations are observed in high resolution TEM. Since DG is known to produce silicon crystallites of preferred orientations on surfaces, the degree of continuity of the floating gate remains unknown.

7.7.3 Aerosol

Of most interest to this thesis is the structural characterization of the

aerosol-deposited silicon nanoparticle floating gate, including AE1, AE2, and AE3 deposited layers. Several important conclusions can be made about this nanoparticle layer as well as the subsequent layers deposited upon the aerosol nanoparticle floating gate. Fig. 7.4a and 7.4b shows the two ends of a guard transistor. The nanoparticle layer can be seen as dark contrast regions embedded within the oxide layers. These images are particularly useful in that they demonstrate that the nanoparticle layer was successfully etched in regions not under gates, but protected under the gates.

High resolution images of the aerosol deposited nanoparticle floating gate have been obtained for the AE2 wafers. Silicon crystalline lattice fringes can be seen in the floating gate and are separated from the channel by ~ 5.5 nm of SiO_2 tunnel oxide in Fig. 7.5. Due to resolution issues related to particle crystallographic orientation, only about 10% of the nanoparticles in the floating gate can be seen as high resolution (only 10% of nanoparticles have a crystallographic orientation suitable for viewing lattice fringes at any given orientation). The presence of crystalline nanoparticles verifies both that crystalline silicon was deposited as expected, and that the aerosol nanoparticles remain crystalline during HTO deposition. At higher nanoparticle densities, crystalline particles can also be seen deposited on each other, bridging the gap between the floating gate and the control gate, producing defects in the device and shorts between the floating gate and the device gate.

As briefly discussed in the DG samples, planar TEM samples have also been prepared from these aerosol device wafers. By etching with all layers except for the silicon nanoparticle floating gate layer and the tunnel oxide and HTO layers, a sufficiently

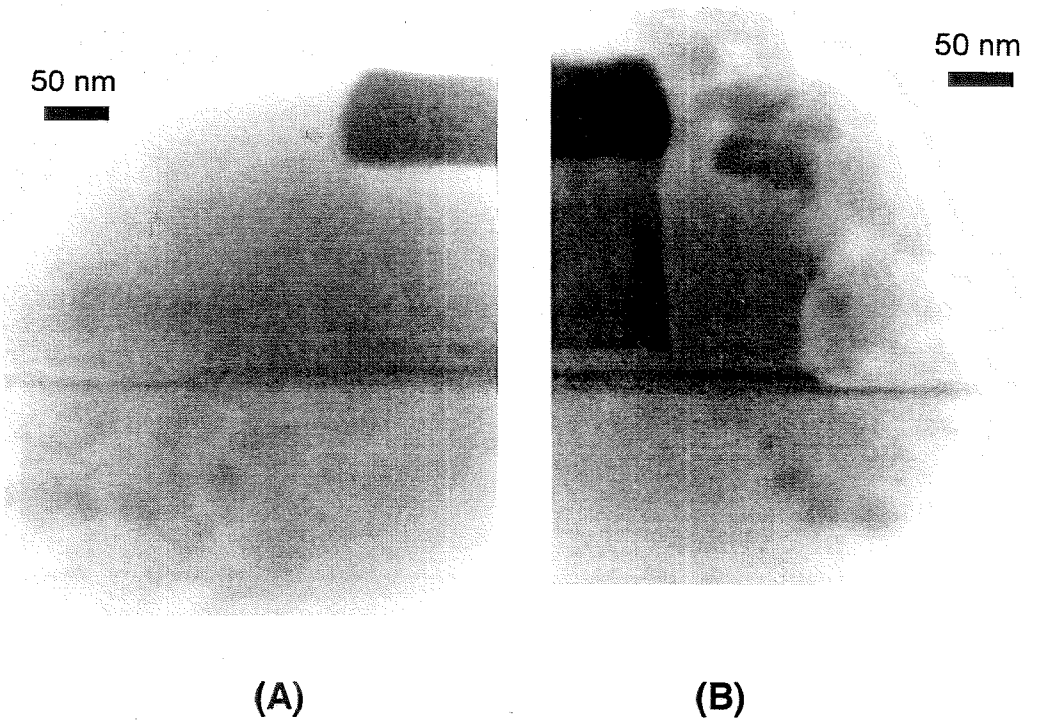

Figure 7.4: Two ends of a guard transistor on an AE1 wafer.

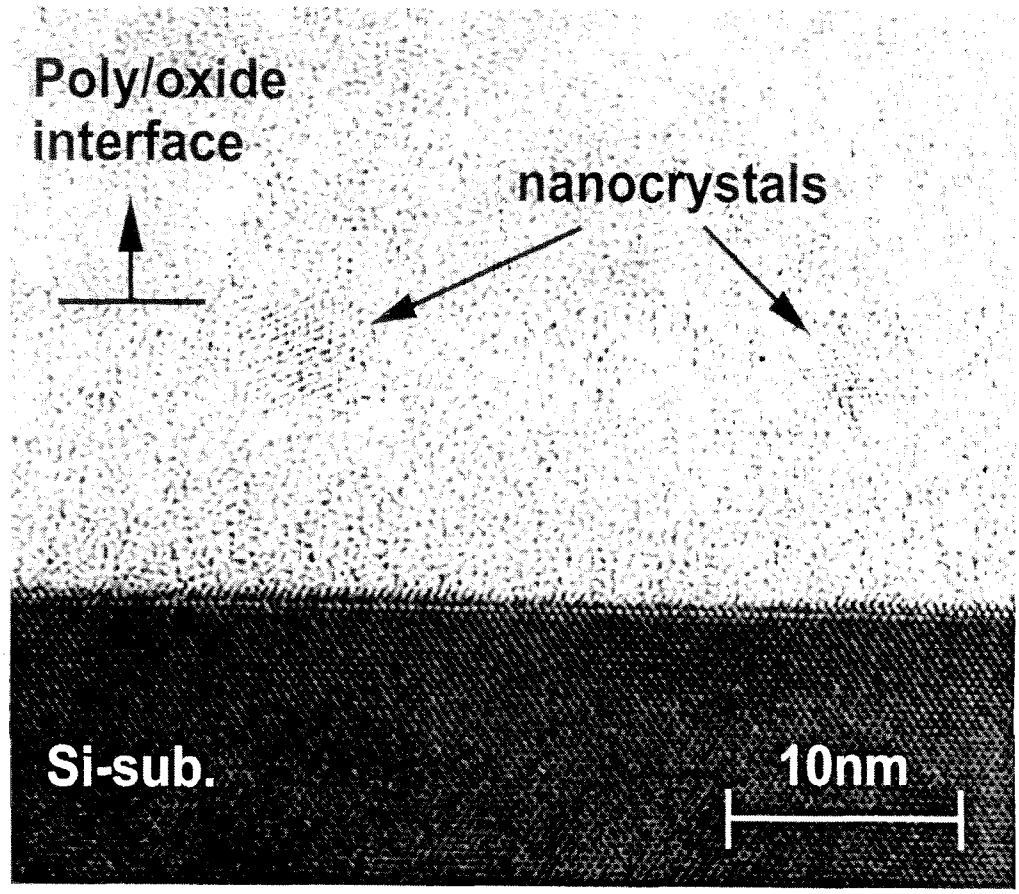

Figure 7.5: High resolution TEM of aerosol nanoparticle floating gate device layer.

thin, electron transparent sample can be produced. The TEM is then used to measure the nanoparticle density as actually deposited on the device wafers and provides an accurate way to verify the size distribution of the deposited aerosol particles. As seen in the planar TEM in Fig. 7.6, the nanoparticles have a density of ~ 6 x 10^{12} particles cm^{-2} and mean diameter ~ 4 -5 nm, in good agreement with deposited nanoparticles at a location roughly 8 cm in from the edge of the wafer (where this sample was taken) and mean diameter ~ 4 -5 nm, consistent with the AE2 sample from which this planar view TEM sample was prepared. Furthermore, the absence of significant three-dimensional particle deposition is not observed, indicating that monolayer (or dense submonolayer) coverage can be achieved while simultaneously avoiding the undesirable three-dimensional particle deposits.

7.8 HTO Characterization

More so than the other floating gate materials discussed, the aerosol nanoparticle density is seen to affect the subsequent HTO deposition. Indeed, TEM of the aerosol nanoparticle sample taken from the outside edge of the wafer shows the HTO to be relatively flat. However, in towards the wafer center where nanoparticle density is highest, aerosol nanoparticles can be seen protruding from the HTO layer and several bumps can be seen in the HTO, presumably from the presence of larger nanoparticles buried within the HTO layers. The issue of HTO layer conformation appears not only to be strongly dependent upon nanoparticle density, but also upon nanoparticle size, as

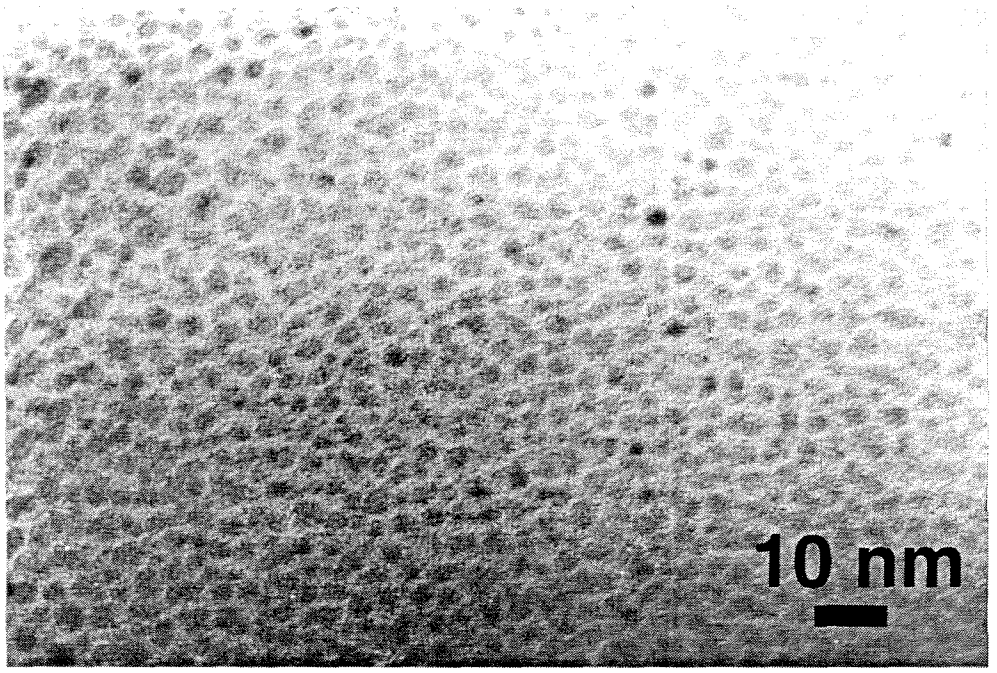

Figure 7.6: Planar TEM of aerosol nanoparticle floating gate layer.

expected. Larger aerosol nanoparticle floating gate (nanoparticle ~ HTO thickness) show the HTO to be more conformal, whereas the smaller nanoparticle samples (nanoparticle < HTO thickness) show more even, level HTO layers even at higher nanoparticle densities.

The conformality of the HTO has also been measured with AFM to understand the extent of HTO conformality issues. The topography of monitor wafers with larger nanoparticle and wafers with small nanoparticles were measured at 3 locations, 2 of which are shown in Fig. 7.7: (a) 1 cm from the wafer edge, halfway between the center and the edge, and (b) 1 cm from the wafer center. As seen in Table 7.4, the average roughness of the HTO layer increases toward the center and becomes more smooth out toward the wafer edge, a trend observed for both the large and small aerosol nanoparticle samples. Furthermore, the smaller nanoparticle sample had lower average roughness measurements compared with the larger nanoparticle wafers at the same corresponding location on the wafer. This indicates that when HTO thickness approach the aerosol nanoparticle diameter, conformation between the two layers becomes a more important issue. When the nanoparticle diameter is less than the HTO thickness, the relative effect of HTO conformation is less important.

To address the issues of HTO layer adhesion to the nanoparticle layer, cross-section TEM is an important tool. In isolated circumstances, the HTO layer was seen to peel away from the nanoparticle layer and the tunnel oxide layer. However, it is unknown as to whether or not this was caused by poor adhesion between layers or if this was a result of TEM cross section preparation. Due to aggressive polishing required to

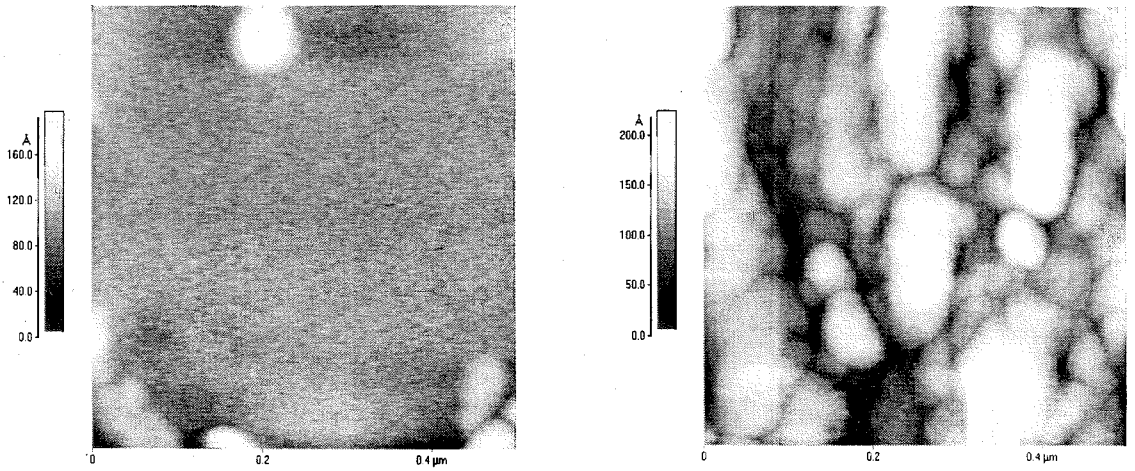

(A) **(B)**

Figure 7.7: AFM of HTO layer embedding aerosol nanoparticles in the **(A)** outer edges of the wafer, and **(B)** 1cm from the wafer center.

	Thermal Oxide	HTO with AE1	HTO with AE2
edge (a)	1.21A	3.39A	2.77A
(b)	1.56A	4.39A	3.04A
center (a)	1.22A	32.2A	20.5A
(b)	1.54A	39.7A	24.9A

Table 7.4: AFM measurements of surface roughness for tunnel oxide and HTO layers with and without aerosol nanoparticle deposits.

prepare cross section TEM samples, it is entirely feasible that sample preparation was responsible for the occasional peel-off conditions observed. Furthermore, the adhesion problem was never observed in device wafers, so it is entirely feasible that the peeling problem is a direct result of the sample thinning and polishing process required to prepare cross sectional TEM samples. Despite this controversy, the HTO layer peeling was fortuitous in TEM sample preparation because it did expose the nanoparticle layer to careful analysis. One such example exposed 3 - 6 nm aerosol silicon nanoparticles in the floating gate region, further verification of successful aerosol nanoparticles deposition in the floating gate region of particles within the expected size distribution of deposited nanoparticles in this particular AE2 sample.

7.9 Summary

The structural characterization of the aerosol wafers in particular shows several interesting features. At low nanoparticle densities, HTO layers appear to have good adhesion and the nanoparticle layers do not produce significant conformational layers in the HTO, especially for small nanoparticle samples. At high nanoparticle densities, the HTO becomes considerably rougher, a result seen in both TEM of SiO_2 bumps in the HTO and in AFM measurements of the increased HTO surface roughness. Despite these limitations, all indications point to the successful deposition of crystalline, single particle, spherical nanoparticles onto the tunnel oxide of devices that have dimensions expected from the size distributions measurements taken of the aerosol prior to and following

aerosol nanoparticle floating gate deposition. The electrical characterization of the aerosol nanoparticle devices will be discussed in Chapter 8, along with brief descriptions of the electrical measurements taken from the SRO and DG samples.

Chapter 8: Device Electrical Characterization and Modeling of Nanoparticle Floating Gate Electrostatics

8.1 Introduction

As described in the previous chapter, several methods have been used to fabricate the discontinuous floating gate devices. The structural characterization of the floating gate devices fabricated by the different methods was discussed in Chapter 7. This chapter discusses the electrical characterization of devices fabricated using the three different floating gate fabrication routes. The electrical measurements were performed at Lucent using an Alessi probe station and proprietary Lucent software. Devices with channel lengths from 0.18 μm to 10 μm were characterized. Since 0.18 to 0.20 μm devices represent the present "state-of-the-art" in device fabrication, we concentrate on these device lengths. Due to Lucent's present limitations on their 0.18 μm device processing, however, the reproducibility of manufacturing channel length of the 0.20 μm devices was considered to be better than manufacturing channel lengths for the 0.18 μm devices, so we focused on the 0.20 μm devices.

Transistor performance varied little with channel length, however the electrical behavior differed dramatically with nanoparticle floating gate fabrication technique. This chapter will discuss these performance differences and their correlation with nanoparticle

density (radial position of the measured device), nanoparticle size (AE1 vs. AE2), and nanoparticle oxide-passivation quality (AE1 vs. AE3). A few comments about the basic electrical characterization of the three types of nanoparticle fabrication methods will be discussed later in the chapter.

8.2 Electrical Measurements

8.2.1 Subthreshold and Output Characteristics

We probed basic transistor behavior by measuring the subthreshold characteristics (I_d vs. V_g) and the output characteristics (I_d vs. V_d) of the transistor, enabling us to verify that well-behaved and well-formed transistors have been fabricated. Good gate control over the conductance of the channel is essential to subsequent electrical measurements; both the subthreshold and output characteristics measure the control of the gate over the conductance of the underlying semiconductor channel.

8.2.2 Program and Erase Transients

Program and erase transients measure the ability of the devices to store charge on the floating gate, and thus, if they will function as memory devices. The program and erase transients measure program and erase voltages, program and erase times, and the magnitude of the threshold voltage swing between programmed and erased memory states. Furthermore, program and erase transients reveal the voltage-time trade-off relationship in these devices. Typically, increasing program and erase voltages reduces

program and erase times. On the other hand, high voltage power supplies are expensive, so longer program and erase times may be tolerated in order to reduce the program and erase voltages required.

8.2.3 Endurance

Ideally, these memory devices should be able to undergo at least 10^5 to 10^6 program/erase (P/E) cycles without window closure. Break-down of the oxide after repeated P/E cycles causes the program threshold voltage to decreases and the erase threshold voltage to increase. The resulting threshold voltage window collapse after repeated P/E cycles prevents accurate differentiation between the programmed and erased states. Endurance measurements also provide evidence of trapped charge build up in the oxide layers in the device.

8.2.4 Gate Disturb

Gate disturb measurements probe the behavior of the devices under normal read conditions. In many flash memory devices, the read voltage is sufficiently large to alter the threshold voltage of the device, leading to "soft" programming or "soft" erasing of the device. The gate disturb examines the extent of "soft" programming and erasing under a variety of applied gate voltages or read voltages. In an ideal device, no "soft" programming or erasing would occur under moderate read conditions. In actual devices, it is desirable that the threshold voltage shifts after "soft" programming and erasing be small compared to the threshold voltage window between programmed and erased states.

Then, even if fractional changes in the programmed and erased states occur under normal read conditions, the programmed and erased states would be clearly differentiated by the large threshold window, and gate disturb behavior is deemed acceptable.

8.2.5 Drain Disturb

Drain disturb measurements are used to probe the discontinuous nature of the nanoparticle floating gate layer by applying large biases to the drain node of the memory device. In a conventional floating gate memory cell where a continuous poly silicon layer stores the trapped charge, a moderately large bias to the drain node causes all charge to tunnel through the tunnel oxide at the drain side, completely erasing the memory. If the nanoparticle memories were truly discontinuous, then one would expect that application of a moderately large bias to the drain node would cause only those nanoparticles positioned above the drain node to discharge. Lateral conduction of charge stored in the nanoparticle layer should not occur if the nanoparticle floating gate structure is truly discontinuous, so the programmed threshold voltage should not change after applying a drain bias. Thus, the drain disturb measurement can demonstrate the discontinuity of the nanoparticle layer.

8.2.6 Retention

Retention measurements are similar to disturb measurements, except that all nodes in the device are grounded. The memory retention of the devices, both for programmed and erased states is necessary to demonstrate the volatility of the memory.

A nonvolatile memory (NVM) should lose only a fraction of the threshold voltage after many months or years.

8.3 SRO and DG Device Characteristics

All wafer types suffered junction leakage that was traced to a problem in the processing of the drain/source regions or in the aluminum contacts.

8.3.1 SRO Devices

In general, transistor behavior was acceptable for the SRO devices, although significant junction leakage between the source and drain regions with the substrate was observed. Program and erase transients indicated that these devices are capable of programming and erasing. However, the SRO nanoparticle fabrication technique is not considered to be novel, so little effort was made to perform complete electrical characterization. In general, their behavior mimicked the aerosol nanoparticle-deposited devices. At best, the electrical characterization of these devices is incomplete.

8.3.2 DG Devices

The direct growth device wafers proved to be highly problematic. These devices

exhibited unusual transistor subthreshold characteristics that are shown in Fig. 8.1. The saw-edge in the I_d vs. V_g was seen in all direct growth devices tested. The saw-edge could be partially caused by the device programming and erasing to traps located in the oxide (for example) at even low to moderate gate voltages that changed the I_d. vs. V_g characteristics. With this poor gate control over the devices, the program and erase transients were difficult to measure, leading to inconsistent results. These program and erase results were extremely irreproducible. For this reason and because the aerosol samples were the main focus of this thesis, no further electrical characterization of these devices was performed. Although the DG samples from the first wafer lot split are incapable of being electrically characterized, sufficient interest in DG samples remains, motivating the dedication of slightly less than half of the wafers from the second lot to be fabricated with a DG floating gate.

8.4 Aerosol Devices

Because the aerosol devices represent a major departure from conventional fabrication technology, and because these devices are the primary focus of this thesis, their electrical behavior will be discussed now in great depth. Electrical characterization of all three nanoparticle sample types (AE1, AE2, and AE3) will be discussed.

8.4.1 0.2 μm AE1 Device Characteristics

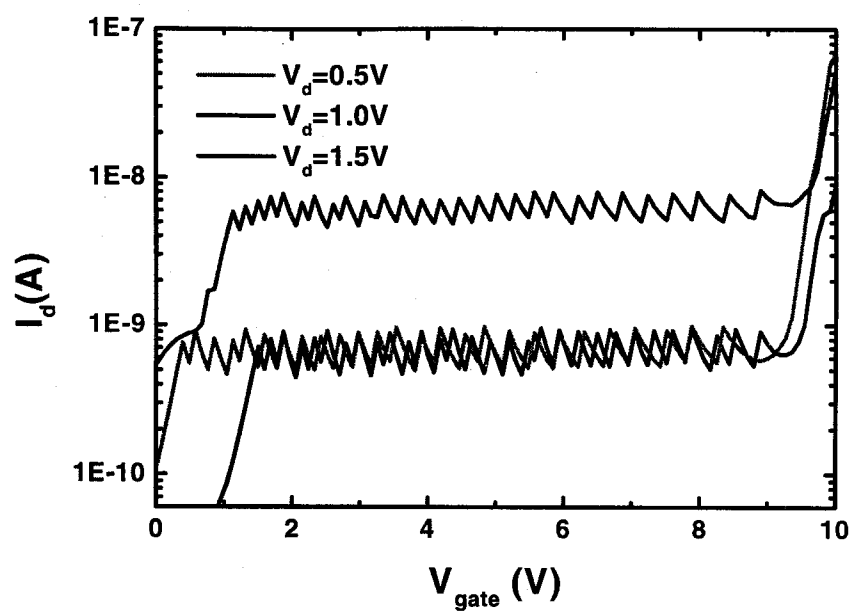

Figure 8.1: Subthreshold characteristics for DG device.

Typical subthreshold and output characteristics of 0.2 μm AE1 aerosol-nanoparticle MOSFETs are shown in Figs. 8.2a and 8.2b. The values of the drive current (30μA/μm), the substrate slope (200mV/dec), and the drain induced barrier leakage (DIBL) (100mV/V) are typical for thick gate dielectric, high substrate doped NVM devices. The threshold voltage, V_t, is defined as the gate voltage corresponding to a 1μA drain-source current when a 1 V drain bias is applied.

Uniform Fowler-Nordheim tunneling is used to program and erase the memory, although programming with channel hot-electron injection is also possible. As shown in Fig. 8.3a and 8.3b, the high areal nanoparticle density obtained by the aerosol fabrication process results in a large threshold voltage window (> 3 V), larger than those previously reported on nanoparticle devices[1],[2],[3]. This large V_t window results in a high read-out current (20 μA/μm for gate and drain biases of 2.5 V and 1 V, respectively), allowing fast memory access. The transient characteristics illustrate the voltage/performance trade-off for this device; higher voltages result in faster program and erase times. Despite the low gate coupling ratio inherent to nanoparticle memories, microsecond programming and millisecond erasure are possible at moderate operating voltages.

As shown in Fig. 8.4, the aerosol devices demonstrate excellent endurance behavior with only a small window closure observed after $5x10^5$ P/E cycles. The gradual shift of the V_t window to higher threshold voltages indicates charge build-up in the gate oxide layer during cycling. This charge build-up is reversible and can be removed by imposing higher erase voltages across the device. As seen in Fig. 8.4, one program

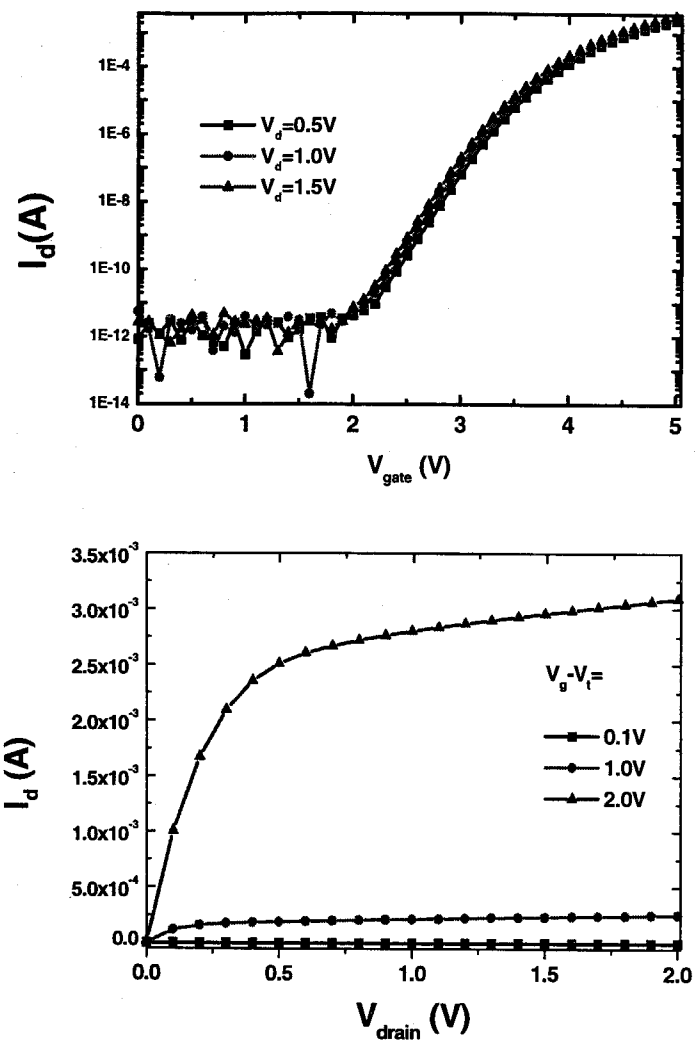

Figure 8.2: **(A)** Subthreshold characteristics and **(B)** output characteristics of 0.2 μm AE1 aerosol nanoparticle MOSFET.

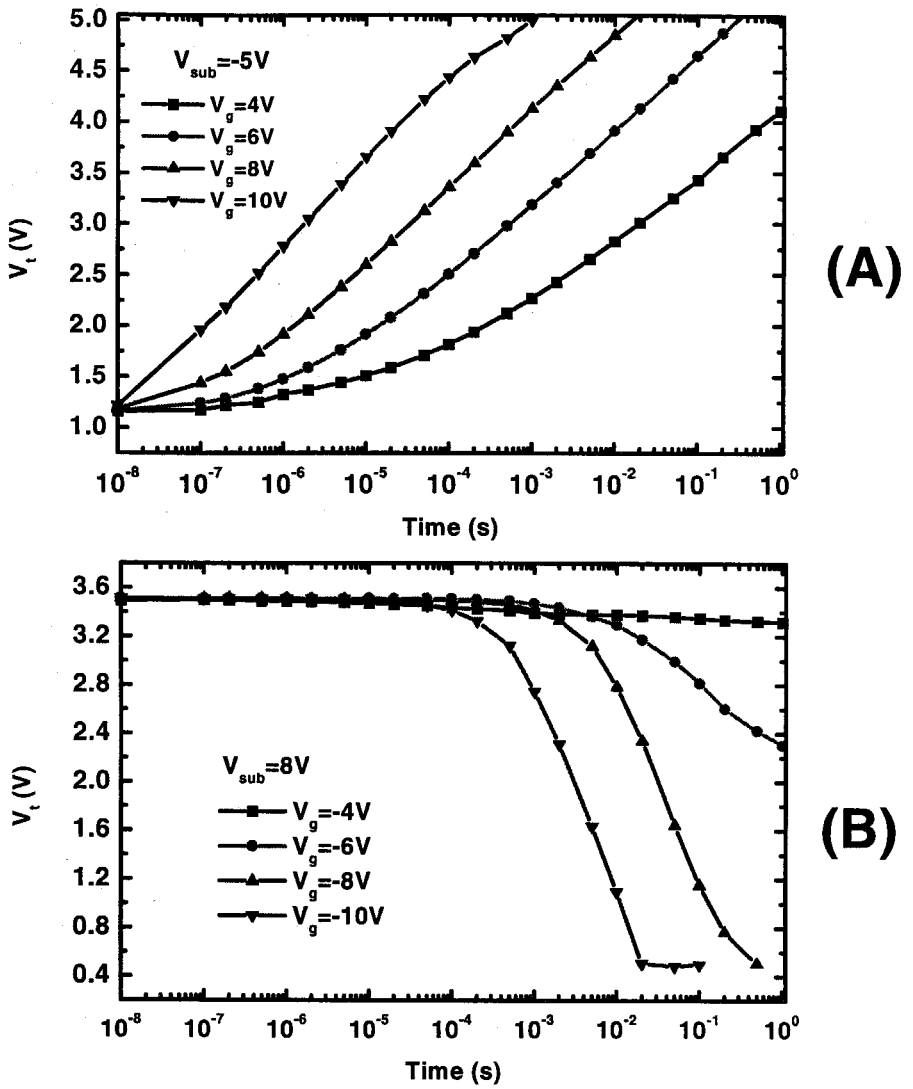

Figure 8.3: **(A)** Program transients and **(B)** erase transients for 0.2 μm AE1 aerosol nanoparticle MOSFET.

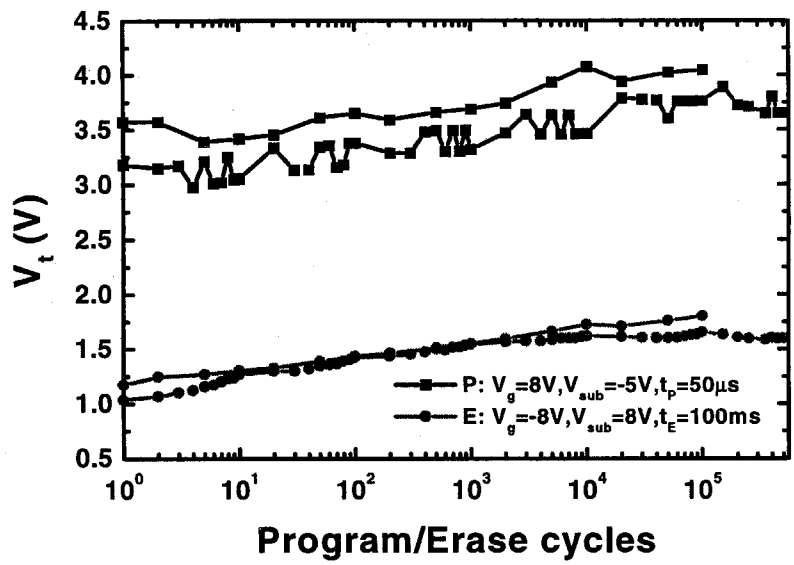

Figure 8.4: Endurance characteristics for 0.2 μm AE1 aerosol nanoparticle MOSFET.

endurance curve exhibits some small fluctuations. Although the reason for this is not completely understood, it could be that more frequent measurements and perturbations to the device may be causing traps to program and erase.

Disturb and retention data after program/erase cycling is presented in Fig. 8.5. In spite of the thin tunnel oxide, reasonable disturb times and long nonvolatility are obtained, indicative of the intrinsic advantages of discrete nanoparticle charge storage. However, further gate dielectric stack optimization is necessary to claim true nonvolatile behavior. No stress induced leakage current (SILC) was observed, nor was any drain disturb detected, even at drain voltages as high as 4V. This observation indicates that there is little or no lateral conduction in the nanoparticle layer. In Fig. 8.6, the effect of tunnel oxide thickness on memory retention can be seen for AE1 devices. The 5 nm tunnel oxide has better retention than the 4 nm tunnel oxide. However, both are acceptable since the loss of data is small compared to the program and erase window that is found in these devices.

8.4.2 0.2 μm AE2 Device Characteristics

Subthreshold and output characteristics of the 0.2 μm AE2 aerosol-nanoparticle MOSFETs are shown in Figs. 8.7a and 8.7b. The values of the substrate slope (240mV/dec) and the DIBL (100mV/V) are, again, typical for thick gate dielectric, high substrate doped NVM devices.

Uniform Fowler-Nordheim tunneling is used to program and erase these devices.

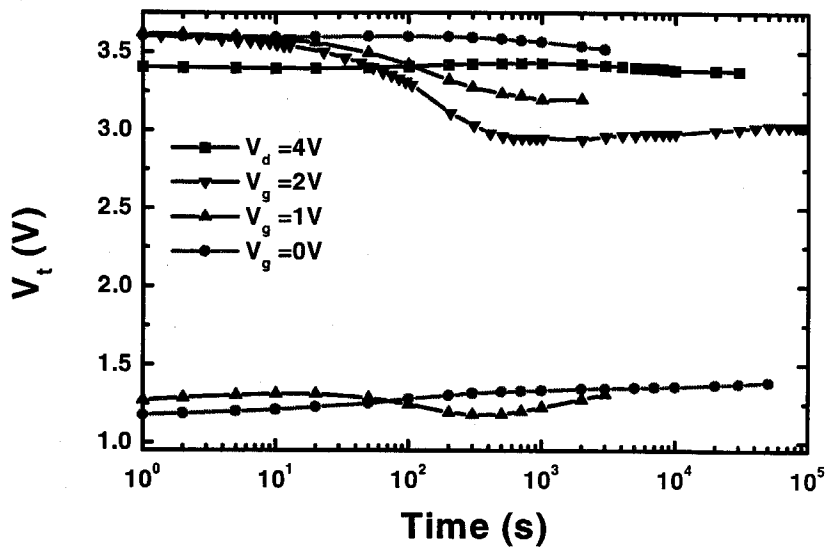

Figure 8.5: Gate and drain disturb characteristics for 0.2 μm AE1 aerosol nanoparticle MOSFET.

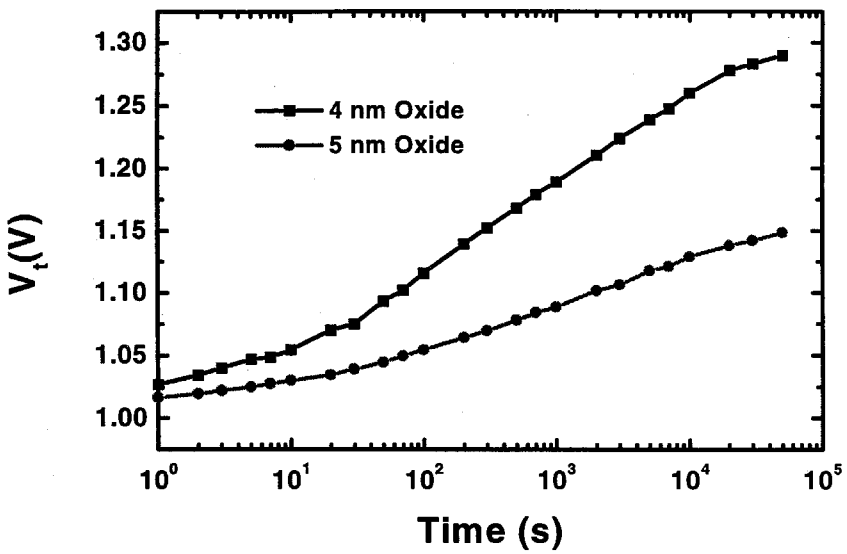

Figure 8.6: Retention characteristics for AE1 sample with different tunnel oxide thicknesses.

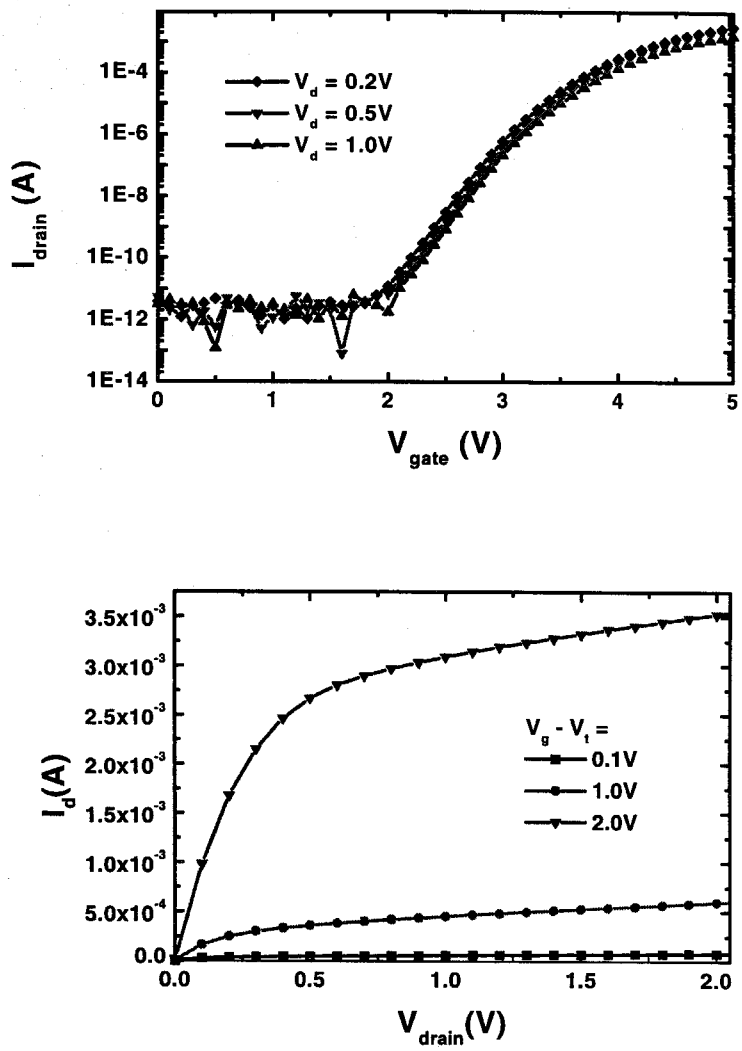

Figure 8.7: **(A)** Subthreshold characteristics and **(B)** output characteristics of 0.2 μm AE2 aerosol nanoparticle MOSFET.

As shown in Fig. 8.8a and 8.8b, the aerosol fabrication process results, again, in a large threshold voltage window (> 3 V). The transient characteristics illustrate the voltage/performance trade-off for this device; higher voltages result in faster program and erase times. Microsecond programming and millisecond erasure are possible at moderate operating voltages. As shown in Fig. 8.9, the aerosol devices demonstrate excellent endurance behavior with only a small window closure observed after $2x10^5$ P/E cycles. Again, charge accumulates in the gate oxide layer during cycling. This charge build-up is reversible and can be removed by imposing higher erase voltages across the device.

Disturb and retention data after program/erase cycling is presented in Fig. 8.10. The main failure of these AE2 devices is seen in the gate disturb characteristics. The gate disturb measurements indicate that charge is actually being injected into and from the floating gate via the HTO layer, not the tunnel oxide. Although the other electrical measurements indicate that the AE2 devices are performing well, the disturb measurements indicate that the quality of the HTO layer need to be improved. These experimental observations lead to the integration of Al_2O_3 as the gate oxide in the second wafer lot to prevent the transfer of charge from the floating gate and gate via the control gate oxide.

8.4.3 0.2 μm AE3 Device Characteristics

Electrical characterization of the AE3 wafers was not performed as completely as the AE1 and AE2 wafers. In general, these devices showed poorer retention

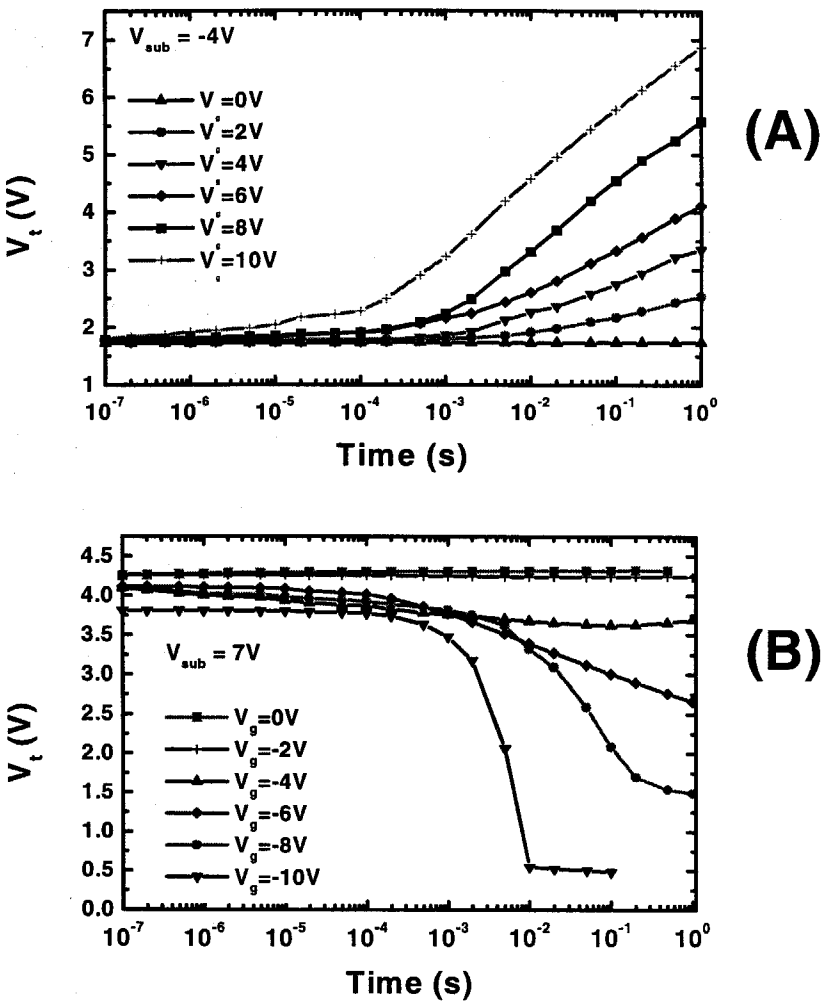

Figure 8.8: **(A)** Program transients and **(B)** erase transients for 0.2 μm AE2 aerosol nanoparticle MOSFET.

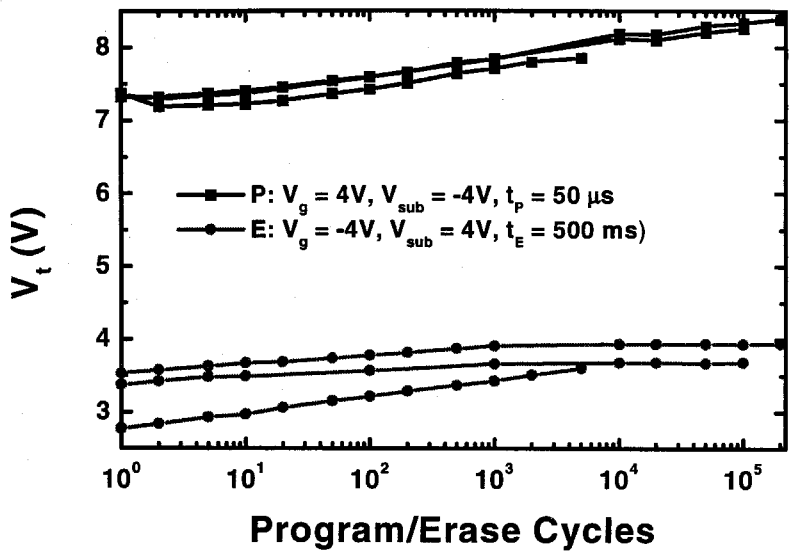

Figure 8.9: Endurance characteristics for 0.2 µm AE2 aerosol nanoparticle MOSFET.

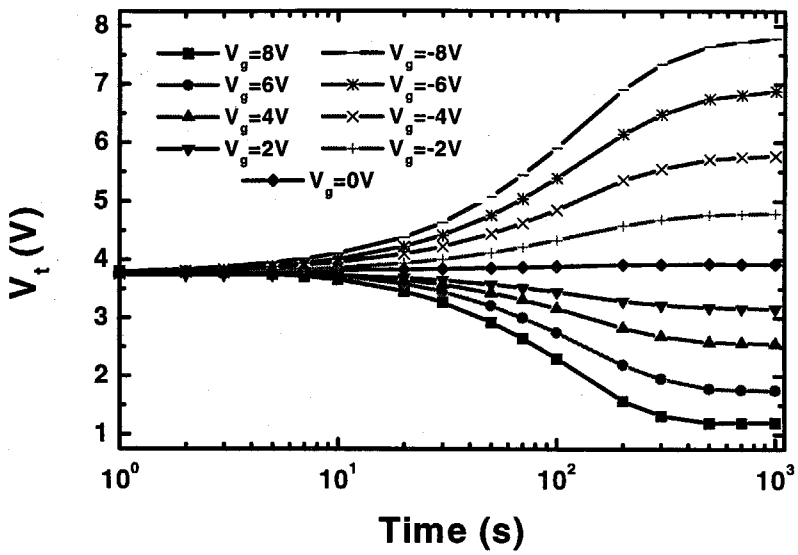

Figure 8.10: Gate disturb characteristics for 0.2 μm AE2 aerosol nanoparticle MOSFET.

characteristics and gate disturb behavior than the AE1 and AE2 samples.

8.5 Nanoparticle Density Effects

The influence of nanoparticle density can be seen by examining the variation in transistor behavior from the wafer center where nanoparticle density is extremely high with behavior towards the outer edges of the wafer where nanoparticle density is lower. As seen in Fig. 8.11, transistor failure in which a device fails to produce the characteristic subthreshold or output characteristics of a functional transistor is far more common near the wafer center than near the outer edges. Since nanoparticle densities are very high in the center of the wafers, often exceeding several monolayers, the high rate of transistor failure may be caused by nanoparticles creating short circuits between the floating gate and the gate electrode because the HTO layer thickness is insufficient to cover multiple monolayers of nanoparticles. When the monolayer coverage exceeds ~70%, the rate of transistor failure increases rapidly. The devices with nanoparticle densities 20 to 70% monolayer exhibit similar, high quality transistor characteristics and program and erase behavior.

8.6 Electrostatic Modeling of Nanoparticle Floating Gate

Modeling of the aerosol nanoparticle floating gate layer has been done to probe

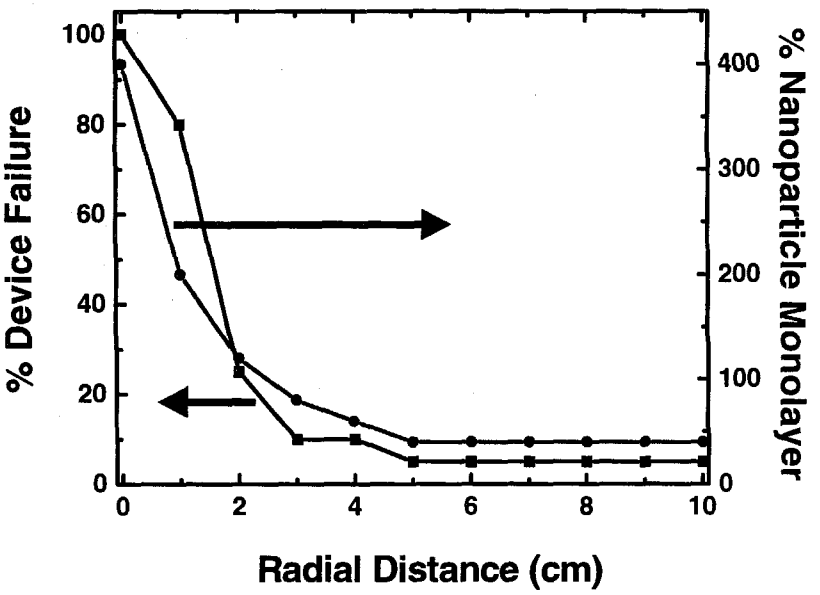

Figure 8.11: % Device failure and % nanoparticle monolayer as a function of device radial position.

the effect of a discontinuous floating gate upon the oscillatory nature of the electric field in the region of the substrate channel. General references on electrostatics have been useful in the formulations of these models [4],[5],[6]. In this simplified model, a few assumptions have been made about the nanoparticle layer and the surrounding oxide layers. The oxide layers are assumed to be free of trapped charge. Thus, the electrostatics in the oxide layers can be found by solving Laplace's equation instead of Poisson's equation that is used to solve for regions in the nanoparticle and in the substrate. The nanoparticle layer is assumed to be a one-dimensional coverage of particles upon a constant thickness tunnel oxide and covered with a constant thickness gate oxide. The nanoparticles all have the same particle diameter and separation distance between adjacent nanoparticles. The nanoparticles all contain the same number of charges of the same sign uniformly distributed throughout the particle. The nanoparticles form a continuous layer (i.e., no nanoparticles are missing from the array). Two regimes have been probed in the electrostatic modeling of the nanoparticle layer, namely the continuous sheet charge and the discrete nanoparticle layer.

8.6.1 Continuous Sheet Charge

In the continuous sheet charge regime, the nanoparticles are assumed to function as charge centers for a continuous sheet of charge located between two oxide layers. A schematic representation of this can be found in Fig. 8.12. By calculating the electrostatics in each of the layers and solving for the boundary conditions, the electric

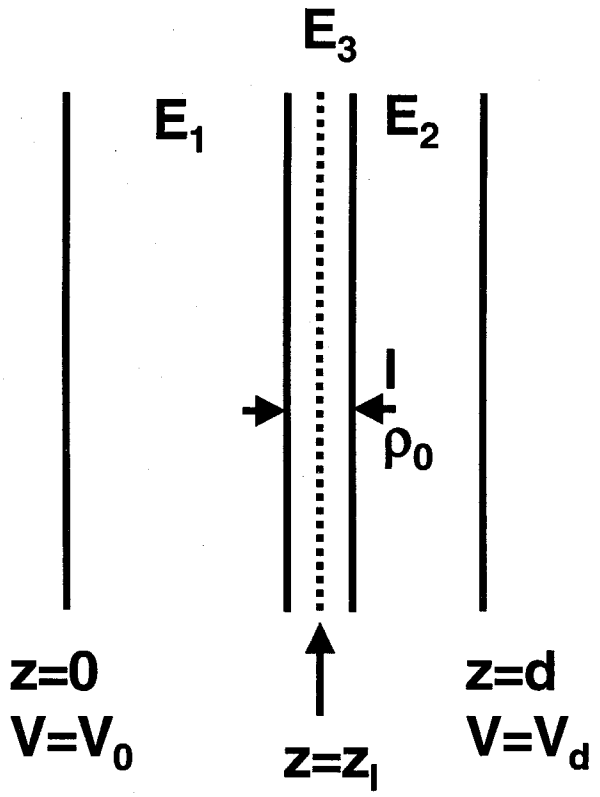

Figure 8.12: Schematic of continuous sheet charge model.

fields in all regions can be calculated. Figure 8.12 shows a planar diode with two infinite parallel plate walls located at z=0 and z=d. These walls represent the edges of the tunnel oxide and gate oxide in the floating gate device. The nanoparticle layer is represented by a charge sheet that is located between these walls and contains a uniform charge density ρ_0. The charge density can be seen to represent both the number of charges per nanoparticle and the density of the nanoparticles in the layer. The thickness of this region (or the diameter of the nanoparticles) is l and the center is situated at $z=z_1$ from the plane at z=0. The potentials of the walls at z=d and at z=0 are fixed at V_d and V_0, respectively. In the charge sheet in one dimension, Gauss's Law can be written

$$\frac{dE_z}{dz} = \frac{\rho}{\varepsilon_0} \tag{8.1}$$

where $\mathbf{E}_z$ is the electric field in the z direction and ε_0 is the permittivity of free space, 8.85×10^{-12} C^2 m^{-2} N^{-1}. In the oxide regions where it is assumed that no charge is trapped, the electric fields will be constant. Furthermore, the charge within the nanoparticle layer (represented by the charge sheet) will vary linearly with z because the charge is uniformly distributed within the charge sheet. In the diagram in Fig. 8.12 and in the equations below, E_1 represents the electric field in the tunnel oxide of the device, E_2 represents the tunnel oxide, and E_3 represents the nanoparticle layer. By integrating Gauss's law over a volume with unit area perpendicular to the z direction and solving for the boundary conditions, the fields in the three regions can be expressed by the following equations:

$$E_1 = \frac{V_d - V_0}{d} - \frac{\rho_0 l}{\varepsilon_0}\left(1 - \frac{z_1}{d}\right), 0 < z < z_1 - \frac{1}{2} \qquad (8.2)$$

$$E_2 = \frac{V_d - V_0}{d} - \frac{\rho_0 l}{\varepsilon_0}\left(\frac{z_1}{d}\right), z_1 + \frac{1}{2} < z < d \qquad (8.3)$$

$$E_3 = \frac{V_d - V_0}{d} - \frac{\rho_0 l}{\varepsilon_0}\left(\frac{z_1}{l} - \frac{z}{l} - \frac{z_1}{d} + \frac{1}{2}\right), z_1 - \frac{1}{2} < z < z_1 + \frac{1}{2} \qquad (8.4)$$

Sample calculations for the continuous sheet model can be seen in Fig. 8.13 for cases where the nanoparticle layer is 2 nm, 4 nm, 6 nm, and 8 nm in thickness and one electron per particle is assumed.

8.6.2 Discrete Nanoparticle Layer

In this model, a unit cell is defined as an area of cylindrical geometry that contains a single nanoparticle as represented in Fig. 8.14. The axial distance from the center of the nanoparticle to the top is equal to the sum of the particle radius and the gate oxide dimension. The axial distance from the center of the nanoparticle to the bottom is equal to the sum of the particle radius and the tunnel oxide thickness. The radial distance from the particle center toward the edge of the cylinder is equal to the sum of the particle radius and one half of the separation distance between adjacent particles. The electric

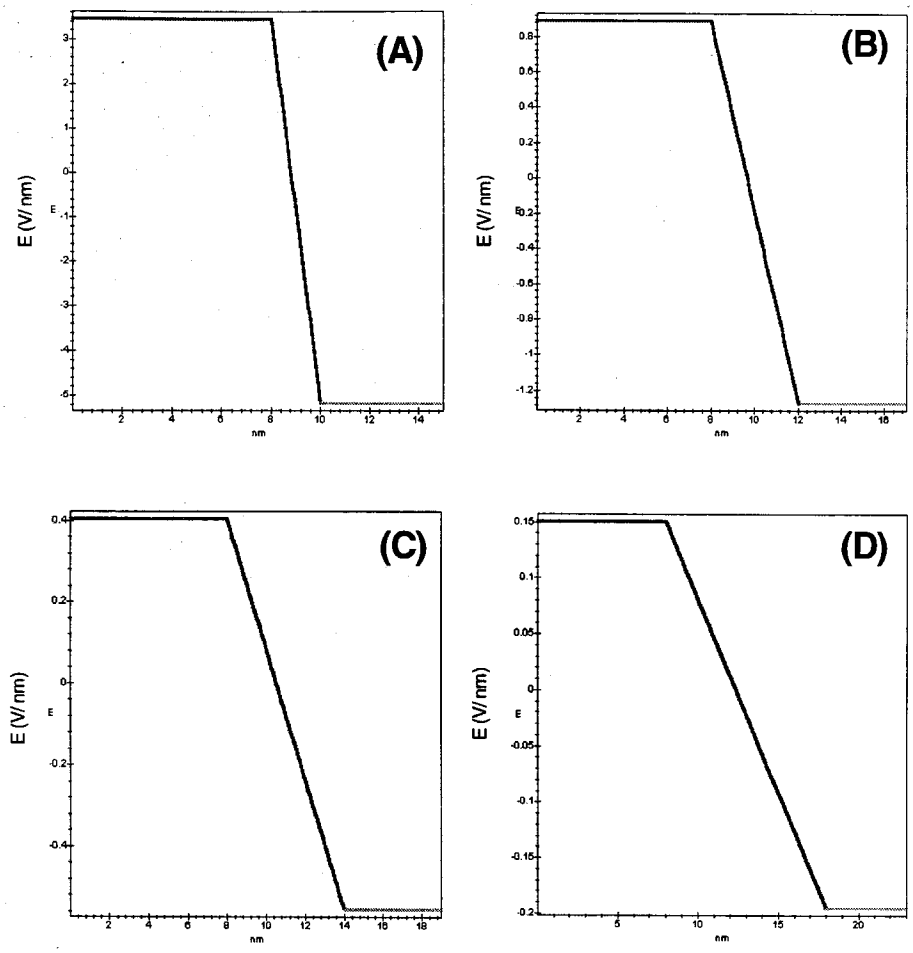

Figure 8.13: Continuous sheet charge model for nanoparticle layers **(A)** 2 nm in thickness, **(B)** 4 nm in thickness, **(C)** 6 nm in thickness, and **(D)** 10 nm in thickness. In all cases, each particle contains one electron.

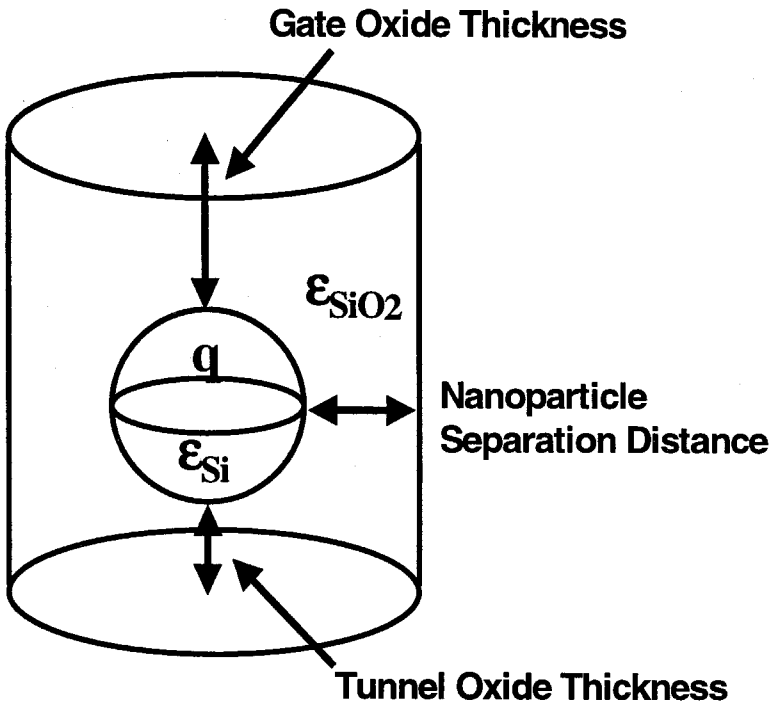

Figure 8.14: Schematic of discrete nanoparticle layer model cylindrical unit cell.

field is numerically solved for matrix points within this cylinder using Gauss's Law for the different regions within the cylinder:

$$E_1(r) = \frac{q}{4\pi K \varepsilon_{Si} r^2}(\mathbf{r}), 0 < r \leq r_1 \qquad (8.5)$$

$$E_2(r) = \frac{q}{4\pi K \varepsilon_{SiO_2} r^2}(\mathbf{r}), r_1 \leq r < r_2 \qquad (8.6)$$

where r_1 is the radius of the silicon nanoparticle and r_2 is the maximum distance between the nanoparticle center and the edge of the cylinder. In essence, this model is calculating E_2 for a spherical region in the dielectric surrounding the nanoparticle, but only those points that fall within the cylinder defined by the tunnel oxide thickness, the gate oxide thickness, and the nanoparticle separation distance are used to calculate the electric fields and voltage contours.

To obtain a regular array of nanoparticles, these cylindrical unit cells are placed in a close-packed arrangement and the electric fields are added together for neighboring unit cells. By changing the dimensions of the unit cell, the impact of the important parameters, such as nanoparticle diameter, nanoparticle density, charge, and tunnel oxide and gate oxide thickness can be determined. The effect of nanoparticle radius and separation on the voltage oscillations in the tunnel oxide is shown in Fig. 8.15a and b. A large separation distance has a greater effect on the voltage oscillations and, thus, the floating gate should be modeled as a discrete array of nanoparticles, whereas a smaller separation between nanoparticles has the effect of smoothing out any individual

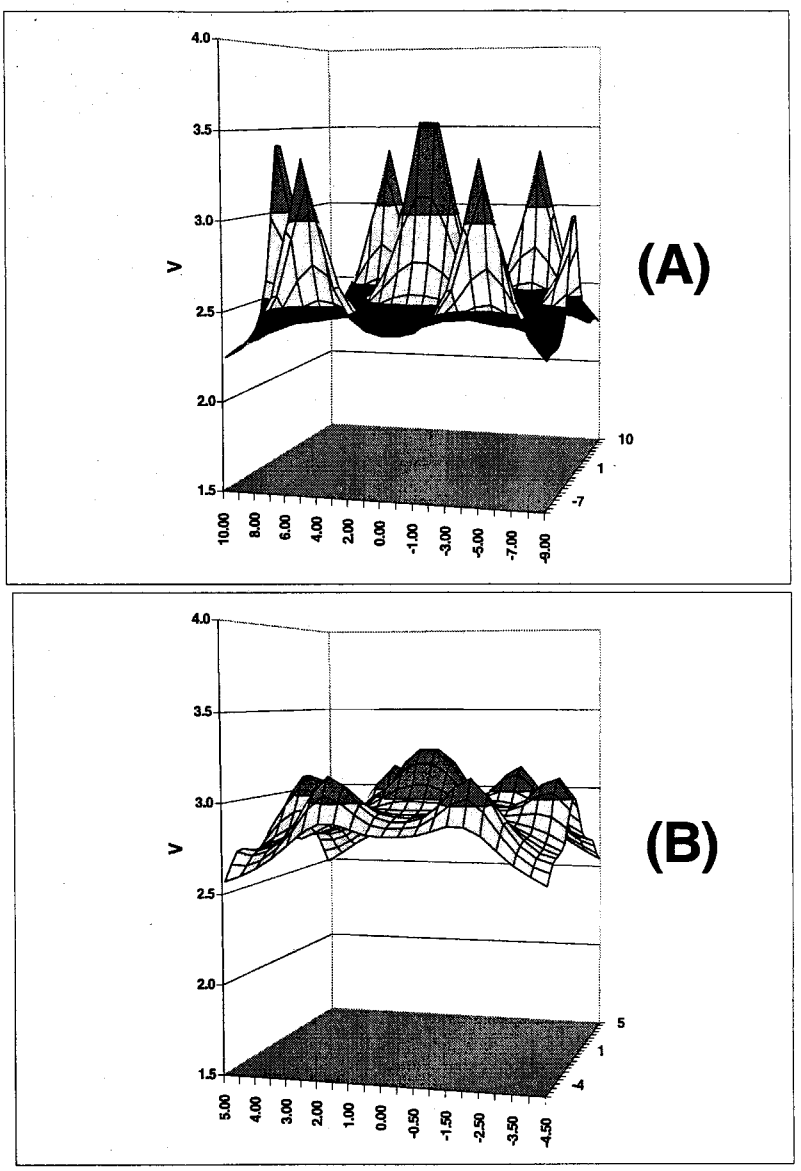

Figure 8.15: Voltage contours for discrete nanoparticle layer with **(A)** nanoparticle diameter = 1 nm and separation distance = 10 nm, **(B)** nanoparticle diameter = 1 nm and separation distance = 4 nm .

nanoparticle effects. In this case, the floating gate could adequately be modeled by the continuous sheet model.

The effect of tunnel oxide thickness on the voltage oscillations is shown in Fig. 8.16a, b, and c. For small tunnel oxides on the order of the nanoparticle size, the oscillations through the tunnel oxide are very pronounced. In these cases, the floating gate region should be modeled with the discrete nanoparticle model. However, as the tunnel oxide approaches dimensions comparable to those used in our experimental devices, the oscillations dampen out, and the floating gate could be modeled with the continuous sheet model with little introduction of error.

Figures 8.17 a and b illustrate the parameters of the devices electrically characterized in the earlier sections of this chapter. Figure 8.17a shows 8 nm particles with a separation distance of 10 nm and tunnel oxide thickness of 5 nm. Figure 8.17b shows 3.5 nm particles with separation distance of 5 nm and tunnel oxide thickness of 5 nm. In general, these parameters yield relatively flat voltage contours that could be modeled adequately with the continuous sheet model.

To understand the effect of these parameters, namely nanoparticle diameter, separation distance, and tunnel oxide thickness, a plot showing the relative effect of voltage and electric field contours on the floating gate oscillations is shown in Fig. 8.18. In this plot, the % contour notation is used to describe the % difference between the peak and the valley values for the contours. Thus, a large % contour value indicates a highly contoured plot for the floating gate, whereas a small % contour value indicates a relatively flat contour for the floating gate that could be adequately described by the

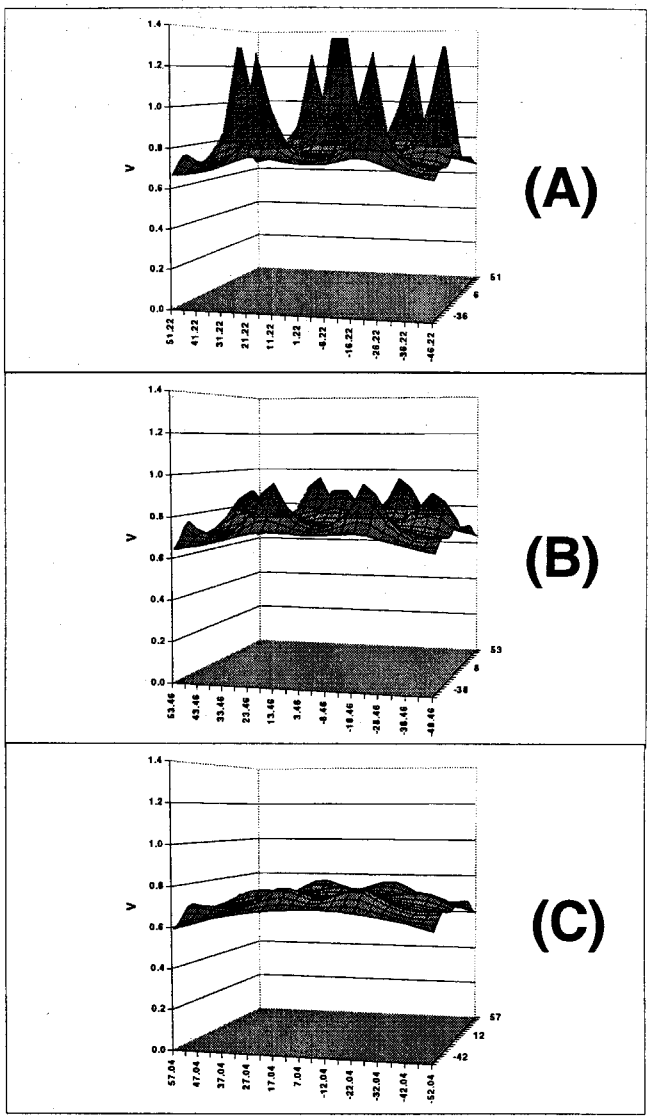

Figure 8.16: Voltage contours for discrete nanoparticle layer with nanoparticle diameter = 2 nm, separation distance = 40 nm, and **(A)** tunnel oxide = 2 nm, **(B)** tunnel oxide = 5 nm, and **(C)** tunnel oxide = 10 nm.

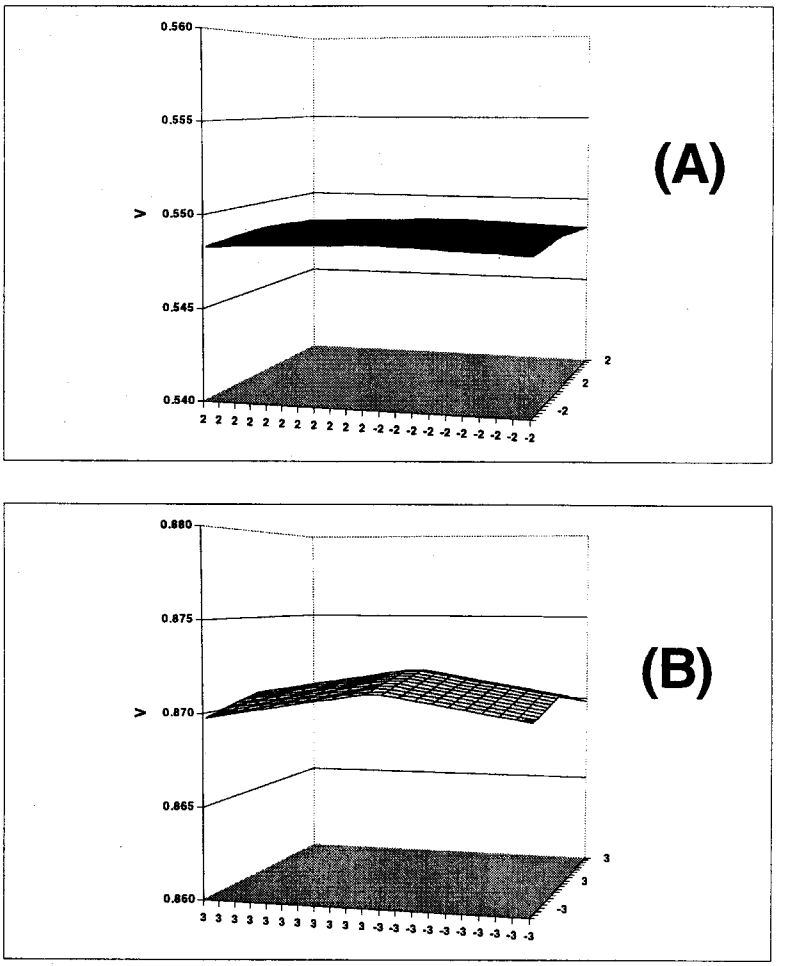

Figure 8.17: Voltage contours for discrete nanoparticle layer with **(A)** nanoparticle diameter = 8 nm, separation distance = 10 nm and tunnel oxide = 5 nm, and **(B)** nanoparticle diameter = 3.5 nm, separation distance = 5 nm and tunnel oxide = 5 nm.

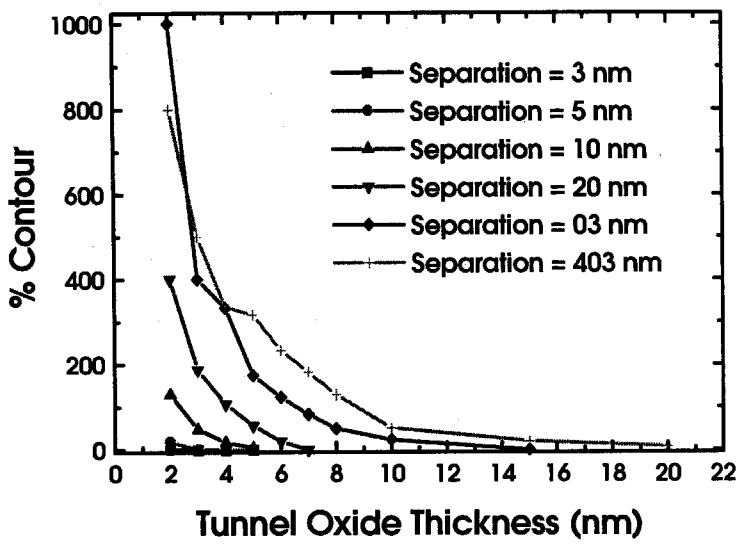

Figure 8.18: % Contour plot (% difference between maximum and minimum in voltage contour) as a function of tunnel oxide thickness and separation distance between 2 nm silicon nanoparticles.

continuous sheet model with little introduction of error. A 0% contour represents a perfectly flat voltage contour plot with no difference between the discrete nanoparticle and the continuous sheet models.

8.7 Summary

A new, aerosol-based technique has been used to integrate a very dense (~10^{12} particles cm^{-2}), coplanar, and uniform layer of nonagglomerated, spherical, single crystal nanoparticles in the gate dielectric of 0.2μm MOSFET devices. As a result of the discontinuous nature of the floating gate, the aerosol nanoparticle MOSFET devices possess very good electrical NVM characteristics, including a high read-out current, promising disturb behavior, excellent endurance, absence of SILC, and long-term charge retention after cycling.

Modeling of the electrostatics of the nanoparticle layer indicate that in many circumstances where nanoparticles are closely spaced and where tunnel oxides are as thick as those used in the aerosol devices fabricated, the nanoparticle layer can be adequately modeled by using a uniform continuous sheet charge approximation. For less dense nanoparticle layers, the model indicates that the best approximation to the electrostatics should be calculated using the discrete nanoparticle model developed.

Bibliography

[1] S. Tiwari, F. Rana, H. Hanafi, A. Hartstein, E.F. Crabbe, and K. Chan, "A Silicon Nanocrystals Based Memory," *Appl. Phys. Lett.*, **68**, pp. 1377-1379 (1996).

[2] S. Tiwari, F. Rana, K. Chan, L. Shi, and H. Hanafi, "Single Charge and Confinement Effects in Nano-Crystal Memories," *Appl. Phys. Lett.*, **69**, pp. 1232-1234 (1996).

[3] H.I. Hanafi, S. Tiwari, and I. Khan, "Fast and Long Retention-Time Nano-Crystal Memory," *IEEE Trans. Electron Dev.*, **43**, pp. 1553-1558 (1996).

[4] J.D. Jackson, *Classical Electrodynamics*, 2nd ed., John Wiley & Sons, New York (1962).

[5] A.N. Matveyev, *Principles of Electrodynamics*, Reinhold Publishing Corp., New York (1966).

[6] D.A. Dunn, *Models of Particles and Moving Media*, Academic Press, New York (1971).

Chapter 9: Final Comments and Future Improvements

As with all successful theses, the end is poorly defined and more questions than answers are found. Areas for future improvements in the production of silicon nanoparticle floating gate devices undoubtedly include improvements to the aerosol system, the particle composition, the deposition chamber, and the devices themselves. Due to the vast number of devices and wafers produced in conjunction with this thesis, plenty of material is available to continue testing of devices. In particular, temperature dependence on retention and device characterization of the second wafer lot should be important near-term goals.

Improvements to the aerosol system include the fabrication and utilization of an ultra clean differential mobility analyzer optimized for the nanometer size range to improve the size distribution control over the deposited aerosol particles. To prevent large particle losses due to extremely low charging probability of nanoparticles, an extremely efficient aerosol charger or ion source would also be useful in conjunction with the differential mobility analyzer.

When size classification becomes possible in the improved aerosol synthesis reactor, the advantages to depositing SiO_2 rather than growing SiO_2 onto classified particles will become more important. For this reason, it will be important to replace the thermal oxide furnace with a TEOS oxide deposition system into the aerosol reactor. For this reason, good control over the critical core and shell dimensions can be achieved.

Furthermore, producing doped aerosol silicon nanoparticles remains an interesting area of future research that may have important device implications.

Improvements to the 200 mm wafer deposition chamber can be made fairly rapidly and easily. These improvements will enable the production of uniform particle density deposits over the entire 200 mm wafer. However, before this improvement should be made, the optimal nanoparticle density should be determined with more complete device characterization and understanding of the role of nanoparticle density on device performance.

As discussed in some detail in Chapter 8, some improvements to the devices themselves should also be made a priority, although the second wafer lot has begun to integrate some of those improvements already. These changes include improving the quality of the control gate oxide to prevent charge transfer through the gate and the floating gate. In the second wafer lot, this has been attempted by replacing the HTO SiO_2 layer with a Al_2O_3. A more difficult improvement to the nanoparticle floating gate layer will be the fabrication of close packed arrays of these nanoparticles. This may require the formation of stable, nonreacting colloidal solutions of silicon nanoparticles that can be deposited in close packed arrangements without compromising the contamination issues required for processing these devices. Exciting research continuing at Caltech that could be integrated into future devices is the layered tunnel barrier to replace a homogeneous tunnel oxide to improve the retention and to decrease the programming time for nanoparticle-based memory devices.

With this thesis, we have demonstrated that a new, exciting combination of

aerosol science and semiconductor device processing has potential to produce new and improved devices. The utilization of aerosol particles in the semiconductor industry and in future devices may well solve many problems plaguing the semiconductor industry as feature sizes become smaller and more dense. Aerosol particles may well become the integral parts of future functioning device, and no longer dismissed as defects that need to be avoided.

Appendix A: Ultra Clean Reactor Protocol : Start Up and Shut Down Procedure

A.1 Ultra Clean Reactor Protocol - Start Up Procedure

1) Verify that the valve between the ultra clean reactor and the DMA system (A) is closed. To turn, hold onto the back side of the valve so that the stainless steel tube and quartz tube connection are not torqued while the valve handle is turned gently. If this is not done, it is likely that the bottom of the quartz tube will break or chip, requiring that the quartz tube be replaced in the furnace. This is a time consuming process.

2) Turn on the sintering/pyrolysis furnace (A) and the oxidation furnace (B) if oxide-passivated nanoparticles are to be made. This is done by turning the switches on the two variacs to the on position (flip to the right). The temperatures in both reactors should be set to at least 900°C with the oxidation furnace at 1000°C or above to make high quality thermal oxides. Verify that thermocouples in the furnaces are operational.

2a) Verify that all valves in the DMA system are set correctly. Verify that all four valves in the DMA system are set to connect the ultra clean system to the DMA system. In general, this series of four valves should include the DMA but bypass the oxidation furnace.

3) In the DMA system, turn on the N2 sheath flow tank and the mass flow controllers (MFCs) to the Q_{vac} (channel 1) and Q_{sh} (channel 2). Turn on the vacuum pump that draws the excess flow from the DMA. The Q_{ex} and Q_{ele} are controlled by separate critical orifices that occasionally need to be cleaned by sonication in methanol for 5-10 minutes.

4) Verify that Q_{sh} balances Q_{ex}. If they are not balanced, either increase Q_{sh} by changing MFC channel 2 or by cleaning the Q_{ex} critical orifice. When changing the flow rate through the MFC, verify that the MFC is set to flow, not ratio or remote, and that the set point value is being changed, not the ratio value. Refer to the manual on the MFC for details.

5) Open the Q_{ele} valve so that the vacuum pump is drawing gas through the electrometer. Again, this flow rate is controlled by the critical orifice. Turn on the electrometer.

6) Verify that the electronics grade nitrogen and oxygen are attached to the ultra clean system. These cylinders are painted white. Open the valves on the top of the cylinders and then open the valves (B) immediately after the regulators on both tanks. Turn on Q_a (channel 3) and QO_2 (channel 4, if required) at the appropriate flow rates. Since the valve (A) is closed between the ultra clean reactor and the DMA system, all flow will exit into the cleanroom.

7) When the temperatures in the sintering/pyrolysis furnace (A) and the oxidation furnace

(B) are above 900°C, turn on the silane flow. Verify that electronics grade silane is attached to the ultra clean system. This cylinder is also painted white. Open the valve on the top of the cylinder and then open the valve (B) immediately after the regulator. The silane flow rate is controlled by the metering valve (C) located after valve (B) and before the silane stream combines with the Q_a nitrogen stream. This metering valve (C) is very sensitive and capable of controlling very precise silane flow rates. To begin, turn the metering valve (C) to the closed position and then start size distributions around 3/4 CCW turn.

8) Reverify that all flows are now operational and correct. Reverify that the pumps are working correctly.

9) Carefully open valve (A) - remember to hold the back of the valve while turning to prevent breaking the quartz tube in the oxidation furnace.

9) Take size distributions of the resulting aerosol. Start with short settling times ~2 sec and short counting times ~5 sec.

10) To increase the particle diameter, turn the metering valve (C) CCW. To decrease the particle diameter, turn the metering valve (C) CW. If no particles are seen in the initial size distributions, either the valve is open too far and very large particles are being made or the valve first needs to be open an additional 1/4 turn or so. Once particles are

detected, further adjustments of the valve (C) can be made to tune the size distribution.

11) When an appropriate size distribution is obtained, increase settling time ~10 sec and counting time ~20-30 sec and repeat size distributions.

12) Repeat steps 10 and 11 until desired size distribution is obtained and is very stable and fluctuates only slight after repeated runs.

A.2 Ultra Clean Reactor Protocol - Shut Down Procedure

1) Carefully close valve (A) between the ultra clean reactor and the DMA system. To turn, hold on the back side of the valve and gently close the valve.

2) Turn off the Qex vacuum pump and Qvac pump. Turn off the power on the MFCs for Qsh and Qvac. Close the valve on the sheath nitrogen cylinder. Turn off the electrometer.

3) Turn off the silane flow by closing the cylinder valve, valve (B) between the regulator and the metering valve (C), and then the metering valve (C).

4) Turn off the sintering/pyrolysis furnace (A) and the oxidation furnace (B) if used by turning the switches on the variacs to the off position (flip to the left).

5) Turn off the nitrogen and oxygen tanks by closing valve (B) on each tank. If the tanks are not going to be used in many weeks, turn off the valves on the tops of each cylinder as well. Turn off power to the MFCs for Qa (channel 3) and QO2 (channel 4).

Appendix B: Cleanroom Protocol and Wafer Handling

B.1 Cleanroom Protocol

1) No jewelry is allowed in the cleanroom. Empty all pockets prior to entering cleanroom. Tie back long hair. Keep good personal hygiene.

2) To gown, put booties on first. Then, follow with lab glasses, face mask, and hood. Put on gloves and finally put on the gown.

3) Keep the cleanroom on at all times. In case of a power outage, turn cleanroom back on and wait 24 hours before using again. If the power goes out, label all wafers not sealed in plastic. Those are now dirty and cannot be used for ultra clean work, including TXRF/SIMS and device manufacturing.

4) Keep talking and excessive hand motions to a minimum.

5) Do not enter the cleanroom if you have a cold. Do not sneeze in the cleanroom.

6) Anything above table level is considered class 100. If work above table level is required, be sure to move wafers away from your work area. Never work above wafers or

the wafers could become contaminated.

7) Wipe down surfaces with electronic grade ethanol and cleanroom wipes prior to sample preparation.

8) When a wafer is in the deposition chamber, do not adjust any valves on the clean system. The clean system must be isolated from the DMA system by the valve (A).

B.2 Wafer Handling

1) Wafers must never come in contact with anything metallic or any material that has touched something metallic.

2) Remove wafers from wafer boats with the quartz fork. Replace wafers into the wafer boats with the quartz fork. Keep the wafers level in the wafer boats - put them in the same slots on both ends.

3) Clean all quartz in the cleanroom with an RCA clean prior to use, especially if new quartz material is being used for the first time or if metallic objects have contacted the quartz material.

4) Remember, do not risk wafer contamination. Keep your hands, arms, and face to the

sides of the wafer.

B.3 Loading/Unloading Wafers in the Deposition Chamber

1) Open deposition chamber and placed individual pieces on the stainless steel table on cleanroom wipes to prevent scratching the table.

2) Wipe down the water-cooled disk and surfaces of the deposition chamber with electronics grade ethanol and cleanroom wipes prior to use.

3) Position the quartz pegs on the water-cooled disk.

4) Remove the wafer from the wafer boat with a quartz fork, carry to the deposition chamber, and put onto the quartz pegs. If the pegs are long enough, the fork will slide out from under the wafer. If the pegs are short, then you must use a clean quartz rod to slide the wafer off of the quartz fork. Contact ONLY the side of the wafer with the quartz rod.

5) Replace the pieces of the deposition chamber. Place the pieces down individually and slide into position. Remember, do not risk wafer contamination. Keep your hands and arms to the sides of the wafer. Do not look directly at the wafer from above because this could also contaminate the wafer.

6) Put the viton O-ring onto the top plate. Be careful that it does not touch the wafer surface. Slide the deposition chamber underneath the suspended cover. This will require moving the stand that supports the cover and stainless steel tube leading into the cleanroom from the oxidation furnace. Rotate the top plate until the holes match the top plate and the cover.

7) Put in 6-7 bolts to seal the cover to the top plate.

8) Put heating tape around the top of the sealed deposition chamber and cover with the stainless steel donut. Tuck the thermocouple in between the heating tape. Be careful that the heating tape extending from the deposition chamber does not contact any material that may melt, especially the temperature controllers and the polymer surrounding the thermocouple.

9) Turn on the temperature controller and the power to the heating tape. Be CAREFUL not to unplug the furnace temperature controllers when this is done.

10) Be sure the water to the water-cooled disk is on - this is turned on outside the cleanroom and should be done before entering the cleanroom or immediately after leaving the cleanroom.

11) Collect the sample for the required time.

12) To remove the sample, repeat the steps a-i in reverse order. NOTE: After removing the heating tape, some fibers are sure to remain behind. Before opening the cover, wipe down the top plate and cover with electronic grade ethanol and cleanroom wipes to remove these fibers. Additionally, when sliding the deposition chamber out from under the cover, it is imperative to slide the stand up to support the cover. If this is not done, the stainless steel tube could bend, causing the electropolished finish to be destroyed and the pressure on the tube could cause the quartz tube in the oxidation furnace to crack.

13) If possible, turn off the heating tape about 20-30 minutes prior to wafer removal. This will allow the top plate and cover to cool enough where it won't burn so much when they are touched. This may interfere with sample collection, so this is usually not permitted when making device samples.

Appendix C: Ultra Clean Reactor Parts

C.1 Gas Delivery System

Gases: Matheson

Electronics grade/semiconductor grade purity gases are required. For the silane mixture, use electronics grade/semiconductor grade nitrogen as the mixing gas. These pure gases tend to take ~1-2 weeks to receive and the silane mixture takes ~3-4 weeks.

Gas Regulator System, Pigtail, Control Valve: Matheson Tri-Gas

Ultra single-stage regulator: 9307-4-V4FM

Regulator Panel and Pigtail: 9001-540 (CGA=540 for nitrogen and silane/nitrogen mixture)

Control valve: 9526-V4FM

Filter/Purifier: Matheson Electronic Product Group

Nanochem Purifilter: 1060-0376-001

Mass Flow Controller: MKS Instruments

Flow Controller: 1179A**CR1BV (** specify specific flow rate range required)

Cable: CB259-5-10

Power Supply/Readout: 247D

Stainless Steel Tubing: Valex

1/4" electropolished stainless steel tubing, 10 R.A. 20' long:T3A-OS-00250-035BO

Connections: Orange Valve & Fitting

VCR Connections (for welded stainless steel VCR fittings): Part numbers depend upon product specifications - order with -p attached to the part number for electropolished finish. If the parts are not electropolished, they will need to be prior to installation.

Cajon Connections (for quartz to VCR connections): Part numbers depend upon product specifications

Quartz Tubing: GM Associates, Inc.

Semiconductor Grade Quartz: 6000-141 9.5mm/7mm Quartz tubing

6000-22	12.75mm/10.5mm Quartz tubing
6000-33	19mm/17mm Quartz tubing

C.2 Deposition Chamber

Stainless Steel Flanges: MDC Vacuum Products

Custom Parts, Wheels, Tube Stand, Water-Cooled Disk - Custom-made at Caltech Metal Shop (Keck Subbasement)

Viton O-Rings: MDC Vacuum Products

C.3 Cleanroom Supplies

Quartz Fork : Quartz International

Quartz Fork: QI-5950-001-78 special order

Quartz Sleeve: QI-5958-002-78 special order

Cleanroom Garments and Tacky Mats: Coast Scientific

RCA Chemicals: Semiconductor Grade Quality

Cleanroom Bags: Lucent Technologies (donated)

C.4 Assembly of Ultra Clean Reactor

All components sealed in Class 100 cleanroom should be opened in cleanroom. Assemble entire system in the cleanroom, using electronics grade ethanol and cleanroom wipes to clean any surfaces that were not sealed in Class 100 environment. This does NOT include rinsing metal tubing. Use stainless steel gaskets once and do not over tighten. Follow directions for VCR fittings as provided in the literature from Orange Valve & Fitting Co. and use stainless steel gaskets only once. Attach as many tubes and connections as possible in the cleanroom. When largest segments of tubes and connections are completed, protect the ends of the tubes with covers, take outside cleanroom, and finish installation. Rinse parts and ends with electronics grade ethanol and cleanroom wipes. To replace gas cylinders, take care to remove CGA carefully so that pigtail does not get bent. Rinse cylinder valve and CGA with electronics grade ethanol and dry with cleanroom wipes. Protect openings as much as possible by keeping them covered until ready to attach CGA to cylinder valve.

Appendix D: TEM Sample Preparation Techniques

D.1 Colloid Evaporation

Take a known volume of colloidal nanoparticles and drop onto the front center of TEM grid. It is best to hold the TEM grid with tweezers the entire time while solvent is evaporating. Repeat as necessary for less concentrated colloidal solutions.

D.2 Electrostatic Deposition

Insert a TEM grid front side up into the electrostatic precipitator. Use the Teflon guides to define the axial position and the distance from the nozzle. If collecting an unclassified sample, keep the time short since many particles will deposit and will interfere with good TEM imaging and cause the sample to appear agglomerated when it is really a thick sample of single nanoparticles deposited on top of each other.

D.3 Cross Section

1) Take two samples, cleave into ~3 x 8mm pieces. Clean with isopropanol and acetone and stand on end to dry. The faces should appear clean with no debris or particles

present.

2) Remove M-Bond 610 from the refrigerator and allow to come to room temperature. Take a small amount of M-Bond and spread over the faces of the two samples. Place sample faces together and center the pieces as much as possible. Place between a folded piece of resist paper and place into cross section clamps. Keep at ~135°C overnight.

3) Remove the samples from the clamp and resist paper. Place onto a metal strip (used with the diamond saw) with sufficient melted crystal bond. Allow to cool.

4) Assemble diamond saw - if samples are primarily silicon, use the HC diamond blade - and clean bottom tray used to catch some samples that may come off in the cutting. Make several cuts perpendicular to the long axis of the sample. This way, several 3 x 1mm samples can be made. Make sure that the saw goes through the entire sample or else there will be edges on the samples. Listen for the distinctive change in sound when the silicon is cut completely.

5) Dissolve and clean all samples in acetone.

6) Flatten a brass sample holder with the hole in the top with sandpaper strips. Rinse before going to a smaller grit size. This only takes a few strokes on the sandpaper.

7) Melt small amount of crystal bond on the flattened side of the brass holder and place one of the samples in the crystal bond. The interface should be perpendicular to the flattened brass surface. This insures a better oriented sample is prepared and makes the TEM easier. It also may prevent samples from fracturing when they get too thin. Allow to cure.

8) Depending upon how thick or thin the sample is, start by using the sandpaper strips. Replace them if they were used for polishing any material other than silicon. Use only a few even swipes and check continuously for progress. The coarser sandpapers remove a lot of silicon, so use those sparingly or skip altogether if the sample is already thin. Polish in the direction parallel to the interface. Rinse sample before changing grits.

9) After 600 grit paper, move to the minimet polishing tool. Place small amounts of diamond paste on the sample, starting in order with 6 micron, 3 micron, and 1/4 micron sizes. Add Metadi fluid as necessary to moisten the diamond paste. Generally, speeds of 30, forces of 3, and times of 5-6 minutes are sufficient for silicon. Check progress by looking under the light microscope. If scratches primarily in one direction along the interface are seen, repeat that same size before proceeding to the smaller diamond paste sizes. After using the 1/4 micron diamond paste, the sample should have a mirror like finish with little or no visible scratches in it.

10) Remove the sample from the brass cylinder by dissolving the crystal bond with

acetone.

11) Remove M-Bond 610 from the refrigerator. Allow to come to room temperature. Rinse the sample with isopropanol and acetone to insure that the polished face is as clean as possible. Take a Cu slot grid, rub the front side with sandpaper to scratch the surface a bit, and rinse in isopropanol and acetone to clean. The front side of the slot grid has flatter edges. The back side has rounded edges.

12) Carefully apply a small amount of M-Bond to the front side of the slot grid while the grid is on a clean glass slide. Move the grid around on the slide to remove excess M-Bond. Invert the glass slide (the slot grid should stick to the inverted slide) and position the slot grid over the sample (also on a glass slide) so that the interface runs parallel to the length of the slot. Do not allow M-Bond to contact the interface of the sample. Allow to cure on a hot plate for at least 30 minutes. Move sample around the glass slide to prevent it from bonding to the glass slide during the first few minutes of curing at elevated temperatures.

13) Add a very small amount of crystal bond to the quartz window of a dimpler stub. Position the slot grid and sample (the polished surface faces toward the dimpler stub) at a 45° angle to the stub and allow the sample to become horizontal by its weight. This prevents bubbles from becoming trapped under the sample. Center the sample and press down firmly with tweezers. Allow to cure for a few minutes.

14) Use the dimpler according to the instructions. Use the smallest weights possible and generally flatten the sample until it becomes ~ < 50 microns thick with 10 micron diamond suspension. Then, switch to the dimpling tool and dimple until a hole appears in the sample. When the sample is getting thin, it is a good idea to check the sample every 30 sec or so to prevent the sample from dimpling away. The final dimpling should be done with the 0.1micron diamond solution.

15) Remove the sample from the dimpler stub by soaking in acetone UNDISTURBED for 45 min. Be very careful with the sample at this point because it can easily fall apart. Carefully remove the sample from the acetone and dry.

16) Set up the ion mill according to the instructions. Mill the sample as required in order to obtain thin areas around the interface. At this point, it is usually easy to see the color change associated with thin silicon substrates. Use this to monitor the ion milling progress as well as the smoothing out of the sample.

D.4 Wedge

1) Follow the cross section technique from steps 1 to 5.

2) Place one side of the sample onto the center of a flattened glass rod end with a small amount of M-Bond. The more crystal bond used, the more time consuming is the

polishing process, so use only the amount required to hold the sample to the rod. The interface should be perpendicular to the glass rod end. Take care to insure that the interface is almost perfectly perpendicular since this will prevent the sample from cracking during future polishing steps. Allow to cure overnight.

3) Gently polish the sample on sandpaper and follow with the Econonet polisher. For the econonet polisher, follow the instructions, first using the 6um polishing wheel, then the 3um, and finally the 1/4 micron wheels. For these samples, polish so that the polishing wheel first contacts the front side of the sample. This prevents debris from ruining the sample. Monitor progress and polishing quality with the light microscope. Use the optical microscope to verify the quality of the area of interest in the device - to make sure that no fractures have damaged the front side of the sample. Sometimes debris will damage the front side of the sample and it is important to polish through this damaged area. After polishing, finish with a short colloidal silica polish with the sample face turned the opposite direction so that the sample face is turned away from the direction of the polishing wheel. Rinse the sample gently with soap and water.

4) Place the glass rod sample side down into acetone and allow to dissolve undisturbed.

5) Attach the sample to the glass rod again with M-Bond, this time polished side face down against the glass rod with the sample face toward the edge of the glass rod. Also, place the sample very close to the edge of the glass rod. The closer to the edge, the faster

the polishing. However, sometimes it's convenient to have some glass before the sample so that the wedge progress can be monitored on the glass rod before the sample is affected. This advance warning allows one to reposition the sample if necessary.

6) Insert the glass rod into the wedge tool and determine the correct wedge angle. Verify that the wedge will be uniform across the entire face by adjusting the feet (in relation to each other)of the wedge tool. Change the angle of the wedge by adjusting the feet (in relation to the sample) of the wedge tool.

7) Again, polish the sample using the Econonet, first starting with the 6 micron, then 3 micron, and finally the 1/4 micron. Track polishing progress with the light microscope and insure that the sample face is undamaged with the optical microscope. Adjust the wedge tool feet to insure that the wedge is uniform across the sample and that the wedge angle is correct. The optical microscope can be used at this point to monitor the thickness of the sample. The thickness is related to the focus points of the glass rod versus the sample surface and can be relatively accurately measured with the optical microscope. When the sample begins to thin sufficiently, a brown-orange color will appear at the sample face. Finish the polishing with a short polish with colloidal silica. Remember to face the sample away from the direction of the polishing wheel for this step.

8) Carefully place the glass rod into acetone with the sample side facing down and let it remain undisturbed for ~45 minutes. The sample is very delicate at this point, so be very

careful with it.

9) Dry the sample.

10) Carefully apply a small amount of M-Bond to the front side of a slot grid while the grid is on a clean glass slide. Move the grid around on the slide to remove excess M-Bond. Invert the glass slide (the slot grid should stick to the inverted slide) and position the slot grid over the sample (also on a glass slide) so that the sample surface runs parallel to the length of the slot. It is important to the make sure that a sufficient portion of the sample remains attached to the copper grid, so the sample surface may not be exactly in the middle of the slot region. Do not allow M-Bond to contact the interface of the sample. Allow to cure on a hot plate for at least 30 minutes. Move sample around the glass slide to prevent it from bonding to the glass slide during the first few minutes of curing at elevated temperatures.

11) If necessary, ion mill the sample to thin the region. In some cases, the wedge technique will produce sufficiently thin samples that this milling step is not required.

D.5 Double-Wedge

1) This technique is nearly identical to the wedge technique. The only difference being in step 7. So, follow steps 1 through 6 as listed in the Wedge section.

2) Polish the sample using the Econamet, first starting with the 6 micron, then 3 micron, and finally the 1/4 micron. Track polishing progress with the light microscope and insure that the sample face is undamaged with the optical microscope. Adjust the wedge tool feet to insure that the wedge is NOT uniform across the sample, but thins slightly faster on one edge versus the other, and that the wedge angle is correct. The optical microscope can be used at this point to monitor the thickness of the sample. The thickness is related to the focus points of the glass rod versus the sample surface and can be relatively accurately measured with the optical microscope. When the sample begins to thin sufficiently, a brown-orange color will appear at the sample face. Continue polishing until the thinnest edge of the sample begins to thin in towards the center of the sample. This polishes away the edge of the sample, but provides very good control over the exact area imaging is desired. Track this progress with the optical microscope and stop polishing when the removed sample area <1 micron away from the feature of interest. Finish the polishing with a short polish with colloidal silica. Remember to face the sample away from the direction of the polishing wheel for this step.

3) Continue with steps 8 through 10 as described in the Wedge section.

4) Ion milling is not required in this sample since the region of interest in the double wedge will be thin enough to image with the TEM.

E: Model Source Code

```
> restart;with(plottools):
> vd:=2;v0:=0;

                        vd := 2

                        v0 := 0

> p:=10;q:=-1;z0:=0;zp:=8+p/2;zd:=5+zp+p/2;

                        p := 10

                        q := -1

                        z0 := 0

                        zp := 13

                        zd := 23

> v:=4/3*3.1415*(p/2)^3;

                    v := 523.5833333

>
> r0:=q/v*1e9*1.6e-19;

                                -12
                    r0 := -.3055865034 10

> e0:=8.85e-12;e1:=e0*3.9;e2:=e0*3.9;e3:=e0*11.8;

                                -11
                    e0 := .885 10
```

$$e1 := .34515\ 10^{-10}$$

$$e2 := .34515\ 10^{-10}$$

$$e3 := .104430\ 10^{-9}$$

```
> E1=((vd-v0)/zd)-(r0*p/e1)*(1-(zp/zd));
>
```

$$E1 = .2370849930$$

```
> E2=((vd-v0)/zd)+(r0*p/e2)*((zp/zd));
```

$$E2 = -.1082104910$$

```
> E3=((vd-v0)/zd)-(r0*p/e3)*((zp/p)-(z/p)-(zp/zd)+.5);
```

$$E3 = .5133213804 - .03452954841\ z$$

```
>
plot(((vd-v0)/zd)-(r0*p/e1)*(1-(zp/zd)),x=0...zp-p/2,axes=boxed,thickness=3,labels=[nm,
E],style=line,color=red);
```

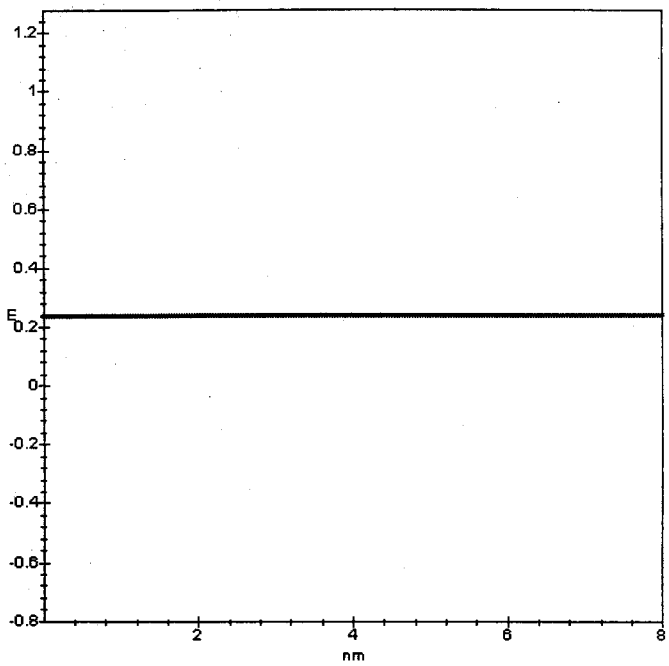

>

plot(((vd-v0)/zd)-(r0*p/e3)*((zp/p)-(x/p)-(zp/zd)+.5),x=zp-p/2...zp+p/2,axes=boxed,thickness=3,labels=[nm,E],style=line,color=blue);

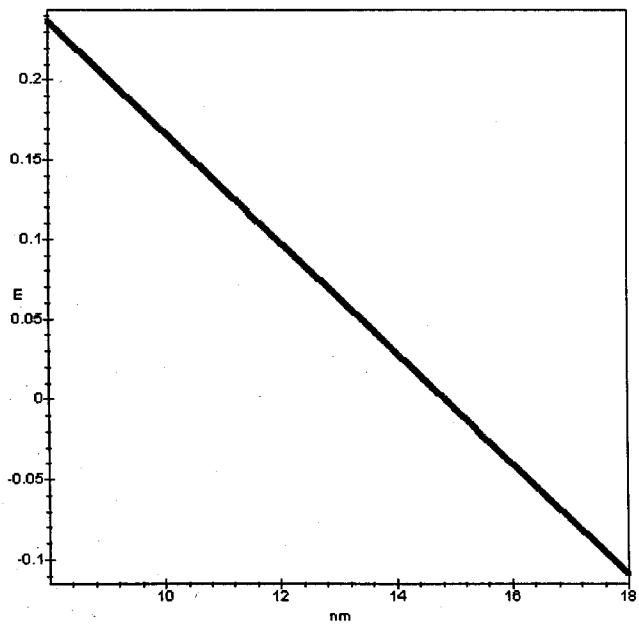

```
>plot(((vd-v0)/zd)+(r0*p/e2)*((zp/zd)),x=zp+p/2...zd,thickness=3,axes=boxed,labels=[n
m,E],style=line,color=green);
```

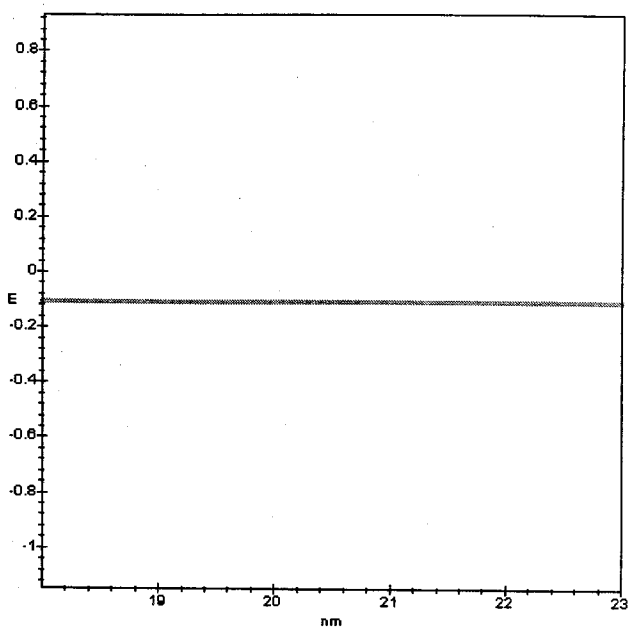


```
>
with(plots):ae1:=plot(((vd-v0)/zd)-(r0*p/e1)*(1-(zp/zd)),x=0...zp-p/2,thickness=3,axes=b
oxed,labels=[nm,E],style=line,color=red):ae3:=plot(((vd-v0)/zd)-(r0*p/e3)*((zp/p)-(x/p)-
(zp/zd)+.5),x=zp-p/2...zp+p/2,thickness=3,axes=boxed,labels=[nm,E],style=line,color=bl
ue):ae2:=plot(((vd-v0)/zd)+(r0*p/e2)*((zp/zd)),x=zp+p/2...zd,thickness=3,axes=boxed,la
bels=[nm,E],style=line,color=green):display({ae1,ae3,ae2});

>
```

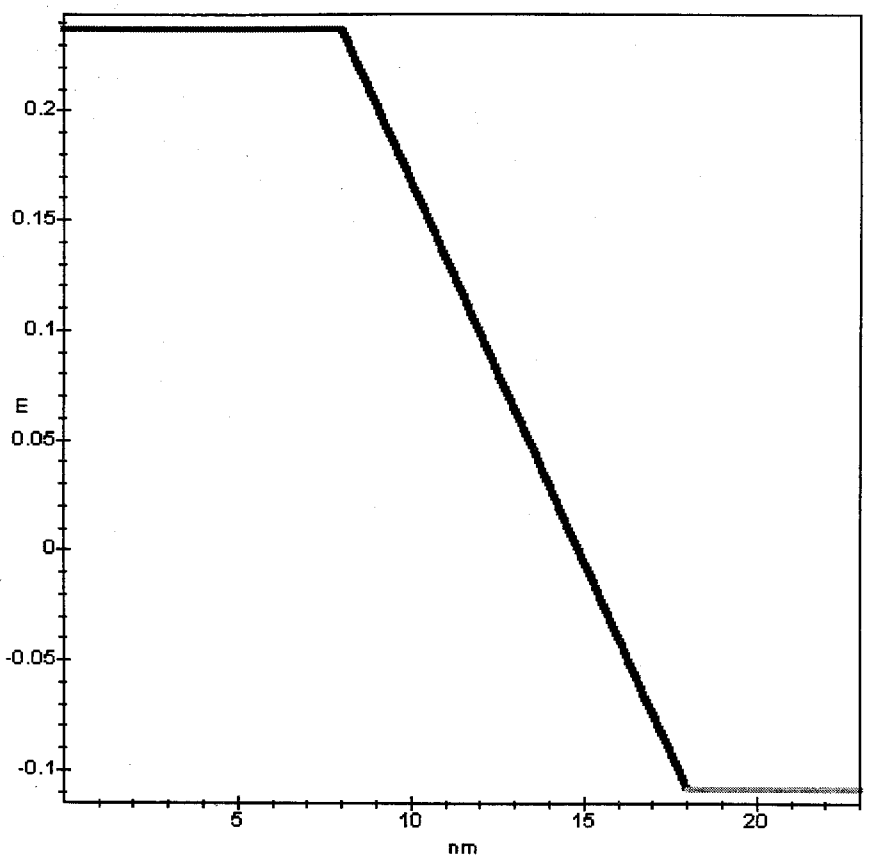
0.2
0.15
0.1
E
0.05
0
-0.05
-0.1
5
10
15
20
nm